Ph.D. Thesis

Interplay between non-relativistic spin-splitting and spin-orbit coupling in metallic systems

By

AMAR FAKHREDINE

Institute of Physics, Polish Academy of Sciences
in
Division of Magnetic Heterostructures ON-3.4

Submitted in partial fulfillment of the requirements for the degree Doctor of Philosophy

Supervisor: Dr. hab. **Carmine Autieri**, Institute Professor
Auxiliary supervisor: Dr. **Giuseppe Cuono**

NOVEMBER 7, 2024

Abstract in English

Non relativistic spin splitting is typically a characteristic phenomenon observed in systems with broken time-reversal symmetry. It is primarily influenced by the effect of magnetic exchange interaction J_{ex} between the spins causing an energy shift between spin-up and spin-down electrons. The occurrence of spin splitting cannot be observed in a system where the time-reversal symmetry (TRS) is preserved, as this symmetry leads to the Kramer's degeneracy. The spin-splitting occurs independently of spin-orbit coupling (SOC) effects though its presence can produce interesting effects through its interplay with the spin-splitting, such effects will be the main topic of this thesis. The property of non-relativistic spin-splitting has proved its importance in spintronics and has several effects on the materials' properties. For example, it can lead to the formation of spin-polarized currents and with SOC can lead to spin Hall (SHE) and anomalous Hall effects (AHE).

The presence or absence of symmetries has become one of the most important aspects in condensed matter physics as it leads to the description of robust phenomena, especially in magnetic and topological systems. The effect of broken space-inversion symmetry in large SOC systems, for instance, is necessary for the presence of the Dzyaloshinskii-Moriya interaction (DMI) which leads to the creation of chiral magnetic structures arising from spin dynamics. In addition, breaking time-reversal symmetry is essential for the emergence of transport responses, such as the AHE, which not only depends on SOC but can also be controlled by its effects. In the presence of spin-orbit coupling in systems with broken inversion symmetry, other significant effects such as the Rashba spin-orbit and the Dresselhaus effect can arise. Furthermore, in topological materials, the breaking of the time-reversal symmetry can give rise to topological Weyl semi-metals.

This thesis includes studies of a few systems characterized by the property of broken time-reversal symmetry exhibiting non-relativistic spin-splitting of energy bands visible in the band structure where its interplay with spin-orbit coupling can generate DMI and/or AHE. These systems with broken time-reversal symmetry can be classified into two categories:

1. **Ferromagnetic systems**: Magnetic thin films of Re/Co/Pt were studied in the first two papers; this system produces very high DMI values due to the availability of the vital conditions. Space-Inversion symmetry is broken due to the presence of interfaces, and the effect of SOC is relatively too strong stemming mainly from platinum. This work presented in Chapter 3, is purely theoretical, based on density functional theory calculations (DFT) in which we examine the effect of tuning the thickness of Co thin films and the effect of interface intermixing on the overall dynamics of the studied system. Chapter 4, is a collective experimental and theoretical study of the same system, it focuses mainly on the importance of interface type and quality on the DMI contribution. Chapter 5, the anomalous Hall effect in the Weyl semi-metal CeAlSi, specifically in its ferromagnetic phase in our DFT calculations, was studied using the Wannierization method. The Weyl points present

in this system originate from the breaking of the inversion symmetry as well as from the lack of TRS. In the presence of SOC, the positions of these Weyl points were monitored and associated with a sign change in the AHE results.

2. **Altermagnetic systems:** Recently, research was ignited with the concept of a new type of magnetism dubbed "altermagnetism" characterized by spin-splitting in the band structure regardless of its compensated magnetization constrained by symmetry. Breaking the time-reversal symmetry in altermagnetism has been an important feature in exploring macroscopic responses that were already seen in ferromagnets. In Chapter 6, CrAs, an altermagnetic candidate, is examined. The effect of SOC acts selectively on the band crossings/anticrossings producing an anomalous Hall effect.

Chapter 1 is an introduction to magnetism, spin-orbit coupling, and symmetries in condensed matter physics. Chapter 2 is devoted to the computational framework. Chapters 3 to 6 include the publications discussed, while Chapter 7 is dedicated to future outlooks and discussions.

Abstract in Polish

Nierelatywistyczne rozszczepienie spinów jest charakterystycznym zjawiskiem zazwyczaj obserwowanym w układach z naruszoną symetrią odwrócenia czasu. Jest ono przede wszystkim determinowane przez efekt magnetycznych oddziaływań wymiany Jex między spinami, które powodują różnicę energii elektronów o spinie skierowanym w górę i w dół. Rozszczepienie spinów nie może być zaobserwowane w układzie, w którym symetria odwrócenia czasu (TRS) jest zachowana, ponieważ symetria ta prowadzi do degeneracji Kramersa. Rozszczepienie spinów zachodzi niezależnie od efektów sprzężenia spin-orbita (SOC), jednak obecność tego sprzężenia może generować ciekawe efekty wynikające z interakcji ze zjawiskiem rozszczepienia spinów. Te efekty są głównym tematem niniejszej rozprawy doktorskiej. Właściwość nierelatywistycznego rozszczepienia spinów okazała się istotna w spintronice i wywiera istotny wpływ na właściwości materiałów. Na przykład może prowadzić do powstawania spinowo spolaryzowanych prądów, a wraz z SOC – do spinowego efektu Halla (SHE) i anomalnego efektu Halla (AHE). Obecność lub brak symetrii stały się jednym z najważniejszych aspektów fizyki materii skondensowanej, ponieważ stan ten pozwala na opisanie trwałych zjawisk, szczególnie w układach magnetycznych i topologicznych. Na przykład, efekt złamania symetrii inwersji przestrzennej w układach o silnym SOC jest główną przyczyną obecności oddziaływania Dzyaloshinskii-Moriya (DMI), które prowadzi do powstania chiralnych struktur magnetycznych wynikających z dynamiki spinowej. Ponadto złamanie symetrii odwrócenia czasu jest niezbędne do powstania reakcji transportowych, takich jak AHE, które nie tylko zależą od SOC, ale także mogą być kontrolowane przez jego efekty. W układach o naruszonej symetrii inwersji przestrzennej w obecności SOC występują także inne istotne efekty, takie jak efekt Rashby i Dresselhause'a. Co więcej, w materiałach topologicznych, złamanie symetrii odwrócenia czasu może prowadzić do powstawania topologicznych półmetali Weyla. Niniejsza praca obejmuje badania kilku układów, w których naruszona jest symetria odwrócenia czasu, co skutkuje nierelatywistycznym rozszczepieniem spinów widocznym w strukturze pasmowej, a poprzez oddziaływanie ze sprzężeniem spin-orbita może generować DMI i/lub AHE. Układy z naruszoną symetrią odwrócenia czasu można podzielić na dwie kategorie:

1. **Układy ferromagnetyczne:** Magnetyczne cienkie warstwy Re/Co/Pt zostały opisane w dwóch pierwszych artykułach. Układ ten generuje bardzo wysokie wartości DMI dzięki występowaniu kluczowych warunków. Symetria inwersji przestrzennej jest naruszona z powodu obecności interfejsów, a efekt SOC jest stosunkowo silny i głównie pochodzi od platyny. Artykuł przedstawiony w Rozdziale 3 jest czysto teoretyczny, oparty na obliczeniach z wykorzystaniem teorii funkcjonału gęstości (DFT), w których badany jest wpływ dostrajania grubości cienkich warstw Co i efektu wymieszania na interfejsie na ogólną dynamikę badanego układu warstwowego. Rozdział 4 zawiera opis zbiorczego badania eksperymentalnego i teoretycznego tego samego układu, które skupia się głównie na wpływie rodzaju i jakości interfejsu na wielkość DMI. Rozdział 5 omawia anomalny efekt Halla

w półmetalu Weyla CeAlSi, konkretnie w jego ferromagnetycznej fazie, z wykorzystaniem metody Wannieryzacji zastosowanej w naszych obliczeniach DFT. Punkty Weyla obecne w tym układzie wynikają z naruszenia symetrii inwersji oraz braku TRS. W obecności SOC monitorowano pozycje tych punktów Weyla, które powiązano ze zmianą znaku w wynikach AHE.

2. **Układy altermagnetyczne:** Niedawno badania wzbudziły zainteresowanie nowym rodzajem magnetyzmu, nazwanym „altermagnetyzmem," który charakteryzuje się rozszczepieniem spinów w strukturze pasmowej, niezależnie od skompensowanego namagnesowania ograniczonego przez symetrię. Naruszenie symetrii odwrócenia czasu w altermagnetyzmie było ważnym czynnikiem w badaniu makroskopowych reakcji, które były wcześniej obserwowane w ferromagnetykach. W Rozdziale 6 opisano badania CrAs, jako kandydata na altermagnetyk. Efekt SOC działa selektywnie na przecinanie/nieprzecinanie pasm, prowadząc do anomalnego efektu Halla.

Rozdział 1 jest wprowadzeniem do magnetyzmu, sprzężenia spin-orbita i symetrii w fizyce materii skondensowanej. Rozdział 2 poświęcony jest zastosowanej metodologii obliczeniowej. Rozdziały 3 do 6 zawierają omówione publikacje, natomiast w Rozdziale 7 dyskutowane są perspektywy przyszłych badań.

To the woman I have become,

Dedication and acknowledgements

My thesis stands as a tribute to those who lifted me during moments of doubt, those who embraced me as I am.

To my full-time supporter, my supervisor Carmine Autieri; for this journey would not have been possible without you.

To my family—my parents and four siblings— for your steadfast support and love which have fueled my determination. Each moment spent with you is a cherished treasure, and this dedication is but a small reflection of my gratitude.

To my best friend, Mariah, for you have been my rock through every challenge and triumph.

Finally, to my resilient country, Lebanon, in the hope that no more lives will be lost fighting for our freedom.

For you, a million times over.

I would like to express my gratitude to my colleagues Giuseppe Cuono and Ragottam Sattigeri for their assistance with scientific and technical challenges. Special thanks to Professor Andrzej Wawro for his help and guidance during these 4 years. Finally, I would like to extend my appreciation to all my collaborators including those at the Institute of Physics, the University of Białystok, and others outside Poland.

This project was supported by the Polish National Science Centre under Project No. 2020/37/B/ST5/02299

AUTHOR'S DECLARATION

I hereby certify that the work contained in this dissertation has not been submitted for consideration in any other academic awards and has been completed in accordance with the rules and guidelines of the Institute of Physics, Polish Academy of Science (IFPAN) and the Code of Practice for Research Degree Programs. Unless otherwise specified by a specific reference in the text, the work is the candidate's own contribution. Work accomplished with the assistance of or in collaboration with others is acknowledged as such. In the dissertation, only the author's viewpoints are given.

SIGNED: ..... DATE: .....

List of publications

The thesis incorporates the following papers to which I have contributed as either a primary or secondary author.

1. **Amar Fakhredine**, Andrzej Wawro, and Carmine Autieri. *"Huge Dzyaloshinskii–Moriya interactions in Pt/Co/Re thin films."* Journal of Applied Physics 135, no. 3 (2024)
2. Anuj Kumar Dhiman, **Amar Fakhredine**, Ryszard Gieniusz, Zbigniew Kurant, Iosif Sveklo, Piotr Dłużewski, Wojciech Dobrogowski, Sukanta Kumar Jena, Aleksiej Pietruczik, Carmine Autieri, Andrzej Wawro, and Andrzej Maziewski. *"Evolution of static and dynamic magnetic properties of Re/Co/Pt and Pt/Co/Re trilayers with enhanced Dzyaloshinskii-Moriya interaction"* Applied Surface Science, 679:161151, 2025
3. Alam, Md Shahin, **Amar Fakhredine**, Mujeeb Ahmad, P. K. Tanwar, Hung-Yu Yang, Fazel Tafti, Giuseppe Cuono et al. *"Sign change of anomalous Hall effect and anomalous Nernst effect in the Weyl semimetal CeAlSi."* Physical Review B 107, no. 8 (2023): 085102
4. **Amar Fakhredine**, Raghottam M. Sattigeri, Giuseppe Cuono, and Carmine Autieri. *"Interplay between altermagnetism and nonsymmorphic symmetries generating large anomalous Hall conductivity by semi-Dirac points induced anticrossings."* Physical Review B 108, no. 11 (2023): 115138

OTHER PUBLICATIONS CARRIED OUT DURING THE PH.D.

The below list includes publications that are not included in the thesis.

1. Hussain, Ghulam, **Amar Fakhredine**, Rajibul Islam, Raghottam M. Sattigeri, Carmine Autieri, and Giuseppe Cuono. *"Correlation-Driven Topological Transition in Janus Two-Dimensional Vanadates."* Materials 16, no. 4 (2023): 1649

2. Giuseppe Cuono, Ghulam Hussain, **Amar Fakhredine**, and Carmine Autieri. *"Topological Phase Diagram of $Pb_{1-x}Sn_xSe_{1-y}Te_y$ Quaternary Compound."* Acta Physica Polonica A 142, no. 4 (2022): 521-528

3. Sukanta K. Jena, Jan Kisielewski, Ryszard Gieniusz, Urszula Guzowska, **Amar Fakhredine**, Carmine Autieri, Artem Lynnyk, Aleks Pietruczik, Andrzej Maziewski, and Andrzej Wawro. *"Field angle-dependent bubble lattice formation in $Re/Co/Pt$ multilayers."* In 2023 IEEE International Magnetic Conference-Short Papers (INTERMAG Short Papers), pp. 1-2. IEEE, 2023

OTHER WORKS IN PROGRESS CARRIED OUT DURING THE PH.D.

These works were also conducted during the Ph.D. program and are currently in progress for publication.

1. Autieri, Carmine, Raghottam M. Sattigeri, Giuseppe Cuono, and **Amar Fakhredine**. *"Staggered Dzyaloshinskii-Moriya interaction inducing weak ferromagnetism in centrosymmetric altermagnets and weak ferrimagnetism in noncentrosymmetric altermagnets."* arXiv preprint arXiv:2312.07678 (2023)

2. Lim, Ji Soo, Carmine Autieri, **Amar Fakhredine**, Merit Spring, Martin Kamp, Louis Veyrat, Axel Lubk, Bernd Büchner, Michael Sing, and Ralph Claessen. *"Spontaneous Anomalous Hall Effect in $SrIrO_3$ (111) Thin Film."* Manuscript in preparation.

3. Cuono, Giuseppe, Carmine Autieri, **Amar Fakhredine**, Jan Skolimowski, Silvia Picozzi, Mario Cuoco, and Filomena Forte. *"Transition between Two Distinct Altermagnetic Phases under Modulation of the Electric Field in Orbital-Selective Altermagnet Ca_2RuO_4."* Manuscript in preparation.

Table of Contents

List of Figures

Figure **Page**

CHAPTER 1

INTRODUCTION

1.1 Magnetism

Magnetism stems from the intricate relationship between the orbital and spin properties of electrons and their interactions. Each electron carries an orbital angular momentum (l) and a spin angular momentum (s), both of which contribute to the electron's magnetic moment. The total orbital and spin angular momentum of a system with n electrons is written as:

$$L = \sum_{i}^{n} l_i \quad S = \sum_{i}^{n} s_i \tag{1.1}$$

To understand the electronic arrangement in a system of electrons such as atoms and molecules, one has to consider the Pauli exclusion principle which describes the behaviour of the half-integer particles. The principle simply states that no two electrons that share the same quantum numbers can be in the same electronic state, therefore they should at least have opposite spins. The second part of the rule is that in a single orbital, only two electrons can be accommodated. Following this rule, it is rather clear that if all the orbitals were to be completely filled, no net magnetic moment would result.

Another rule which governs the way that the orbitals should be filled is known as the first Hund's rule. It states that during the assignment of electrons, the same energy should be distributed on each orbital before the electrons start pairing up in the half-filled orbitals. In other words, all the singly occupied orbitals will have the same spin which maximizes S. The second point of the rule, is that the highest value of L results in the lowest in energy. The total angular momentum, J = L + S, has the lowest value when the electronic arrangement has less than half-filled shells, while it is maximized if it is more than half-filled. This explains the magnetic moment found in 3d and 5d transition metals with partially filled shells, which results from the spin and orbital

momentum components.
Faraday categorized all the substances under his study into paramagnetic and diamagnetic. Paramagnetic substances were those attracted by an electromagnet, while the term diamagnetic was used for those repelled by it. In paramagnets, the atomic dipoles point in randomized directions in the absence of a field, resulting in no magnetization in any direction. The spins tend to align parallel to the external magnetic field enhancing the overall magnetization in the same direction and lowering the energy of the system. At low temperatures, where the thermal agitation is less effective, the Curie law was discovered where the susceptibilities of many systems follow the equation $\chi = \frac{C}{T}$. In diamagnetism, on the other hand, the atomic spins align such that the magnetization points as opposed to the applied magnetic field. In both paramagnets and diamagnets, the total magnetic moment is absent in a zero-applied field. Diamagnetic materials generate a weak, opposing magnetic moment in response to an external magnetic field, in accordance with Lenz's rule, which states that the direction of an induced current will oppose the change in magnetic flux. This causes diamagnets to be repelled by an external magnetic field. Ferromagnetic materials, such as cobalt, nickel,iron, and gadolinium are also attracted by an electromagnet but with a much stronger coupling interaction where the atomic spins interact with one another trying to align in the same direction[4]. This strong interaction creates an order that persists even with no applied field and results in a permanent magnetic moment[5].

While parallel alignment of the spins is typical in ferromagnets, it is not the only present configuration in magnetic systems. In 1936, Louis Néel introduced the theory of antiferromagnetism. In antiferromagnets, the magnetic moments form two equal but opposite sublattices defined as M_A and M_B which cancels out the total magnetization. The phase transition of such systems occurs at a specific temperature known as the Néel temperature T_N where the spins start to order. In other systems, the sublattices M_A and M_B are unequal giving rise to a finite magnetization, and this is known as ferrimagnetism. In ferrimagnetic systems, a net magnetic moment is also expected stemming from the difference in the magnitude of the moments. What is mentioned so far about the ordered states are known as collinear magnetic configurations, however, some systems do not have collinear magnetic moments but are known as helical or spiral structures[6]. Some other noncollinear magnetic systems having random directions of the moments are known as "spin glass", in which the magnetic atoms create a frustrated interaction between the spins.

Researchers have been outraged recently by the emergence of a new type of magnetism in which the magnetization densities obey the non-relativistic spin symmetry making a combination of two-fold spin-space rotations and a real-space rotation. Unlike, say antiferromagnetism where the spin-up and spin-down sublattices are simply related by translation and inversion symmetry, in altermagnets they are connected only through proper or improper rotations and symmorphic or nonsymmorphic symmetries. Altermagnetism combines the properties of both ferromagnets and antiferromagnets in the sense that such systems have no net magnetization but still show a band

splitting in the absence of spin-orbit coupling (SOC) as a consequence of a broken time-reversal symmetry[7]. This non-relativistic spin-splitting is sizable and can even exceed that of a bulk crystal with a heavy element. In conventional antiferromagnets, the Kramer's degeneracy is protected even in the presence of SOC, however, in altermagnets it is lifted even when no SOC nor inversion-symmetry breaking is present[8]. The schematic diagram presented in Fig.1.1 shows how to differentiate altermagnets from conventional antiferromagnets. One common mistake in the search for an altermagnetic behavior is observing the non-relativistic spin splitting (NRSS) at the time-reversal invariant momenta (TRIM) points in the band structure which is not a property of an altermagnet. TRIM points in altermagnetic systems still preserve the identity of Kramer's degeneracy even in the presence of SOC as long as no ferromagnetism is generated. Some antiferromagnets show spin-splitting as in Fig.1.1, however, their sublattices are not connected by any crystal symmetry which classifies them differently than antiferromagnets.

1.2 Spin-orbit coupling

Spin-orbit coupling (SOC) interaction is an important phenomenon in magnetism and is responsible for many other aspects such as band topology, magnetocrystalline anisotropy and magnetostriction. It arises from relativistic effects which are described by the famous equation of Dirac, and it links the motion of a particle in a crystal to its spin, making the energy in the

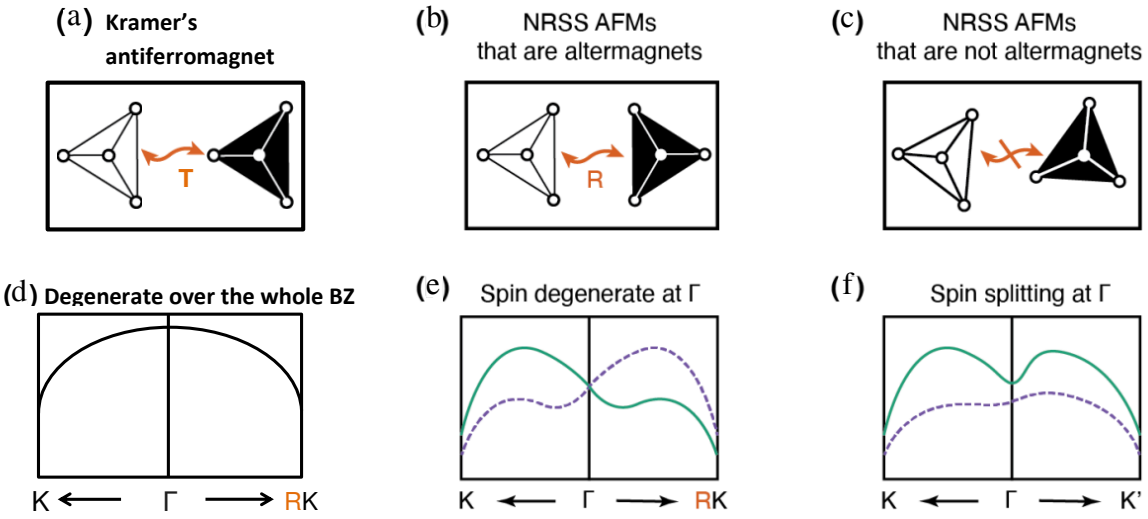

Figure 1.1: Schematic diagram of the behavior of the band structure in the case of a conventional Kramer's antiferromagnet (a,d), altermagnet (b,e), and neither an altermagnet nor an antiferromagnet (c,f). The figure is adapted from reference [1].

Hamiltonian as:

$$H_{SO} = \lambda \vec{L} \cdot \vec{S} \tag{1.2}$$

where λ is known as the SOC parameter.
The SOC causes a shift in the energy levels of an electron as it enters an electric field caused by the nucleus of an atom coupled by its spin to the effective magnetic field via the equation:

$$\hat{H} = -\hat{\vec{\mu}}_S \cdot \vec{B} \tag{1.3}$$

where $\hat{\vec{\mu}}_S = -\frac{g_s \mu_B}{\hbar} \hat{\vec{S}}$ is the spin magnetic dipole, where g_s is the spin-g-factor of the electron which is equal to 2, and $\mu_B = \frac{e\hbar}{2m}$ is the Bohr magneton[9].
The effect of SOC scales with the power four of the element's atomic number Z^4, therefore, when the nucleus of an atom gets bigger the SOC greatly increases[10]. Spin degenerate levels can be split by the effect of SOC into parallel and antiparallel. The degeneracy of states with the same orbital can be lifted with opposite spins in a free atom, but in solids, this splitting is not allowed due to the crystal symmetry. The time-reversal symmetry imposes that the Hamiltonian stays invariant under the reversal of the time's direction. This can also be reflected in the spin, an internal degree of freedom. Time reversal symmetry usually preserves Kramer's degeneracy in half-integer spin systems. Kramer's degeneracy is lifted only in the case where time-reversal symmetry is broken such as the application of external magnetic fields. At any energy E and point k satisfies the following equation:

$$E(k,\uparrow) = E(-k,\downarrow) \tag{1.4}$$

This degeneracy is unaffected by the inclusion of SOC in the Hamiltonian. If the system preserves inversion symmetry, meaning that the crystal lattice remains unchanged when $\vec{r} \rightarrow -\vec{r}$ we will get:

$$E(k,\uparrow) = E(-k,\uparrow) \;\; and \;\; E(k,\downarrow) = E(-k,\downarrow) \tag{1.5}$$

We can see that from the combination of both symmetries designated by equations 1.4 and 1.5 spin splitting is not possible since they yield the following constraint:

$$E(k,\uparrow) = E(k,\downarrow) \tag{1.6}$$

We can conclude that at least one of the symmetries should be broken to observe the spin-splitting caused by SOC.
The electric field generated by the positively charged nucleus results in the intrinsic spin-orbit coupling. However, other types of spin-orbit coupling can arise due to different electric field sources. The Dresselhaus spin-orbit coupling[11] occurs in systems with broken inversion symmetry while the Rashba[12] spin-orbit coupling arises in systems with broken time-reversal along a high symmetry axis symmetry. In systems where the time-reversal symmetry is broken, the SOC can induce several magnetic effects and interactions such as the Dzyaloshinskii-Moriya interaction (DMI) and the anomalous Hall effect (AHE).

1.3 Dzyaloshinskii-Moriya interaction

In 1958, Dzyaloshinskii demonstrated that in the thermodynamic theory of magnetic systems, spin-orbit coupling introduces both symmetric and antisymmetric terms in the spins[13]. While the symmetric terms contribute to magnetocrystalline anisotropy and can renormalize the magnetic exchange, the antisymmetric term enables a relativistic weak ferromagnetism (via spin canting) even in centrosymmetric systems with zero non-relativistic magnetization if time-reversal symmetry is broken. An elegant theory for those systems with zero non-relativistic magnetization and broken time-reversal symmetry were presented in 2022[7]. It was shown that these systems are non-conventional due to their even-parity wave in the k-space, these systems were named altermagnets to emphasize their difference from conventional antiferromagnets which preserve the time-reversal symmetry and consequently Kramers degeneracy. The Dzyaloshinskii-Moriya interaction is an antisymmetric exchange interaction that occurs between spins and may lead to non-collinear and/or chiral spin textures. It appeared as a consequence of adding the effect of SOC to the Heisenberg model. Unlike the collinear exchange interaction known as the *Heisenberg* interaction given as:

$$\hat{H} = -J_{ij} \ \ \vec{S}_i \cdot \vec{S}_j \tag{1.7}$$

which favors parallel spin alignments, the DMI favors a perpendicular one and is calculated from the product of two spins:

$$\hat{H}_{DMI} = \vec{D_{ij}} \cdot (\vec{S}_i \times \vec{S}_j) \tag{1.8}$$

The vector $\vec{D_{ij}}$ is the atomic DMI vector, while $\vec{J_{ij}}$ in the Heisenberg equation is the exchange constant. The origin of such an interaction is the absence of the inversion symmetry and the existence of SOC, typically occurring at the interface between a ferromagnetic material and a heavy metal. However, the DMI can also occur in bulk materials that inherently lack inversion symmetry, such as in chiral magnets like FeGe and MnSi[14, 15]. In these bulk materials, the crystallographic structure itself breaks inversion symmetry, allowing the DMI to emerge without the need for an interface.

The interfacial DMI was initially understood as weak ferromagnetism in antiferromagnetic insulators but later generalized to other systems[13, 16]. This interaction can stabilize the formation of skyrmions which has been verified experimentally, and these are magnetic textures which behave like particles having a size of a few nanometers. Their small size allows them to be easily manipulated which makes them very useful for abacus-type applications like information storage and logic functions[17]. There are two types of skyrmions depending on the direction of the rotation affected by different symmetries named as Bloch type and Néel type. Skyrmions are defined by the topological Skyrmion number S, which characterizes the emergent magnetism arising from the winding of the spins in the skyrmion configuration around the unit sphere. In

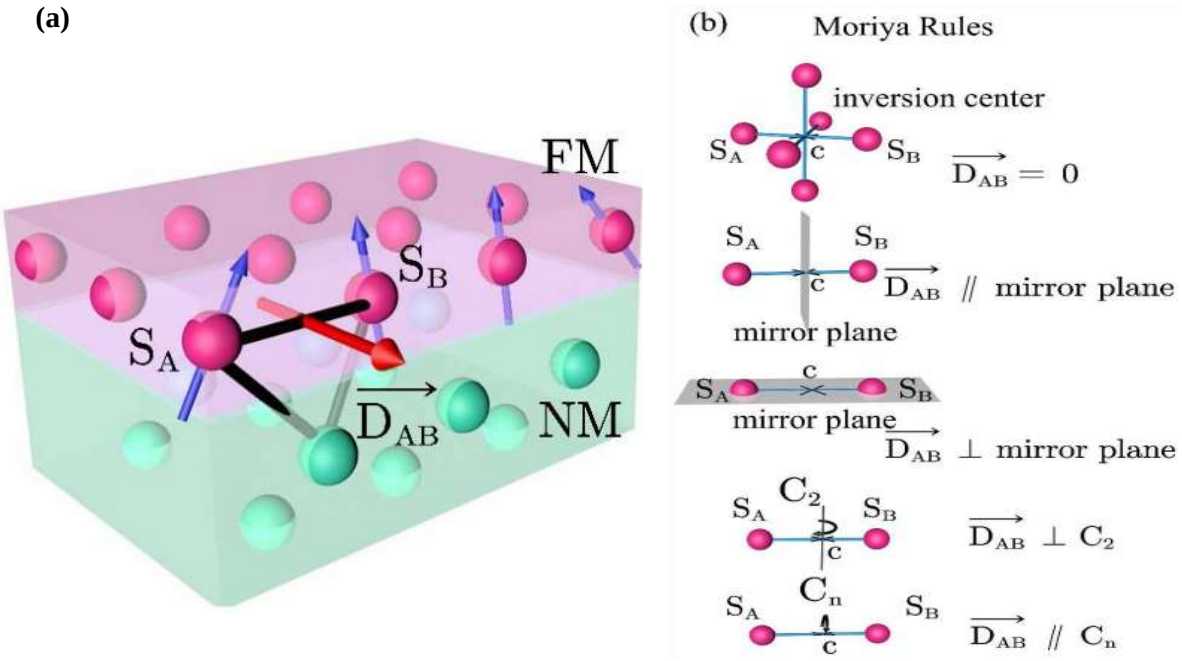

Figure 1.2: (a) Schematic diagram of the direction of the DMI vector in a layered structure of a nonmagnet (NM) and a ferromagnet (FM) (b) The Moriya rules. The figures are taken from reference [2].

the two-dimensional limit, this number is defined as :

$$S = \frac{1}{4\pi}\int \vec{m}\cdot(\partial_x\vec{m}\times\partial_y\vec{m})d_x d_y = \pm 1 \tag{1.9}$$

This number is zero for a ferromagnet or an antiferromagnet. The direction of the DMI vector $\vec{D_{ij}}$ is determined by the Moriya rules[16], but in the case of the interfacial DMI where a ferromagnetic material is placed on top of a non-magnetic material with strong spin-orbit coupling, then the direction of the vector is perpendicular to the triangle formed by the two spins and the third non-magnetic neighboring atom as shown in Fig.1.2.
Moriya has come up with five criteria that relate the crystal symmetry effect to the DMI[2]. Assuming that two magnetic ions have positions at points A and B, where the center is labeled by C then:

1. If the center C is also an inversion center, then $\vec{D}_{ij} = 0$.
2. If a mirror plane perpendicular to the line AB passes through the center C, then $\vec{D}_{ij} \parallel$ mirror plane or $\vec{D}_{ij} \perp$ AB.
3. If the mirror plane contains both the A and B points, then $\vec{D}_{ij}$ is $\perp$ to the mirror plane.
4. If there is a two-fold rotation axis $\perp$ to AB which passes through C then $\vec{D}_{ij} \perp$ to the two-fold rotation axis.

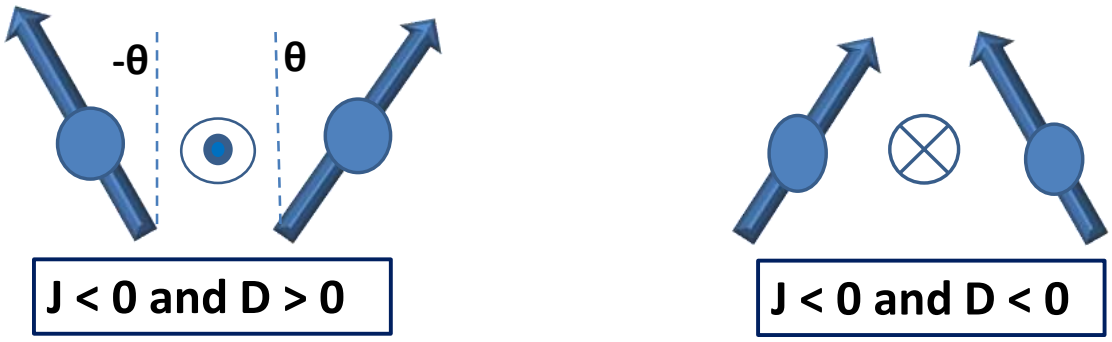

Figure 1.3: Competition between the DMI interaction D and the exchange interaction J.

5. If there is an n-fold rotation axis along the AB line, then $\vec{D}_{ij}$ is ∥ to AB.

1.4 Staggered Dzyaloshinskii-Moriya interaction

The staggered form of the Dzyaloshinskii-Moriya interaction occurs when the sign of the DMI alternates for instance along a chain of atoms. In this situation, the DMI interaction on different magnetic sublattices varies resulting in a modulated type of interaction. In the traditional form of the DMI discussed in Section 1.3, in a system with inversion symmetry the total DMI is null ($\sum_{i,j} D_{i,j} = 0$) and this makes any DMI interaction between two spins null as well ($D_{i,j} = 0$). In the case of staggered DMI, while the inversion symmetry remains unbroken, the DMI vector between sites can still be nonzero ($D_{i,j} \neq 0$). Depending on the sign of the DMI, we have different canting as depicted in Fig. 1.3. A uniform DMI in a ferromagnetic system can create chiral magnetic structures as illustrated in Fig. 1.4(a), while the uniform DMI is ineffective in antiferromagnets as seen in the top part of Fig. 1.4(b). This staggered DMI can induce a weak ferromagnetic/ferrimagnetic behavior in crystal systems in the presence or absence of inversion symmetry as can be seen in Fig.1.4 (b). The weak ferromagnetism (defined as ferromagnetism driven by spin-orbit coupling) can appear only in altermagnets since the spin-orbit needs a system with broken time-reversal symmetry to create ferromagnetism. In such systems, the weak ferromagnetism/ferrimagnetism appears as an interplay between the space group, magnetic order, and the direction of the Néel vector. As of the submission of this thesis, a preprint of our study on this topic is available on arXiv[18].

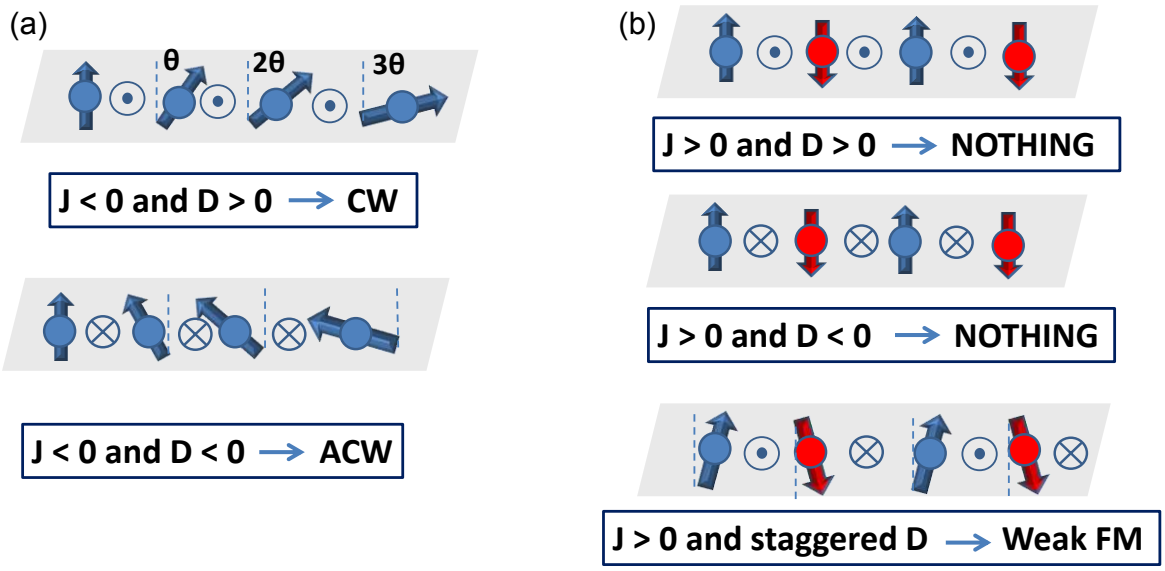

Figure 1.4: Competition between the DMI interaction D and the exchange interaction J in (a) ferromagnets and (b) altermagnets.

1.5 Anomalous Hall effect

The Hall effect, which was discovered in 1881 by Hall[19], and discussed that a conductor carrying a current under the effect of a magnetic field undergoes the effect of the Lorentz force which shifts the electrons to one side, was later overcome by a stronger effect found in ferromagnets [20]. This stronger effect is now known as the anomalous Hall effect (AHE) and it is related to the topology and to the geometry of the system, such as the Berry curvature. The AHE occurs in systems with broken time-reversal symmetry under the inclusion of SOC which results in intrinsic effects related to the band structure of the material and extrinsic effects related to the lattice impurity. The equation for the Hall's resistivity of ferromagnets is empirically known to follow the equation:

$$\rho_{xy} = R_0 B + R_s M_Z \tag{1.10}$$

where the second part $R_s M_z$ is related to the anomalous Hall coefficient originating from the fact that the current exists even in the absence of a magnetic field and is related to the magnetization M_z.

An observation made by Karplus and Luttinger in the 1950's[21] showed that spin splitting of the bands in the presence of spin-orbit coupling (SOC) can contribute to Hall conductivity. Another significant observation was made by Smit[22], who demonstrated that the anomalous Hall effect (AHE) can occur only through impurity scattering, where the skew scattering mechanism was introduced. In this mechanism, spin-up and spin-down electrons are scattered asymmetrically by the potential of the impurity under the influence of SOC. Another mechanism by Berger was

later introduced[23] called the side jump causing the spin-up and spin-down electrons to undergo a lateral shift where the wave vector is conserved.
The intrinsic contribution to the AHE is related to the Berry curvature[24] of the Bloch electrons which plays a similar role of an effective magnetic field in the real space. This field is derived from a vector potential in momentum space known as the Berry connection denoted as $\vec{A}_n$ representing the local phases of the wave function and is calculated using this equation:

$$\vec{A}_n = i\langle u_n|\nabla_k|u_n\rangle \tag{1.11}$$

where u_n is the lattice periodic part of the Bloch wave.
The Berry curvature is then related to the Berry connection through:

$$\vec{\mathscr{F}}_n = \vec{\nabla}_{\vec{k}} \times \vec{A}_n \tag{1.12}$$

One can think about the Berry curvature as a geometrical feature of an energy band that describes the evolution of the eigenstates of the system in response to variation to changes in the system's parameters such as the momentum. Lastly, the intrinsic AHE is related to the Berry curvature by the following equation:

$$\sigma_{xy} = -\frac{e^2}{h}\int \frac{d^2k}{2\pi}\sum_n f_{FD}^n \mathscr{F}_n \tag{1.13}$$

where f_{FD}^n is the Fermi-Dirac distribution function.

1.6 Weyl Semimetals

Weyl fermions discovered by Hermann Weyl, existed as massless particles in the Dirac equation in 1929 [25, 26]. A Weyl semimetal is a state that hosts Weyl fermions. A Weyl semimetal is a material in which the electronic bands touch at discrete points in momentum space, where the energy is cone-like, rather than being separated by an energy gap as in conventional insulators or semiconductors. The Weyl equation governs the energy excitations near the touching points. These points, known as Weyl points, arise in crystals that lack inversion symmetry and are characterized by low-energy excitations that behave like Weyl fermions. Such an observation was initially explained as "accidental" degeneracies, these band touchings are now understood to be topologically protected by recent advances in band theory, meaning they are robust against perturbations. In other words, at any generic point k in the BZ, a two-fold degenerate band crossing of non-degenerate bands occurs giving Weyl semimetals their distinct topological nature[27]. Weyl points act as sources and sinks to the Berry curvature as they are assigned to a topologically protected chiral charge of +C or -C, and they can occur in systems where either time-reversal symmetry or inversion symmetry is broken. The charge C is an integer number which is usually 1 or 2, this is also the Chern number of Hamiltonian projected from cutting the plane between the

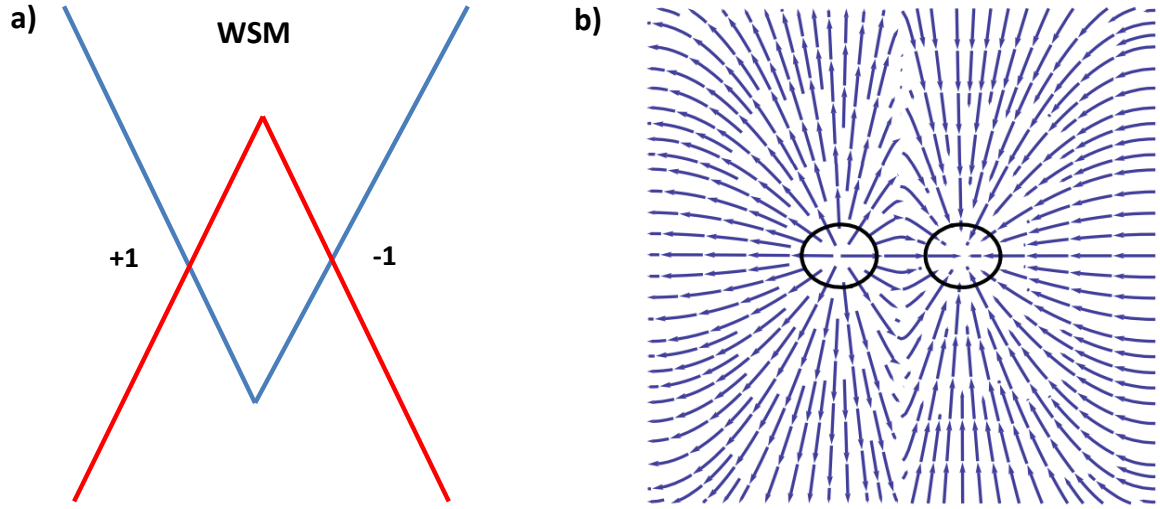

Figure 1.5: (a) Schematic diagram of two bands forming two Weyl points of chirality +1 and -1 (b) The field lines of the Berry curvature around the two Weyl points. The figure in b) is taken from reference [3].

Weyl fermions[28]. The energy around the Weyl point is characterized by the linear dispersion as:

$$H = v\ \vec{\sigma} \cdot \vec{k}. \tag{1.14}$$

where v is related to the chirality of the Weyl point, σ is the Pauli matrix and k is the crystal momentum. The realization of the Weyl semimetal with a pair of Weyl nodes exists only in the case where the time-reversal symmetry is broken, since the Berry curvature vanishes in a system where both time-reversal symmetry and inversion symmetry is preserved[29]. In systems where both symmetries are conserved, the situation will result in double degeneracy at all k which would generate Dirac fermions as a result of the superposition of two Weyl nodes. Weyl semimetals are widely known for giving rise to the anomalous Hall effect due to their distinct Berry curvature properties. The separation of two Weyl nodes having opposite chirality, which is analogous to monopoles in the momentum space, produces the Berry flux contributing to the AHE. This is similiar to a dipole's electric field with a non-zero defined value at a large distance [3, 30] as demonstrated in Fig.1.5.
Other types of protected nodal points that will be discussed are the semi-Dirac points. When the time-reversal symmetry (TRS) is broken, two pairs of Weyl points emerge from the semi-Dirac points[31].

1.7 Semi-Dirac Semimetals

A semi-Dirac cone was very recently observed in electron systems, where a point near the Fermi-surface in a 2D system has a linear dispersion relation along one momentum direction

but quadratic in the orthogonal direction near the band-touching points[32]. This property of a semi-Dirac point combines the characteristic of massless quasi-particles along one k direction and an effective mass-like along another direction[33, 34]. Such materials that exhibit the coexistence of massless and massive Dirac fermions are known as Semi-Dirac semi-metals. The semi-Dirac dispersion relation is given by:

$$\epsilon_k = \pm\sqrt{\left[\frac{k_x^2}{2m}\right]^2 + [v{k_y}^2]} \tag{1.15}$$

In this equation, to fulfill the property of a semi-Dirac point, the effective mass m applies along the k_x direction whereas the velocity applies to the k_y direction where the quasi-particles are massless[35]. The ± sign is related to the conduction band or to the valence band.
Semi-Dirac points are often protected by nonsymmorphic symmetries which are characterized by a rotational symmetry or a mirror reflection combined with a fractional lattice symmetry. This kind of symmetry protects the semi-Dirac points from being lifted upon the effect of spin-orbit coupling. As has been mentioned, the TRS breaking leads to two Weyl points emerging from a semi-Dirac point. In such a scenario, an additional breaking of the inversion symmetry can induce a gap opening which triggers the Berry curvature consequently leading to an enhanced anomalous Hall effect.

1.8 Non-symmorphic symmetries

The presence of non-symmorphic symmetries in a crystal structure plays an important role in protecting novel phases, which include insulating phases and semi-metallic phases[36]. Non-symmorphic symmetries include fractional translation symmetries, which could be either a glide reflection symmetry or a screw-axis rotation visualized as schemes in Fig.1.6. In such symmetries, the mirror reflection or the rotation changes the crystal where the role of the fractional translation is to keep the crystal invariant. The existence of non-symmorphic symmetries in a crystal structure leads to the emergence of non-trivial band structures designated by symmetry-protected non-trivial band crossings, such as Dirac points in semimetals.[37]. In such cases, in the presence of SOC, the degeneracy is lifted at all k except at some isolated points which form a nodal line[38].
Let us consider the two-fold unitary nonsymmorphic symmetry denoted by $G(k)$:

$$G(k) = \begin{pmatrix} 0 & e^{-ik} \\ 1 & 0 \end{pmatrix} \tag{1.16}$$

The Hamiltonian upon the action of $G(k)$ must satisfy:

$$G(k)H(k)G^{-1}(k) = H(k) \tag{1.17}$$

G(k) also anti-commutes with the Pauli matrix σ_3 which gives:

$$H(k) = \begin{pmatrix} 0 & q(k) \\ q^*(k) & 0 \end{pmatrix} \tag{1.18}$$

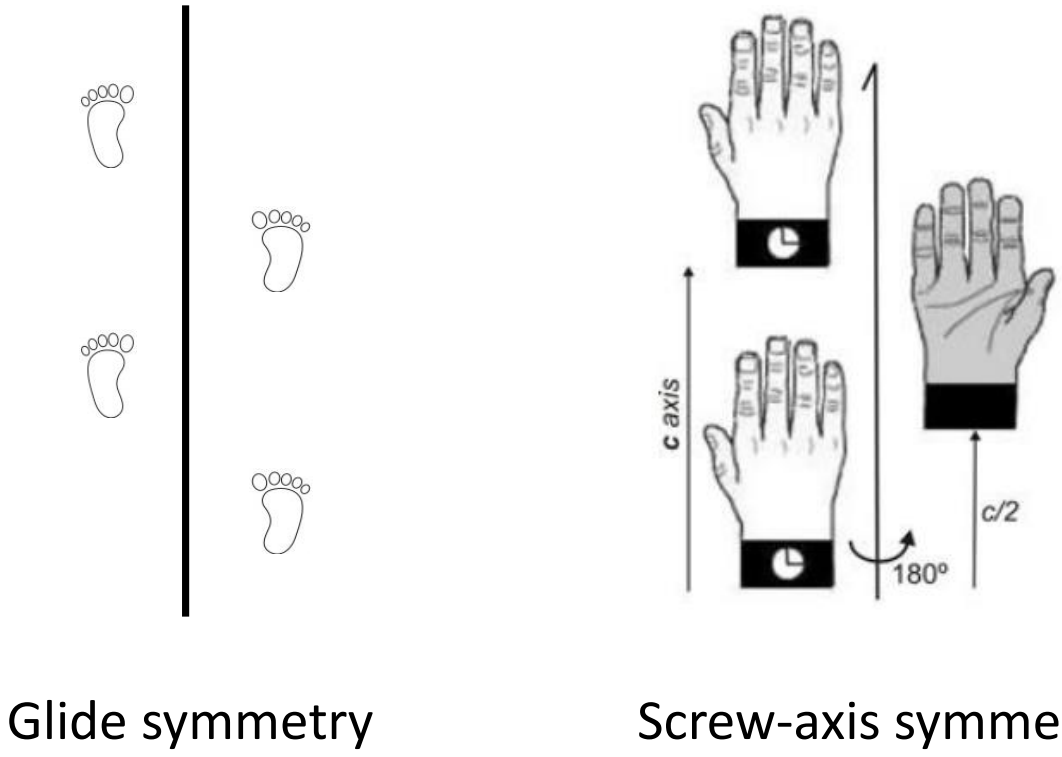

Figure 1.6: Schematic diagram of the nonsymmorphic symmetries. The glide symmetry is a mirror reflection followed by a translation, whereas the screw-axis symmetry is a rotation along an axis followed by translation.

To satisfy equation 1.17, then the following equation should apply:

$$q(k)e^{ik} = q^*(k) \tag{1.19}$$

Any function that satisfies equation 1.19 could be zero at any k in the Brillouin zone (BZ). Therefore, in such case any two-band Hamiltonian in the presence of a nonsymmorphic symmetry $G(k)$ must be gapless at a certain point. The presence of an inversion symmetry $\hat{P}$ in such a scenario assures pinning the band crossing at a certain position in the BZ which could be located at the origin or at the boundaries.

CHAPTER 2

METHODICAL APPROACH AND COMPUTATIONAL ASPECTS

All the results presented in this thesis are derived from ab initio calculations. The primary and most significant method used is Density Functional Theory (DFT), supported by Wannierization, a key technique based on the tight-binding approach and implemented through the Wannier90 code. The strength of DFT lies in its ability to predict and explain various atomic properties and behaviors without the reliability on experimental findings. Most importantly, it provides a rigorous approach to address any *interacting* problem by effectively converting it into a *non-interacting* problem which makes it easier to implement.

Chapter 2 is entirely devoted to the brief discussion of the fundamentals of DFT starting from a single electron aspect, followed by a more complex many-body problem. In the following section, the notable Kohn-Sham theory is presented along with various exchange-correlation functionals which are the the most formidable challenges within the realm of DFT. After that, we discuss the Wannierization technique and its construction starting from Bloch functions, an essential concept, which will be discussed beforehand.

2.1 Many body electron system

Any many-body electron system must be composed of a set of M atomic nuclei and N electrons where both sets occupy different positions in 3D Cartesian coordinates, let us assume that R_1,...,R_M represent those of the nuclei and r_1,...,r_k denote the position of each of the electrons at a fixed instant[39]. In such case, we should extract the eigenvalues (energies) and the eigenvectors (wave functions) from the Hamiltonian of the system, which encompasses the kinetic energies and the Coulomb interactions. Once the eigenvalues are obtained, it becomes simpler to calculate the system's total energy, forces, geometry, energy levels, charges, and other important properties

of the material being investigated. The equation below represents the total Hamiltonian of a system of electrons and nuclei:

$$\hat{H} = \hat{T}_n + \hat{T}_e + \hat{V}_{n-n} + \hat{V}_{e-e} + \hat{V}_{n-e} \tag{2.1}$$

where $\hat{T}_n$ and $\hat{T}_e$ represent the kinetic energies of the nuclei and electrons respectively, $\hat{V}_{n-n}$ is the Coulomb repulsion potential which is due to the nuclei, $\hat{V}_{e-e}$ is the potential due to the electrons, and finally $\hat{V}_{n-e}$ is the potential due to the interaction between the electrons and the nuclei.

These operators are defined by the mass of the respective particles and their positions, where m is the mass of an electron and M is that of a nucleus. Substituting each potential by its definition, the equation (2.1) will become :

$$\begin{aligned}\hat{H} = &\sum_{\alpha=1}^{K} \frac{(-i\hbar\nabla_{R\alpha})^2}{2M_\alpha} + \sum_{\alpha=1}^{N} \frac{(-i\hbar\nabla_i)^2}{2m} + \sum_{\alpha,\beta=1;\alpha<\beta}^{K} \frac{Z_\alpha Z_\beta e^2}{|\vec{R}_\alpha - \vec{R}_\beta|} \\ &+ \sum_{i,j=1;i<j}^{N} \frac{e^2}{|\vec{r}_i - \vec{r}_j|} - \sum_{\alpha=1}^{K}\sum_{i=1}^{N} \frac{Z_\alpha e^2}{|\vec{R}_\alpha - \vec{r}_i|}\end{aligned} \tag{2.2}$$

where i,j and α,β run for electrons and nuclei respectively. In regular quantum mechanics, one must solve the presented Schrödinger equation in its simplest form as in (2.3) to understand the behavior of the quantum system and to calculate its energies and wavefunctions.

$$\hat{H}\Psi = E\Psi \tag{2.3}$$

In the latter equation, Ψ is a set ψ_n of eigenstates which are solutions for the Hamiltonian where each eigenstate has an associate energy E_n that satisfies the equation. To plug in the Hamiltonian written in (2.2) into equation (2.3), the situation becomes more challenging and requires certain approximations that allow us to solve the problem.

Born Oppenheimer

Electrons are at least three orders of magnitude lighter than protons and neutrons so they can move at much higher velocities than the nuclei. This brings us to the conclusion that at fixed positions, the kinetic energy of the nuclei can be neglected and their respective potential can be treated as a constant value. This is known as the *Born-Oppenheimer* (BO) approximation[40, 41] and it is the first simplification of our system where it allows us to separate the wave function into a product of ionic and electronic parts such as:

$$\Psi = \Psi^{\mathrm{n}}_{\mathrm{k}}(\vec{R}_\alpha)\Psi^{\mathrm{e}}_{\mathrm{k}}(\vec{r}_i,\vec{R}_\alpha) \tag{2.4}$$

where the $\Psi^{\mathrm{n}}_{\mathrm{ik}}$ is a nuclear wave function and $\Psi^{\mathrm{e}}_{\mathrm{k}}$ is the electronic wave function which also relies on the position of nuclei.

With this definition of the total wave function, we can now substitute it in the Schrödinger

equation only to find that the part related to the potential due to the attraction of electrons and nuclei would be more complicated because it should be applied on both of the separated wave functions.

$$[\hat{T}_e + \hat{V_{e-e}}] + \hat{V_{n-e}}]\Psi^{\mathrm{e}}_{\mathrm{k}}(\vec{r}_i, \vec{R}_\alpha) = E_k(R-\alpha)\Psi^{\mathrm{e}}_{\mathrm{k}}(\vec{r}_i, \vec{R}_\alpha) \tag{2.5}$$

Equation (2.5) is indeed now an electronic Schrödinger equation which depends also on the positions of the nuclei. This is the main point of the BO approximation where it allows us to calculate the electronic structure of a molecule without any interference of the quantum mechanics of the nuclei.

Hartree-Fock approximation

Although the BO approximation is sufficient for situations where the nuclear motion is slow, the difficulty to address the electron-electron effects remains. In such cases, the Hartree-Fock (HF) approximation is introduced to account for the correlation of electrons into the electronic wave functions[42]. HF basically defines an initial ansatz that the multi-electron wavefunction is a product of all wave functions of the electrons present in the system[43] . The ground state of the many body electron wave-function of the system assuming that we have i electrons can be described as:

$$\Psi^{\mathrm{e}}_0(\vec{r}_i\sigma_1, ...\vec{r}_N\sigma_N) \approx \phi_{1.....N}(\vec{r}_i\sigma_1, ...\vec{r}_N\sigma_N) \tag{2.6}$$

The set of ϕ_i represents the single wave-functions of electrons, where σ_i denotes their spins and $\phi_{1.....N}$ is the ground state that can be obtained using the variational principle. The most important part of the HF approximation is that the complex many-body wave function is given by a Slater determinant of the spin orbitals such as :

$$\Psi_{\mathrm{HF}} = \begin{vmatrix} \phi_1(x_1) & \phi_2(x_1) & \phi_3(x_1) & \cdots & \phi_N(x_1) \\ \phi_1(x_2) & \phi_2(x_2) & \phi_3(x_2) & \cdots & \phi_N(x_2) \\ \vdots & \vdots & \vdots & \ddots & \vdots \\ \phi_1(x_N) & \phi_2(x_N) & \phi_3(x_N) & \cdots & \phi_N(x_N) \end{vmatrix} \tag{2.7}$$

here x denotes the space and spin coordinates of each single wave function. This approximation imposes that the electronic wave function must be antisymmetric for any exchange between two electron positions according to the Pauli exclusion principle.

$$\Psi^e(x_1, x_2, ...x_i, ..., x_j, ...x_N) = -\Psi^e(x_1, x_2, ...x_j, ..., x_i, ...x_N) \tag{2.8}$$

In order to evaluate the Hartree-Fock equations, the expectation value of the Hamiltonian should be considered for the wave functions $\phi_{1...N}$. The HF equations have a similar structure to the ordinary single-particle Schrödinger equation but instead, the total single particle potential in the HF equations is non-local and consists of two terms:

The Hartree (direct Coulomb) potential :

$$v_H(r) = \int \frac{d^3r'}{|\vec{r} - \vec{r'}|} \sum_{\sigma'=\uparrow,\downarrow} \sum_{j \neq i} |\phi_j(\vec{r'}, \sigma')|^2 \tag{2.9}$$

and the exchange potential :

$$V_x^{HF}(\vec{r}\sigma, \vec{r'}\sigma') = \frac{e^2}{|\vec{r} - \vec{r'}|} \sum_{j=1}^{N} \phi_j(\vec{r\sigma}) \phi_j^*(\vec{r'}\sigma') \tag{2.10}$$

The potentials and the states ϕ_i are treated through a self-consistent calculation starting from an initial guess of the total potential. They are improved consequently after each cycle when potentials are then calculated from ϕ_i states. This iterative process stops as soon as the required accuracy is achieved.

In the Hartree-Fock approach, each electron experiences an average field of the complete electron cloud, while the actual motion of electrons depends via the Coulomb repulsion on the positions of all electrons. To include this Coulomb correlation in the many body wave function, we have to realize a complete solution that incorporates both occupied and unoccupied states instead of the single Slater determinant. The developed wave function then could be written as such:

$$\psi_k(\vec{r}_1\sigma_1, ...\vec{r}_N\sigma_N) = \sum_{i_1,...,i_N} C^k_{i_1...i_N} \phi_{i_1}(\vec{r}_1\sigma_1)\phi_{i_2}(\vec{r}_2\sigma_2)\ldots\phi_{i_N}(\vec{r}_N\sigma_N) \tag{2.11}$$

Then, we expand the single-particle orbitals in terms of a finite set of basis functions, let's call it η_k such that:

$$\phi_i(\vec{r}\sigma) = \sum_{k=1}^{M} b_{i,k_\sigma} \eta_k(\vec{r}) \tag{2.12}$$

If we use the matrix elements $\langle \eta_k / \eta_l \rangle$, we could determine the expansion coefficients $b_{i,k\sigma}$ and $C^k_{i_1...i_N}$. For an effective single-electron problem, the equation looks like:

$$\sum_{l=1}^{M} \sum_{\sigma'} [\langle \eta_k \left| -\frac{(-i\hbar\nabla)^2}{2m} \delta_{\sigma,\sigma'} + v_{eff}\sigma,\sigma' \right| \eta_l \rangle - \epsilon_i \langle \eta_k | \eta_l \rangle] b_{i,l\sigma'} = 0 \tag{2.13}$$

where $v_{eff}\sigma\sigma'$ is the potential felt by the electrons of the system.

The challenge lies in handling the scaling of a many-body electron system, as the scaling factor M is directly proportional to the total number of electrons N. This implies that each additional electron requires an additional basis function to represent it. As a result, a method capable of efficiently addressing these complexities is needed—one that can reduce the many-body problem into an effective single-electron, non-interacting system, while also accounting for electron correlations and the Hartree-Fock approximation. A powerful approach that addresses this is Density Functional Theory (DFT), which replaces wave functions with the electron density n in real space.

2.2 Essentials of Density Functional Theory (DFT)

The concept of DFT is to reduce the complications of a given system and the scaling factors by simply introducing the idea of treating real-space electron densities instead of the k-dependent wave functions[44]. This means that instead of describing our ground state by an overlap of the electron orbitals, we define it as follows:

$$n(\vec{r}) = \langle \psi_0 | \hat{n}(\vec{r}) | \psi_0 \rangle = N \sum_{\sigma_1,.....\sigma_N} \int d^3_{r_2}.....d^3 r_N \left| (\vec{r}_1\sigma_1,.....\vec{r}_N\sigma_N)|\psi_0\rangle \right|^2 \tag{2.14}$$

Hohenberg-Kohn Theorem

The Hohenberg-Kohn theorem[45] is the heart of DFT since it determines uniquely all the properties of a system, in addition to the energy and the wave function of the ground state as a function of the electron density. The Hohenberg-Kohn idea is built upon two fundamental theorems:

- The ground-state energy, as derived from Schrödinger's equation, is a unique functional of the electron density. In other words, the electron density fully determines the energy and all other properties of the system.
- The true electron density is the one that minimizes the total energy functional. This minimizing electron density corresponds to the exact solution of the Schrödinger equation for the system's ground state.

The idea of a functional is basically to define a certain value from a function, such as the ground state energy E which would be *[E(n(r))]* where *n(r)* is the electron density. Applying this concept can grant us a solution by which instead of dealing with a 3N variables system, one could deal with 3 variables of the real space. To address the theorems, let us consider the total Hamiltonian of a system of interacting electrons:

$$\hat{H} = \hat{T} + \hat{V}_{ext} + \hat{V}_{ee} + \hat{V}_{ion} \tag{2.15}$$

Here $\hat{T}$ is the kinetic energy operator, $\hat{V}_{ext}$ is the external potential energy operator, $\hat{V}_{ee}$ is the potential energy operator of the electron-electron repulsion, and $\hat{V}_{ion}$ is the potential energy operator of the ions. The energy functional would result in a well-known analytical form as follows:

$$\begin{aligned} E[\psi_k] &= \langle \psi_k | \hat{H} | \psi_k \rangle \\ &= \frac{\hbar^2}{2m} \sum_{\sigma=\uparrow,\downarrow} \int d^3 r \hat{\psi}^\dagger(\vec{r}\sigma) \nabla^2 \hat{\psi}(\vec{r}\sigma) \\ &\quad + \int V(\vec{r}) n(\vec{r}) d^3 r + \frac{e^2}{2} \int \int \frac{n(\vec{r}) n(\vec{r'})}{|\vec{r} - \vec{r'}|} d^3 r d^3 r' + E_{ion} \end{aligned} \tag{2.16}$$

This energy functional includes the electronic kinetic energies, the Coulomb interactions between the electrons and the nuclei, the Coulomb energy between electrons themselves, and finally between the nuclei. This is one part of the energy functional, the other part is the exchange-correlation functional which remains unknown and includes the interactions of particles at a quantum scale. The picture of solving a problem using the DFT tool so far is still unclear, and this is where Kohn-Sham equations and its role appears.

Kohn Sham equations

The Kohn-Sham (KS) formalism was the first to make DFT an easily accessible tool for calculations starting from a simple fictitious system of non-interacting electrons[46]. The idea of Kohn-Sham was to introduce equations that involve only a single electron wave function, where the first equation looks somehow similar to Schrödinger's equation and has the form :

$$\left[\frac{h^2}{2m}\nabla^2 + V(\vec{r}) + V_H(\vec{r}) + V_{XC}(\vec{r})\right]\psi_i(\vec{r}) = \epsilon_i\psi_i(\vec{r}) \tag{2.17}$$

where $\psi_i(\vec{r})$ is the wave function of a single electron which depends on three spatial variables only.

The potential $V(\vec{r})$ here is the same potential that is responsible for the interactions between electrons and nuclei. The next potential $V_H(\vec{r})$ is the Hartree potential which has the following form:

$$v_H(\vec{r}) = e^2\int\frac{n(\vec{r'})}{|\vec{r}-\vec{r}'|}d^3r' \tag{2.18}$$

This potential is a self-consistent field arising from the interaction of a single electron with the total electron density of a whole system of electrons at a position r'. In other words, it describes the mean electrostatic interaction felt by an electron due to other electrons in the system where part of it should include the Coulomb interaction between the electron and itself but it remains unphysical. The last potential is the exchange-correlation potential $V_{XC}(\vec{r})$ which accounts for all the remaining electronic energy that is not included in the part of non-interacting terms. The exchange-correlation potential is described as a functional derivative of the electron density[47] :

$$V_{XC}(\vec{r}) = \frac{\delta E_{XC}(\vec{r})}{\delta n(\vec{r})} \tag{2.19}$$

The functional derivative δ is not a regular derivative, one can think about it as a derivative of a quantity that is a function as well. This energy due to the exchange-correlation effects is not known or straightforward, in fact, it requires some approximations to be evaluated. From equation 2.19, we can realize that the electron density must be calculated beforehand which indeed comes after initially calculating the single-electron wave functions. Up till now, the situation looks as if it's running in a loop, which is exactly what the whole idea of solving the Kohn-Sham equations requires. The problem is treated using an iterative procedure as follows:

1. Define an initial electron density which is usually calculated from the superposition of atomic orbitals.

2. Solve the Kohn-Sham equations using the trial density, which determines the single-wave functions $\psi_i(\vec{r})$.

3. Calculate the electron density again as a function of the new electron density as $n_{KS}(\vec{r}) = 2\sum_i \psi_i^*(\vec{r})\psi_i(\vec{r})$

4. Repeat the same cycle until the initial and the new electronic density become equal which is considered the ground state of the system.

Exchange-Correlation Functional

The exchange-correlation energy which was discussed in Eq.2.19, is an unknown quantity and requires a lot of approximations to be achieved. E_{XC} is divided into an exchange part E_X and a correlation part E_C. The exchange energy emerges from the exchange of electrons and is associated with the antisymmetrization of the electronic wave function. The correlation part, on the other hand, accounts for the interaction between electrons beyond the mean-field approximation.

Local Density Approximation (LDA)

The only case where this energy can be derived analytically is in the case of a *uniform electron gas* since the local electron density $n(\vec{r})$ is constant at all the spatial points in this case. Making use of this special condition, we can introduce the first approximation made to calculate $E_{XC}[\{\psi(r)\}]$ which is called the Local Density Approximation (LDA)[48, 49]. The general LDA approximation of a system yielding the exchange-correlation energy is calculated as:

$$E_{XC}(\vec{r}) = \int n(\vec{r})\epsilon_{xc}[n(\vec{r})]d^3r \tag{2.20}$$

where ϵ_{xc} is the exchange-correlation density per particle in a uniform electron gas having an electron density $n(\vec{r})$. The potential in this case is written as :

$$V_{XC}^{LDA}(\vec{r}) = V_{XC}^{electron\ gas}[n(\vec{r})] \tag{2.21}$$

Generalized Gradient Approximation (GGA)

An improvement to the LDA approximation is to include the gradient of the electron density of a homogeneous electron gas, since real systems are not really homogeneous and they have a varying electron density. This approach is called the Generalized Gradient Approximation (GGA)[50]. Among the most used XC functionals of this type are the Perdew-Burke-Ernzerhof (PBE) and the Becke exchange and Lee-Yang-Parr correlation (BLYP)[51]. The GGA functionals have shown in some cases to be superior over LDA, especially in predicting total energies and structural properties but it still underestimates the band gap of materials especially those with strong electronic correlation.

The general form of a GGA energy can be expressed as :

$$E_{XC}(\vec{r}) = \int n(\vec{r})\epsilon_{xc}[n(\vec{r}), \nabla(\vec{r})]d^3r \tag{2.22}$$

Other XC functionals

More advanced functionals exist beyond GGAs although they may increase the computational time of a calculation. Examples on these functionals are the meta-GGA, hyper-GGA, PBE0 and other hybrid functionals such as B3LYP which offer more accuracy of energies. Improvements done on GGA functionals include adding higher orders of the density gradient or mixing a certain amount of the nonlocal HF exchange energy.

The hybrid functionals are a GGA-type based functional in addition to a percentage of the accurate exchange energy from the HF method which usually does not take into account the correlation of electrons. It is expected that this type of mixing would bring better results and reduce errors if part of the HF exchange energy was added. Table 2.1 shows the most used XC functionals in DFT.

Classification	Example	Variables
Local	LDA	n(r)
Semi-Local	GGA	n(r), ∇n(r)
Semi-nonlocal	meta-GGA	n(r), ∇n(r),∇^2n(r)
Hybrid	B3LYP	GGA + HF

Table 2.1: XC functionals that are commonly used in DFT calculations

Plane Waves

All the DFT calculations that are included in this thesis are applied to arrangements of atoms that are periodic in space. These atoms can shape a cell, which is repeated periodically and is defined as a *supercell*. A supercell is designated by three lattice vectors $\vec{a_1}$, $\vec{a_2}$, and $\vec{a_3}$. Solving the Schrödinger equation for such a system to calculate the wave functions requires that the system should have a periodic Coulomb potential. In other words, the solution must satisfy a fundamental property known as **Bloch's theorem** which states that the solution must be expressed as a product of a plane wave and another function $u_{ik}(\vec{r})$.

$$\psi_{ik}(\vec{r}) = e^{i\vec{k}.\vec{r}}u_{ik}(\vec{r}), \qquad u_{ik}(\vec{r}+\vec{R}) = u_{ik}(\vec{r}) \tag{2.23}$$

The vector $\vec{R}$ is the translation vector of the crystallographic lattice. The function $u_{ik}(\vec{r})$ is periodic in space with the same periodicity of the supercell which means that $u_{ik}(\vec{r}+n_1\vec{a_1}+n_2\vec{a_2}+n_3\vec{a_3}) = u_{ik}(\vec{r})$ for any integer n_1, n_2 and n_3.

This theorem implies that we can solve the Schrödinger equation for each value of k, but it is equally applicable for quantities derived from the solutions, such as the electron density. Solutions based on this concept are much easier than in the real space, and since they are

calculated in terms of the plane waves $e^{i\vec{k}.\vec{r}}$, they are referred to as 'plane-wave calculations'[52]. The periodicity of $u_{ik}(\vec{r})$ means that they can be expanded in terms of a special set of plane waves such as :

$$u_{ik}(\vec{r}) = \sum_G c_G e^{i\vec{G}.\vec{r}} \tag{2.24}$$

where c_G is the expansion coefficient and the sum is over all the reciprocal lattice vectors defined by $\vec{G}$ such that $G = m_1\vec{b_1} + m_2\vec{b_2} + m_3\vec{b_3}$ with b_1, b_2, and b_3 being the reciprocal lattice vectors. The overall solution for the Schrödinger equation is as follows:

$$\psi_{i,k}(\vec{r}) = \sum_G C_{\vec{k}+\vec{G}} \quad e^{i(\vec{k}+\vec{G})\vec{r}} \tag{2.25}$$

This sum goes over an infinite number of possible values of G which is not very practical, so a simpler interpretation is used in which only the solutions with lower energies would be considered

$$E = \frac{\hbar^2}{2m}|\vec{k} + \vec{G}|^2 \tag{2.26}$$

such that the kinetic energy cut-off is

$$E_{cut} = \frac{\hbar^2}{2m}G_{cut}^2 \tag{2.27}$$

This cutoff energy must be wisely selected when performing a DFT calculation. The largest cutoff energy of the atoms in a supercell can be taken as the overall value.

Pseudopotentials

The burden in including a high energy cutoff parameter that includes plane waves that oscillate on a shorter wavelength is that these describe the electrons that are tightly bound to the core. These electrons are not necessarily important in describing chemical bonds and other physical properties that are governed by the less tightly bound valence electrons. In order to avoid computational costs, the use of pseudopotentials is essential where it replaces the core electrons and the true potential with a smoother one which produces the electronic wave functions with less oscillations[53]. This approach deals explicitly with the chemically active valence electrons while keeping the core electrons "frozen" so it is known as the "frozen core approximation". In frozen core calculations, the pseudopotential is achieved by considering a single atom of one element, but this pseudopotential is also reliable if used in a chemical environment which gives the pseudopotential a transferrable property. DFT codes provide a library of applicable pseudopotentials where each defines its minimum cutoff energy. One of the most used approaches to construct pseudopotentials is the projector augmented-wave (PAW) method which was introduced by Blöchl and later updated for plane-wave calculations by Joubert and Kresse. All the calculations presented in this thesis are applied using the PAW to extend the plane wave basis set through the implemented software VASP.

To obtain the smooth pseudo-wavefunction through solving the Kohn-Sham equations requires constructing a potential that satisfies certain conditions which are[54]:

(i) The modified potential should coincide with the original Kohn-Sham potential (obtained through an all-electron calculation) outside the pseudization region.

(ii) The modification is made in such a way that the solution of the KS equation yields precisely the pseudo-wavefunction inside of the pseudization region.

Let us remember the Kohn-Sham equation which fulfills the property of a real wave function:

$$\left[-\frac{(\hbar\nabla_i)^2}{2m}+V_{eff}^{[\rho]}(\vec{r})\right]\Psi_i^{KS}(\vec{r})=E_i\Psi_i^{KS}(\vec{r}) \tag{2.28}$$

To construct the pseudo wave function, a projection operator $\hat{P}$ should be applied to the KS wave function as follows:

$$\Psi_i^{KS}(\vec{r})=(1-\hat{P})\phi_i(\vec{r}) \tag{2.29}$$

such that

$$\hat{P}=\sum_i|k_j\rangle\langle k_j| \tag{2.30}$$

where $|k_j\rangle$ are the core states. Substituting Eq.2.29 into the KS equation, the following equation will be yielded giving the pseudopotential $V_{ps}(\hat{r})$:

$$V_{ps}(\hat{r})=V_{eff}^{[\rho]}(\vec{r})-\left[-\frac{(\hbar\nabla_i)^2}{2m}+V_{eff}^{[\rho]}(\vec{r})\right]\hat{P}+E_i\hat{P} \tag{2.31}$$

2.3 Wannier functions

We have seen that the electronic ground state has been described so far through the extended Bloch functions, however, another approach using localized orbitals was established by Gregory Wannier in 1937[55] that of the Wannier functions (WF). The localized orbitals are described by a lattice vector $\vec{R}$ and a band-like index n. WF are potent in the study of materials' electronic and dielectric properties and offer valuable information about the nature of the chemical bonding[56]. The Wannier functions are represented as the Fourier transformation of the periodic Bloch states [57], and they are denoted as $W_n(\vec{r}-\vec{R})$ or $|\vec{R}_n\rangle$:

$$|W_n(\vec{r}-\vec{R})\rangle=\frac{V_{cell}}{(2\pi)^3}\int_{BZ}\sum_{m=1}^{N}U_{mn}^{(k)}|\psi_{m,\vec{k}}\rangle e^{-i\vec{k}.\vec{R}}d\vec{k}, \tag{2.32}$$

$U_{mn}^{(k)}$ is a unitary matrix which transforms a system of N bands at each wave vector k, and the Bloch functions are therefore:

$$|\psi_{m,\vec{k}}\rangle=\sum_{\vec{R}}e^{i\vec{k}.\vec{R}}|\vec{R}_n\rangle \tag{2.33}$$

where V_{cell} is the unit cell's volume. WFs are not eigenfunctions of the single-electron Hamiltonian but they form a complete and orthogonal basis set, where two WFs $|\vec{R}_n\rangle$ and $|\vec{R}'_m\rangle$ transform to each other through a translation vector $\vec{R} - \vec{R}'$.

$$\langle \vec{R}_n | \vec{R}'_m \rangle = \delta_{RR'} \delta mn \tag{2.34}$$

The phase indeterminacy $e^{i\phi_n(k)}$ makes the Wannier functions non-unique and the problem becomes even bigger if we consider a system of isolated bands as in the case of valence states in an insulator since each band will undergo a unitary transformation. This issue has caused impracticality to the use of Wannier functions which was later addressed by Nicola Marzari and David Vanderbilt in 1997 [58] in which they developed a method leading to well-defined and centrally localized functions known as the maximally localized Wannier functions (MLWFs) through the Marzari-Vanderbilt scheme (MV). The MV method is also effective in the case where one is interested in the partially filled band in a certain metal close to the Fermi level that is present at a specific energy range but happens to cross other bands. These kinds of bands are expressed as *entangled* bands, and in such a situation, the number of bands in the energy range would be greater than the number of necessary Wannier functions. This obstacle was further resolved by determining the MLWF through a *disentanglement* identified as the Souza-Marzari-Vanderbilt (SMV) strategy. The mappings from Bloch functions to *maximally localized* Wannier functions (MLWFs)[59] are through a family of transformations in a continuous space of unitary matrices. MLWFs are a very efficient tool for the construction of effective Hamiltonians for the study of ballistic transport, systems with strongly correlated electrons, and self-interaction corrections. Wannier90 is a tool used to implement these methods after obtaining an electronic structure calculation and calculating the overlap matrix between the periodic part $|u_{n\vec{k}}\rangle$ of the Bloch states.
Different approaches have been introduced to reduce the arbitrariness in $U^{(k)}_{mn}$ [60]. The most important was to define a "*localization criterion*" in which a functional measures the spread of the Wannier functions:

$$\Omega = \sum_n \left[\langle \vec{0}n | r^2 | \vec{0}n \rangle - \langle \vec{0}n | \vec{r} | \vec{0}n \rangle^2 \right] = \sum_n \left[\langle r^2 \rangle_n - \vec{\bar{r}}^2_n \right] \tag{2.35}$$

The spread runs over n functions $|\vec{0}n\rangle$ and $\vec{\bar{r}}^2_n = \langle r \rangle_n$. To aim for a maximized localization of the Wannier functions, we should find the choice of the matrices $U_{mn}(k)$ which minimizes the spread Ω.

2.4 Anomalous Hall effect

After obtaining a tight-binding model with the Wannier functions used as a basis set, the anomalous Hall conductivity (AHC) can be calculated [61] through the following equation:

$$\sigma_{xy} = -\frac{e^2}{\hbar}\sum_n \int_{BZ} \frac{d\vec{k}}{(2\pi)^3} f_n(\vec{k}) \mathscr{F}_{n,z}(\vec{k}) \tag{2.36}$$

where $f_n(\vec{k})$ is the Fermi-Dirac distribution function and $\mathscr{F}_{n,z}$ is the Berry curvature which is the main component in the theory of the anomalous Hall effect (AHE) and it is defined as:

$$\mathscr{F}_n(\vec{k}) = \vec{\nabla} \times A_n(\vec{k}) \tag{2.37}$$

where $A_n(\vec{k})$ is the Berry connection which is a vector potential calculated from the eigenstates $|u_{n\vec{k}}\rangle$ as:

$$A_n(\vec{k}) = i\langle u_{n,\vec{k}} | \vec{\nabla}_k | u_{n,\vec{k}} \rangle \tag{2.38}$$

The Berry curvature summed over all the occupied bands leads to the “sum over states equation" written as :

$$\mathscr{F}^{tot}_{\alpha\beta} = i\sum_{n,m}(f_n - f_m)\frac{\langle \psi_n | \hbar v_\alpha | \psi_m \rangle \langle \psi_m | \hbar v_\beta | \psi_n \rangle}{(\epsilon_m - \epsilon_n)^2} \tag{2.39}$$

where v_m and v_n are the velocities obtained from the band derivatives. This approach was used in the theoretical part of the calculation of the anomalous Hall conductivity in the paper [62] presented in Chapter 4.

CHAPTER 3

DZYALOSHINSKII-MORIYA INTERACTIONS IN INTERFACIAL MAGNETIC SYSTEMS WITH STRONG SPIN-ORBIT COUPLING

3.1 Overview of the results

The Dzyaloshinskii-Moriya interaction (DMI) is an antisymmetric exchange interaction [16, 63, 64] which pushes two spins to align perpendicular to each other and provokes a chirality of clockwise or anticlockwise rotation. DMI arises in systems where the time-reversal symmetry is broken and there is a strong spin-orbit coupling. DMI proved to be an important ingredient for the formation of numerous topological textures where it is mostly significant in metallic systems with surfaces and interfaces; especially since it can induce chiral magnetic properties such as domain walls, spin spirals, and skyrmions[65]. Skyrmions are very promising in many applications such as racetrack devices, logic devices, and spintronics[2]. First-principles calculations has emerged as a powerful tool to investigate the strength of the DMI and provide an in-depth understanding of its physical origin in different systems. A lot of research works using density functional theory (DFT) calculations have been done on magnetic bilayers based on the combination of heavy metal (HM)/Ferromagnet(FM) thin films where the band hybridization is a primary factor in controlling the strength of the DMI[66, 67]. In such systems, the arrangement of different multilayers, layer thickness, stacking sequence, and growth conditions allows for a widespread tuning of different magnetic parameters such as the DMI.

The motivation for this chapter comes from a joint experimental-theoretical research done previously by my group on Pt/Co/W thin films where the DMI reached higher values than $2mJ/m^2$ [68]. It was shown that sandwiching Cobalt with two transition metals possessing strong spin-orbit coupling can lead to a remarkable enhancement of the DMI.

The system studied in this paper is Re/Co/Pt where we show that although W is a good candidate

for strengthening the DMI in Co/Pt systems, rhenium can surpass it and contribute to a twofold enhancement. The system was also studied experimentally in my research group at IFPAN by S. K. Jena et al. [69] and by the experimental group in Białystok with which I collaborated[70].
The calculations are based on a practical method introduced by [71] using the Vienna ab initio simulation package (VASP) for calculating the DMI in Co/Pt thin films which are determined based on the energy difference between two different chiralities of the spin textures in the Co atoms in the presence of spin-orbit coupling (SOC). The DMI was calculated as a function of increasing the number of layers of cobalt, as well as of Re to demonstrate the dependence of the system on the thickness of the FM material discussed before [72, 73]. We prove that the DMI has an additive and interfacial property supported by the results of the layer-resolved DMI which shows the highest contributions at both interfaces.
The missing key in DFT calculations regarding multilayered systems and the reason behind our overestimated results is the intermixing at the interfaces which affects the DMI since it is highly sensitive to the quality of the interfaces[74, 75]. Considering this problem, we have established an intermixing scheme between Co and Pt atoms on one hand and Co and Re on the other hand. The results show that the Co/Pt interface is easily affected by the disorder and causes a noticeable reduction of the DMI which is quantitatively in excellent agreement with the experimental observations.
It was shown in early studies that the DMI can compete with other exchange interactions and lead to chiral spin-spiral ground states and magnetic skyrmions [76, 77]. This type of spiral magnetism was also recognized in a family of Weyl semimetals (WSMs) RAlSi [78–80]. For example, in the WSM NdAlSi, the chiral spin texture suggests significant DMI interactions as predicted by the Weyl-mediated RKKY coupling. In the next chapter, we study a WSM which belongs to the mentioned family where we study its AHE in different magnetic configurations. All the calculations and the figures in this paper were done and generated by me, including disscusions and writing.

3.2 PAPER I: Huge Dzyaloshinskii-Moriya interactions in Pt/Co/Re thin films

Journal of Applied Physics

RESEARCH ARTICLE | JANUARY 17 2024

Huge Dzyaloshinskii–Moriya interactions in Pt/Co/Re thin films

Amar Fakhredine ; Andrzej Wawro ; Carmine Autieri

J. Appl. Phys. 135, 035303 (2024)
https://doi.org/10.1063/5.0177260

Journal of Applied Physics ARTICLE pubs.aip.org/aip/jap

Huge Dzyaloshinskii–Moriya interactions in Pt/Co/Re thin films

Cite as: J. Appl. Phys. **135**, 035303 (2024); doi: 10.1063/5.0177260
Submitted: 20 September 2023 · Accepted: 23 December 2023 ·
Published Online: 17 January 2024

View Online Export Citation CrossMark

Amar Fakhredine,[1,2,a)] Andrzej Wawro,[1,b)] and Carmine Autieri[2]

AFFILIATIONS

[1]Institute of Physics, Polish Academy of Sciences, Aleja Lotników 32/46, PL-02668 Warsaw, Poland
[2]International Research Centre Magtop, Institute of Physics, Polish Academy of Sciences, Aleja Lotników 32/46, PL-02668 Warsaw, Poland

[a)]**Author to whom correspondence should be addressed:** amarf@ifpan.edu.pl
[b)]wawro@ifpan.edu.pl

ABSTRACT

We investigate the magnetization and the Dzyaloshinskii–Moriya interactions (DMI) in Pt/Co/Re thin films in the case of perfect interfaces and upon the introduction of intermixing on both Co interfaces. Calculations were implemented on a series of systems with a countable number of cobalt atomic layers. Remarkably, Re can introduce a DMI at the interface with cobalt and also increase the DMI at the Pt/Co interface. We demonstrate that the chiral magnetic multilayer Pt/Co/Re with a chiral spin structure can achieve a substantial DMI value, which is almost double that attained in the prototype system Pt/Co/W. We also study the DMI as a function of the Re thickness, finding the optimal thickness to maximize the DMI. When we include a disorder that cancels a contribution from all first-neighbor Co atoms in the intermixed region, we find out that intermixing at the two interfaces affects the strength of the DMI solely when introduced at the Pt/Co interface, where the DMI loses almost half of its value. On the contrary, the mixing at the Co/Re interface has very little or no effect where the calculated values were not significantly decreased as compared to the case with perfect interfaces.

I. INTRODUCTION

A trilayer structure that exhibits a lack of inversion symmetry, with a ferromagnetic layer situated between two substantial heavy metals, potentially gives rise to intricate chiral magnetic configurations. At the core of this setup is the Dzyaloshinskii–Moriya interaction (DMI), characterized by an exchange energy term with an antisymmetric nature. This interaction takes on the role of directing the alignment of interacting spins in a non-collinear manner within systems lacking inversion symmetry and featuring robust spin–orbit coupling (SOC).[1–3] The DMI promotes magnetic configurations with consistent rotational orientation, such as Néel-type domain walls and skyrmions.[4] An example of this occurs at interfaces between cobalt and heavy materials like iridium or platinum, both of which possess significant SOC.[5,6] The skyrmions are topologically protected against continuous deformation toward spin structures with different topological invariants.[7,8] Skyrmions hold promise for a wide range of technological applications, including data storage, spintronics, logic devices, neuromorphic computing, quantum computing, magnetic sensors, and energy-efficient electronics.[9] Ongoing research in these areas could yield significant and transformative impacts.

Several research papers have concentrated on investigating Pt/Co bilayers,[10] specifically its DMI contribution, however, enhancing this chiral interaction could be achieved by sandwiching cobalt with another 5d material creating a chiral spin magnetic multilayer.[11,12] One of the examples is the magnetic stack Pt/Co/W, which was studied both experimentally and theoretically showing a DMI value that reaches higher than 2 mJ/m^2.[13] On the other side, stacks like Al/Co/Pt and Ir/Co/Pt[14] were reported in other works,[15] showing a weaker contribution that the bilayers Al/Co and Ir/Co can provide to the overall DMI. Our work shows that the use of another 5d material, that is, rhenium can induce a higher DMI value and be even more prospective. For instance, it was reported that capping Co with a Re monolayer could give a clockwise (CW) contribution of around 1.5 meV nm, which is of the opposite sign to the contribution yielded by Pt/Co, which allows the system Pt/Co/Re to be a candidate for a huge DMI.[16,17] Recent experimental

works on Pt/Co/Re have also confirmed this relatively large value and additive behavior of the DMI.[18–20] In spin–orbit bulk systems, rhenium largely increases the magnetic damping in FeCo alloy, demonstrating its effectiveness in inducing spin–orbit effects in the Co-based system.[21]

Many theoretical studies have validated the overall DMI of magnetic trilayers, which is usually overestimated with respect to experimental findings. The discrepancy observed can be attributed to the theoretical distinct emphasis on trilayers with sharp atomic layers (ALs), while multilayers produced experimentally are anticipated to exhibit separate vertical textures due to intermixing effects at the interfaces.[22] As a result, we also conducted calculations including interface disorder to seek an explanation for this type of disparity.

In this paper, we study the DMI in Pt/Co/Re thin films where we show the variation of this effect as a function of cobalt multilayers up to a scale of 10 AL. The values of DMI achieved for our system exceed the prototype system for the chiral ferromagnetic multilayers Pt/Co/W.[23] We believe that the usage of Re affects the total DMI of the whole system and enhances the Pt/Co contribution even though it is not a direct neighbor to Pt, an effect which was also seen in the case of Rh and Pd.[24] This hypothesis was also mentioned in a paper by Jia *et al.*,[22] stressing that using a capping element Z in Pt/Co/Z systems modifies the DMI at the Pt/Co interface although it is believed that only a change in the quality of the interface can alter this contribution. The origin of the system's huge DMI was found to be purely interfacial while the contributions to the DMI from the inner layers are oscillating and, thus, become non-effective. In addition, we study the effect of disorder at the two interfaces where we launched two different schemes of intermixed interfaces to indicate their effect on the magnetization and the DMI. We unveil a distinct robustness against the intermixing at the Pt/Co interface demonstrated by around 40% reduction from the significantly high value achieved in the ideal case.

II. COMPUTATIONAL FRAMEWORK

The technique of constraining the magnetic moments in a supercell was used to calculate the DMI of Pt/Co/Re multilayers through the density functional theory framework.[25] The Vienna *ab initio* simulation package (VASP) was used in all calculations using electron-core interactions described by the projector augmented wave (PAW) method,[26] and the exchange-correlation energy is calculated within the generalized gradient approximation of the Perdew–Burke–Ernzerhof (PBE) form.[27] We have employed for the Pt the PAW with six valence electrons in the electronic configuration $6s^2 5d^8$, for the Co we have nine valence electrons with $4s^2 3d^7$ while for the Re we have seven electrons with $6s^2 5d^5$ electronic configuration. The cutoff energies for the plane-wave basis set that were used to expand the Kohn–Sham orbitals were chosen to be 280 eV. The Monkhorst–Pack scheme was used for the Γ-centered $4 \times 12 \times 1$ k-point sampling to follow the recipe done by Yang *et al.*[28]

In order to extract the DMI vector, the calculations were carried out in three steps. First, structural relaxations were performed under a ferromagnetic state without SOC to determine the most stable interfacial geometries until the Hellman–Feynman forces converged to less than 0.015 eV/Å. Next, the Kohn–Sham equations were solved without SOC to determine the charge distribution of the system's ground state. Finally, SOC was included and the self-consistent total energy of the system was determined as a function of the orientation of the magnetic moments which were controlled by using the constrained method implemented in VASP. The DMI was calculated using the method described by Yang *et al.*,[28] which necessitates forcing the magnetic moments to rotate in a specific manner. In Fig. 1, we report the clockwise (CW) and anticlockwise (ACW) magnetic configuration in the real space. The DMI orientation depends on which magnetic configuration has the lowest energy.

A set of structural models of the Pt/Co/Re of the 4×1 unit cell stack were set up in a close-packed configuration. A primitive P1 space group unit cell was used to build the Pt/Co/Re multilayer stack supercells. For modeling the geometries of the interfaces, the experimental in-plane lattice constant of the Pt (111) surface, which is 3.92 Å was used and hcp layer growth was assumed for Co and Re layers, while for Pt, fcc growth was considered. We varied the number of cobalt atomic layers ranging from 1 to 10 Als respective to each of our structures with a constant number of 5 AL for platinum and 5 AL for rhenium. The thin-film calculations were performed using slab geometry with a vacuum layer of 15 Å along the out-of-plane direction. This computational setup based on PBE has been used for the determination of magnetic properties in ferromagnetic multilayers.[29,30] The DMI was calculated using the method described by Yang *et al.*[28] The DMI strength [d (meV)] parameter was calculated from the energy differences between clockwise and anti-clockwise energy configurations of the magnetic spirals in the cobalt layers for the perfect interface as shown in Fig. 1. The DMI strength is further used to calculate the micromagnetic DMI which we use in our results. The micromagnetic DMI is

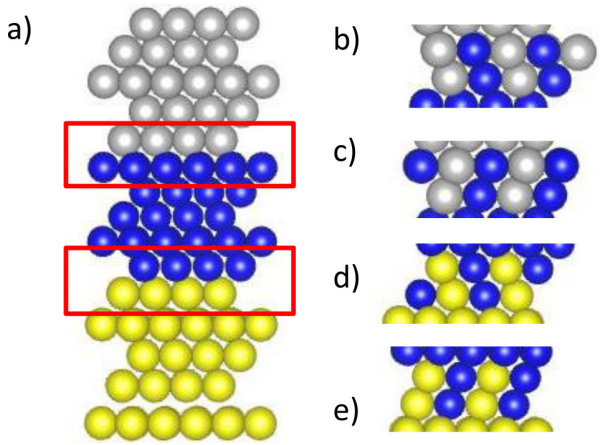

FIG. 1. (a) Layered structure of the Pt/Co/Re system with a perfect interface. The yellow, blue, and gray balls represent the Pt, Co, and Re atoms, respectively. Crystal structures resembling the (b) Z-mixing and (c) C-mixing at the Pt/Co interface. Crystal structures resembling the (d) Z-mixing and (e) C-mixing at the Co/Re interface. The red rectangles are to indicate the area of two layers where the intermixing was introduced. After the intermixing, the number of layers composed entirely of cobalt atoms decreases by one with respect to the perfect interface.

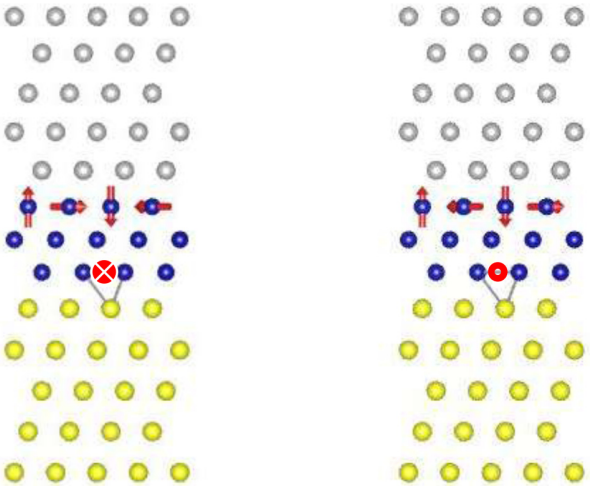

FIG. 2. Schematic structures for clockwise (left panel) and anticlockwise (right panel) directions of the chiral magnetic moments in $Pt_5/Co_3/Re_5$. The red arrows represent the Co spins in the two different clockwise and anticlockwise configurations. The yellow, blue, and gray balls represent the Pt, Co, and Re atoms, respectively. The direction of the DMI vectors is represented as a cross or point for incoming or outgoing direction.

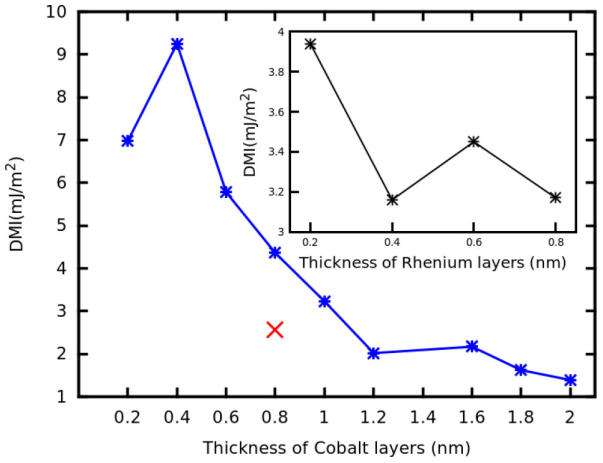

FIG. 3. Micromagnetic DMI results as a function of cobalt thickness (blue solid line) for $Pt_5/Co(nm)/Re_5$ where the subscript indicates the number of AL for a given element. Each cobalt AL has a thickness of 0.2 nm. For comparison, we add also the record-high value of Pt/Co/W from the literature[13,23] marked with a red cross. The inset of the figure shows the variation of the DMI as a function of rhenium layers for the thin-film $Pt_5/Co_5/Re(nm)$. The lines are a guide for the eyes.

calculated in units of mJ/m^2 and is a value that is inversely proportional to the number of ferromagnetic layers N_F and the fcc lattice constant.[28] This method has been used for DMI calculations in bulk frustrated systems and insulating chiral-lattice magnets[31] and later was adapted here in the case of metallic interfaces.[28,32] For the intermixed calculations, we replaced two layers at the interface composed of 50% Co and 50% Pt or Re such that the number of total atoms is conserved relative to the case of perfect interfaces. We denote the types of mixing used for our calculations as C- and Z-type with respect to different atomic neighborhoods as shown in Figs. 2(b)–2(e). The C- and Z-types have the same first-neighbor crystal structure but different second neighbors, therefore, the results of the two calculations are expected to be similar. We report both results to demonstrate the numerical accuracy of our DMI estimation. The Co and Pt(Re) are totally intermixed and there are no Co–Co first-neighbor in the intermixing region.

III. RESULTS

We divide our results into two subsections, where we describe the system with perfect interfaces in the first part, while in the second part, we consider the system by adding mixed interfaces with variable selected thicknesses of cobalt ALs.

A. Perfect interface

We calculate the micromagnetic DMI for the Pt/Co/Re thin film with perfect interfaces represented in Fig. 2(a). The calculations of the total magnetic DMI contribution followed a declining trend as we increased the thickness of the cobalt layer as shown in Fig. 3. The maximum value reached is 9.25 mJ/m^2 for 2 AL of cobalt while it drops to a minimal value of 1.39 mJ/m^2 at a thickness of 10 ALs. The curve roughly follows the trend of $\frac{1}{N_F}$ for the micromagnetic DMI[28] with some oscillations due to the metallic nature of the systems. While at low N_F these oscillations are not visible, these oscillations can produce plateaus at large N_F as the one observed between 1.2 and 1.6 Å in Fig. 3. The case of one cobalt layer is a peculiar point since it shares the same interface with rhenium on one side and platinum on the other side, which makes the DMI non-additive in this case. The DMI energy value for 1 AL of cobalt produced a much smaller DMI compared to the case of 2 AL, and, consequently, a smaller value of the micromagnetic DMI considering it depends on the thickness of the ferromagnetic layer. In the inset, we report the evolution of the DMI as a function of the Re thickness for the $Pt_5/Co_5/Re(nm)$ thin films. In contrast to cobalt, changes in the arrangement of rhenium layers have a relatively smaller impact on the strength of the DMI. The DMI shows a gradual variation from 3 to 4 mJ/m^2 as the rhenium thickness increases from 1 to 4 ALs, which is close to the value calculated for the system $Pt_5/Co_5/Re_5$ that is 3.23 mJ/m^2.

The layer-resolved DMI strength on each cobalt layer was also calculated by introducing chiral magnetic moments for each layer separately. We calculate the layer-resolved DMI strength for $Pt_5/Co_n/Re_5$ with n = 3, 4, 5, and 6 as can be seen from Figs. 4(a)–4(d), respectively. For all cases, the calculated d^k shows that two essential contributions are located at the Co interfaces with a positive sign. The other inner layers give a, respectively, smaller and oscillating d^k value, which does not participate systematically to the total DMI. The oscillating nature of the DMI rises from the metallicity.[33] The summation over d^k should be close to the total value of the DMI, where the minor difference comes from the fact that a small DMI

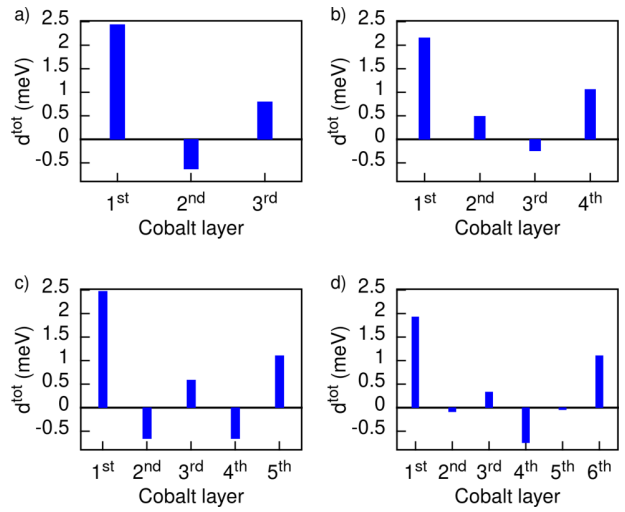

FIG. 4. Layer-resolved DMI strength of the system with (a) for $Pt_5/Co_3/Re_5$, (b) $Pt_5/Co_4/Re_5$, (c) $Pt_5/Co_5/Re_5$, and (d) $Pt_5/Co_6/Re_5$. The first layer on the left side denotes the contribution coming from the Pt/Co interface while that at the right is due to Co/Re.

contribution comes from the Pt atoms. The value of the DMI at the Pt side is around 2.0–2.5 meV, in agreement with the data shown in Ref. 34. It is relatively high in comparison to the case of Pt/Co/W[13] system, yielding half of the strength to around 1 meV. On the other hand, on the Re side, a value of around 1 meV was always achieved. The DMI at Pt/Co and Co/Re interfaces showing the same sign of the chiralities are in agreement with experiments where the values

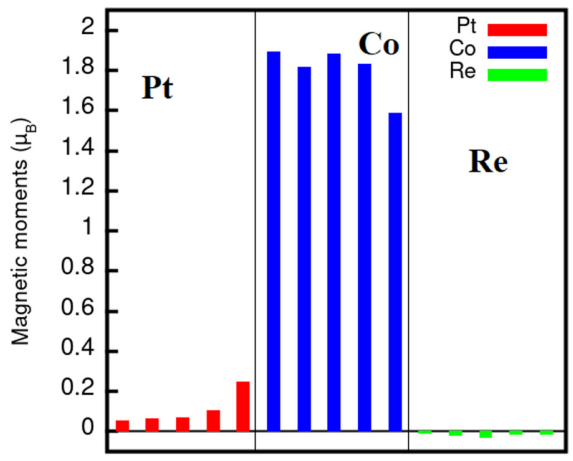

FIG. 5. Magnetization profile of the system $Pt_5/Co_5/Re_5$ with perfect interfaces. The system consists of five layers of each element in the stack. The interfacial magnetization effect weakly depends on the thicknesses of the Re, Co, and Pt.

TABLE I. Total energies (eV) of the intermixed systems for both types compared to the perfect system.

Type of interface	C-mixing	Z-mixing
Mixed Pt/Co interface	−499.194	−499.435
Mixed Co/Re interface	−498.401	−498.053
Perfect interface	−498.622	−498.622

add up in the Pt/Co/Re systems producing a huge total DMI. It is also worth mentioning that the micromagnetic DMI depends on the magnetic layers' thickness because DMI appears mainly at the interface as an effect of the hybridization between magnetic moments in the 3d cobalt layers and the strong SOC in 5d states of Pt and Re. If one has to compare the trilayer systems Pt/Co/Re with Pt/Co/W,[13] it is noticeable that the Pt/Co DMI contribution at the latter system is less in value. This behavior is similar to the case discussed in another work,[24] where different stacks like Pt/Co/Rh and Pt/Co/Pd produced two distinct DMI values at the Pt/Co interface. Different transition metals with different SOC strengths can affect the overall DMI significantly.

The magnetization profile of the intrinsic spin of Co atoms and the induced magnetic moments at the 3d/5d interfaces were studied and displayed at equilibrium interlayer distances after performing the full relaxation scheme. This calculation was done for the ground state without SOC. The trend that is shown in Fig. 5 was studied after that by varying the number of cobalt ALs. The figures show a positively induced spin polarization on the platinum atoms at the Pt/Co[35,36] interface with a value of about $0.25\,\mu_B$. On the other hand, there is almost no visible polarization at the rhenium substrate at the Co/Re interface. The magnetic moments of cobalt facing Re dropped by more than 10% of its original value,

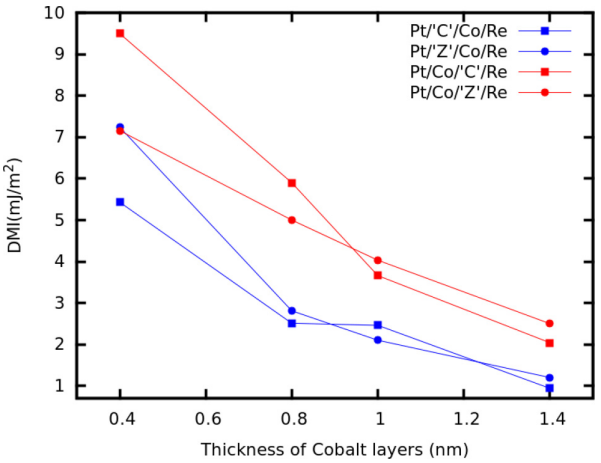

FIG. 6. Micromagnetic DMI results as a function of cobalt thickness for the two types of intermixing at both interfaces. The effective DMI here was calculated by dividing the total DMI by only the complete Co layers disregarding the mixed ones.

while those of rhenium show very low polarizability, also reported in Ref. 37. This could be due to the weak hybridization of the 3d-states of cobalt with the low-lying states in rhenium, which is similar to the case for Co/Au[16] or Fe/Re.[29] By adding more cobalt ALs, the same behavior was seen even on relatively high thicknesses, which confirms that rhenium is a weak polarizable transition metal.

B. Intermixing at the interfaces

To further investigate the influence of interfacial roughness on the DMI of the Pt/Co/Re structures, we generated a set of thin films with varying interfacial crystallinity by modifying the atomic arrangement of interfacial atoms. Two different types of mixed interface layers are presented in Figs. 2(b)–2(e) denoted as C-mixing and Z-mixing, which shows a different structural assortment of the atoms. Both the Pt/Co interface and the Co/Re interface were subject to this type of mixing, in order to study the influence of the different transition metals. From the energetics shown in Table I, the ground state of the Co/Re interface is the perfect interface while the ground state at the Pt/Co interface is the structure with inter-diffusion. This explains the strong effects of intermixing at the Pt/Co interface found experimentally.[38,39]

The method of the DMI calculations and the structural setup followed the same technique as in the case of perfect interfaces, where the spin spirals were included only on the cobalt atoms and

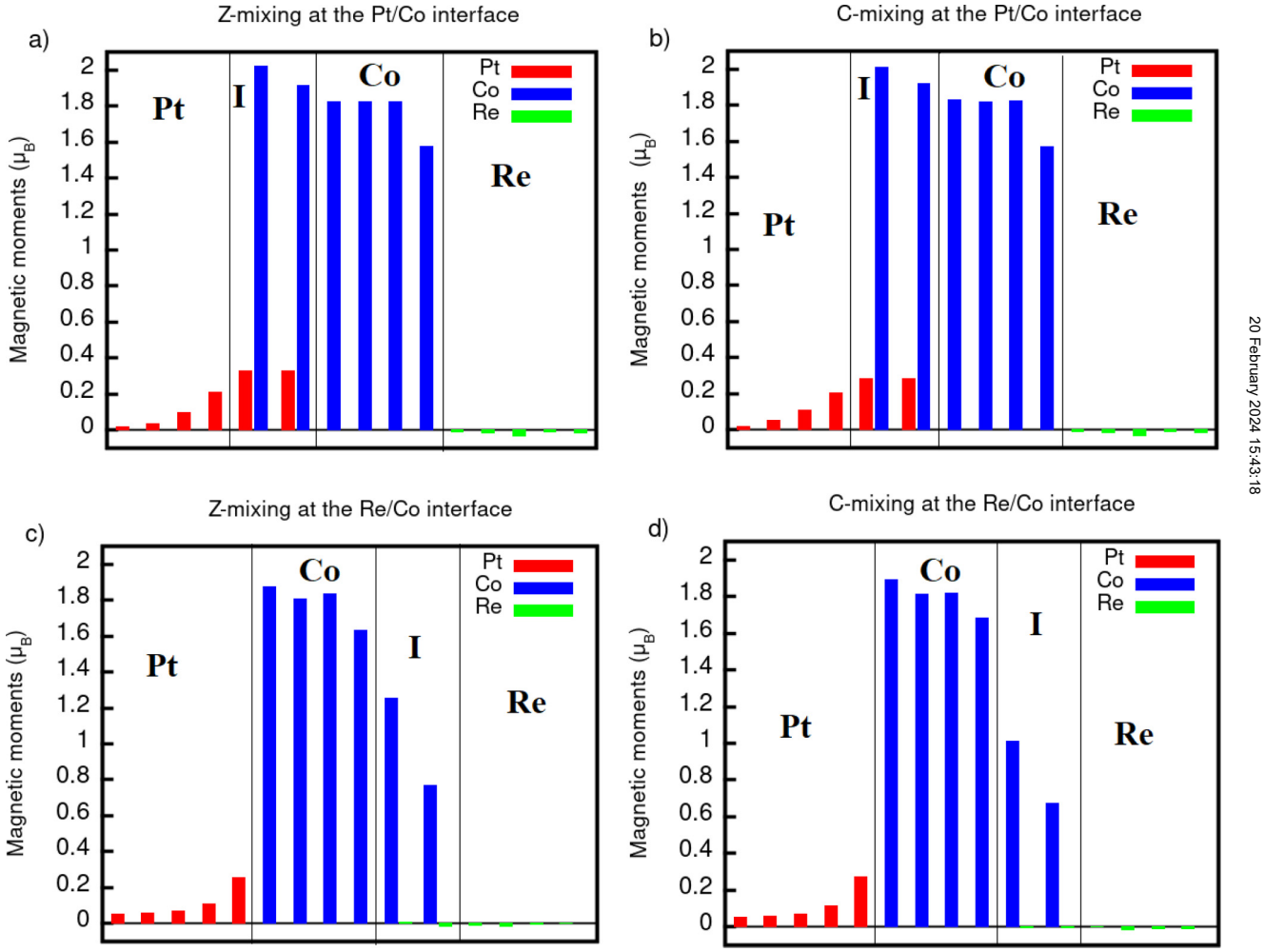

FIG. 7. Magnetization profile of the $Pt_5/Co_5/Re_5$ system with mixed interfaces: (a) Z- and (b) C-type mixing at the Pt/Co interface, (c) Z- and (d) C-type mixing at the Co/Re interface. We label the regions divided by vertical lines as Pt, Co, Re, and I, where I indicates the intermixing region and Pt, Co, and Re indicate the regions with ALs of a single element. After the mixing, these systems are such that the number of complete cobalt layers is four in addition to two mixed layers at the interface with half cobalt atoms.

on the other complete cobalt layers. We begin our analysis by examining the situation in which the mixing is specifically implemented at the Pt/Co interface. By applying interfacial Co–Pt intermixing in either scenario, we found a decrease in the DMI, which aligns with experimental findings suggesting that enhanced crystallinity leads to a larger DMI. With these kinds of intermixing, we do not have Co atoms first-neighbor in the intermixing region. It is expected to produce a sensitive reduction of the total DMI since the first-neighbor DMI is supposed to give the largest contribution to the total DMI.

The results of the micromagnetic DMI for the intermixing case are shown in Fig. 6. The effective DMI here was calculated by dividing the total DMI by only the complete Co layers disregarding the mixed ones. Also in the case of intermixing, the curve of the micromagnetic DMI roughly follows the trend of $\frac{1}{N_F}$ as for the perfect interface case. To initiate the analysis, the first studied system, which includes one cobalt layer (in the ideal case) and two cobalt layers (in the disordered case), displays a minor shift in the DMI value. Nevertheless, it is crucial to recognize that these cases are peculiar and cannot be classified as representative of the general case. Moving to higher thicknesses, the value obtained for the system with two mixed layers of Co and Pt along with three complete layers is 2.51 mJ/m^2 for the case of C-mixing and 2.81 mJ/m^2 in the case of Z-mixing. Moreover, the value for the system, where we introduced two mixed layers of Co and Pt along with four complete layers, is 2.46 mJ/m^2 for the case of C-mixing and 2.10 mJ/m^2 for the case of Z-mixing. Finally, the case for two mixed layers of Co and Pt along with 6 complete layers of Co yielded 0.94 mJ/m^2 for the case of C-mixing and 1.20 mJ/m^2 for the case of Z-mixing. Therefore, the DMI was reduced by the disorder in all cases. Since the DMI between the second neighbors in the plane and between the first-neighbors out-of-plane is neglected, the cobalt atoms in the mixed layers do not contribute to the total DMI. Consequently, the DMI will depend on the last complete layer of Co atoms. In the case of the mixed interface, the Co atoms confront only 50% of the Pt atoms; therefore, the interfacial DMI of the interfacial Co-layer is approximately reduced by 50%. However, we stress the role of the platinum atoms present in the disordered layers where fewer atoms participate in lowering the SOC of the system concerning the ideal case. Therefore, giving an overall lower DMI value than that in the case of perfect interfaces. This significant reduction at the Pt/Co interface was reported in another work,[40] where the DMI is proved robust against mixing and the system experiences a decrease with increasing the interfacial mixing of Pt and Co atoms, which confirms our results. The experimental values of the micromagnetic DMI are expected to be between the values of the perfect interfaces and the intermixed ones. Coming to the case related to the Co/Re interface, the values of the DMI after intermixing were slightly smaller than the case of perfect interfaces as can be shown in Fig. 6. Since the Co/Re intermixing weakly affects the DMI, the DMI values for the Co/Re intermixing are larger than that for the Pt/Co intermixing.

After studying the DMI, we discuss the variation of the magnetic moments in the case of intermixing, especially at the interface where the coordination of cobalt atoms completely changes. We present the bar graphs in Fig. 7 to illustrate the effect. The figures present the system with two mixed interfaces in C and Z-type mixing, along with three complete cobalt layers and five layers for each of Pt and Re. Mixing at the Pt/Co interface increases the moments at Co atoms in both types of intermixing as shown in Figs. 7(a) and 7(b) in the alloyed zone and also enhances the moment at the next Pt layer.[38,41] The observed increase in the magnetism of cobalt atoms aligns with the narrowing of the d-bands, leading to an enhancement of magnetism caused by the progressive reduction of like-nearest neighbors.[42] When examining the Co/Re interface Figs. 7(c) and 7(d), the magnetic moment of the Co interfacial layer experiences reduction, which was also seen in the case of the ideal interface. Meanwhile, the magnetic moments generated within the Re layers display an inversion in its sign, being indicative of a possible antiferromagnetic coupling. However, its magnitude remains negligible, consistent with previously documented values.[43] Despite the changes observed in the magnetic moments of Co and Pt due to disorder, Re atoms exhibit no noticeable increase in polarizability, maintaining their state as in the ideal case.

IV. CONCLUSIONS

Using first-principle calculations, we have proved that the chiral metallic multilayer Pt/Co/Re possesses a huge DMI of up to micromagnetic DMI of 9.25 mJ/m^2 (or DMI strength of 4.19 meV). Re and Pt produce opposite chirality; therefore, the DMIs at the Co/Re and Pt/Co interfaces sum up to produce this huge effect. The Re enhances the DMI at the Pt/Co interfaces. We have also found out that the induced magnetization is large and positive for the Pt up to 0.244 for the atoms interfaced with Co, while it is very small and negative for the Re atoms. We proved that Pt/Co/Re has better properties than the prototype system Pt/Co/W. Upon study of the effect of intermixing on both interfaces, the intermixing on the Pt/Co interface introduces a suppression of the interfacial DMI, while that on Co/Re shows very little or no effect on the system. Since the biggest contribution to the DMI comes from the Pt side of the stack, the intermixing at the Pt/Co interface produces a larger suppression of the total DMI. Once the grown conditions are optimized to minimize the Pt/Co intermixing, the trilayer Pt/Co/Re could be used for skyrmions transport devices paving the way to new technological applications. The realization of such a device should focus on the reduction of the Pt/Co intermixing to realize this huge DMI.

ACKNOWLEDGMENTS

The authors were supported by the Polish National Science Centre under Project No. 2020/37/B/ST5/02299. The work was supported by the Foundation for Polish Science through the International Research Agendas program co-financed by the European Union within the Smart Growth Operational Programme (Grant No. MAB/2017/1). We acknowledge the access to the computing facilities of the Interdisciplinary Center of Modeling at the University of Warsaw (Grant Nos. g91-1418, g91-1419, and g91-1426) for the availability of high-performance computing resources and support. We acknowledge the CINECA award under the ISCRA initiative IsC99 “SILENTS,” IsC105 “SILENTSG,” IsB26 “SHINY,” and IsB27 “SLAM” grants for the availability of high-performance computing resources and support. We acknowledge

the access to the computing facilities of the Poznan Supercomputing and Networking Center (Grant No. 609).

AUTHOR DECLARATIONS

Conflict of Interest

The authors have no conflicts to disclose.

Author Contributions

Amar Fakhredine: Conceptualization (lead); Data curation (lead); Writing – original draft (lead); Writing – review & editing (equal). **Andrzej Wawro:** Supervision (equal); Writing – original draft (equal); Writing – review & editing (equal). **Carmine Autieri:** Conceptualization (equal); Data curation (equal); Supervision (equal); Writing – original draft (equal); Writing – review & editing (equal).

DATA AVAILABILITY

The data that support the findings of this study are available from the corresponding author upon reasonable request.

REFERENCES

[1]I. Dzyaloshinsky, J. Phys. Chem. Solids **4**, 241 (1958).
[2]T. Moriya, Phys. Rev. **120**, 91 (1960).
[3]T. Moriya, Phys. Rev. Lett. **4**, 228 (1960).
[4]M. Heide, G. Bihlmayer, and S. Blügel, Phys. Rev. B **78**, 140403 (2008).
[5]A. Fert, in *Materials Science Forum*, Vol. 59 (Trans Tech Publications, 1990), pp. 439–480.
[6]H. Moriya, A. Musha, and K. Ando, Appl. Phys. Express **14**, 063001 (2021).
[7]J. Barker and O. A. Tretiakov, Phys. Rev. Lett. **116**, 147203 (2016).
[8]Z.-L. Deng, T. Shi, A. Krasnok, X. Li, and A. Alù, Nat. Commun. **13**, 8 (2022).
[9]S. Luo and L. You, APL Mater. **9**, 050901 (2021).
[10]K. Yamamoto, S. E. Moussaoui, Y. Hirata, S. Yamamoto, Y. Kubota, S. Owada, M. Yabashi, T. Seki, K. Takanashi, I. Matsuda, and H. Wadati, Appl. Phys. Lett. **116**, 172406 (2020).
[11]W. Jiang, G. Chen, K. Liu, J. Zang, S. G. te Velthuis, and A. Hoffmann, Phys. Rep. **704**, 1 (2017).
[12]A. Hrabec, Z. Luo, L. J. Heyderman, and P. Gambardella, Appl. Phys. Lett. **117**, 130503 (2020).
[13]S. K. Jena, R. Islam, E. Milińska, M. M. Jakubowski, R. Minikayev, S. Lewińska, A. Lynnyk, A. Pietruczik, P. Aleszkiewicz, C. Autieri, and A. Wawro, Nanoscale **13**, 7685 (2021).
[14]M. Perini, S. Meyer, B. Dupé, S. Von Malottki, A. Kubetzka, K. Von Bergmann, R. Wiesendanger, and S. Heinze, Phys. Rev. B **97**, 184425 (2018).
[15]H. Yang, O. Boulle, V. Cros, A. Fert, and M. Chshiev, Sci. Rep. **8**, 12356 (2018).
[16]A. Belabbes, G. Bihlmayer, F. Bechstedt, S. Blügel, and A. Manchon, Phys. Rev. Lett. **117**, 247202 (2016).
[17]P. Jadaun, L. F. Register, and S. K. Banerjee, npj Comput. Mater. **6**, 88 (2020).
[18]A. Nomura, T. Gao, S. Haku, and K. Ando, AIP Adv. **12**, 015215 (2022).
[19]A. K. Dhiman, A. Fakhredine, R. Gieniusz, Z. Kurant, I. Sveklo, P. Dłewski, W. Dobrogowski, A. Pietruczik, S. K. Jena, C. Autieri, A. Wawro, and A. Maziewski, "Strong changes of magnetic properties of Pt/Co/Pt trilayers driven by interfacial Re insertion" (to be published).
[20]S. Jena, J. Kisielewski, R. Gieniusz, U. Guzowska, A. Fakhredine, C. Autieri, A. Lynnyk, A. Pietruczik, A. Maziewski, and A. Wawro, in *2023 IEEE International Magnetic Conference—Short Papers (INTERMAG Short Papers)* (IEEE, 2023), pp. 1–2.
[21]S. Akansel, A. Kumar, V. A. Venugopal, R. Esteban-Puyuelo, R. Banerjee, C. Autieri, R. Brucas, N. Behera, M. A. Sortica, D. Primetzhofer, S. Basu, M. A. Gubbins, B. Sanyal, and P. Svedlindh, Phys. Rev. B **99**, 174408 (2019).
[22]H. Jia, B. Zimmermann, G. Michalicek, G. Bihlmayer, and S. Blügel, Phys. Rev. Mater. **4**, 024405 (2020).
[23]M. Kuepferling, A. Casiraghi, G. Soares, G. Durin, F. Garcia-Sanchez, L. Chen, C. H. Back, C. H. Marrows, S. Tacchi, and G. Carlotti, Rev. Mod. Phys. **95**, 015003 (2023).
[24]H. Jia, B. Zimmermann, and S. Blügel, Phys. Rev. B **98**, 144427 (2018).
[25]M. G. Morshed, K. H. Khoo, Y. Quessab, J.-W. Xu, R. Laskowski, P. V. Balachandran, A. D. Kent, and A. W. Ghosh, Phys. Rev. B **103**, 174414 (2021).
[26]G. Kresse and J. Furthmüller, Phys. Rev. B **54**, 11169 (1996).
[27]J. P. Perdew, K. Burke, and M. Ernzerhof, Phys. Rev. Lett. **77**, 3865 (1996).
[28]H. Yang, A. Thiaville, S. Rohart, A. Fert, and M. Chshiev, Phys. Rev. Lett. **115**, 267210 (2015).
[29]C. Autieri, P. A. Kumar, D. Walecki, S. Webers, M. A. Gubbins, H. Wende, and B. Sanyal, Sci. Rep. **6**, 29307 (2016).
[30]C. Autieri and B. Sanyal, J. Phys.: Condens. Matter **29**, 465802 (2017).
[31]H. Xiang, E. Kan, S.-H. Wei, M.-H. Whangbo, and X. Gong, Phys. Rev. B **84**, 224429 (2011).
[32]J.-H. Yang, Z.-L. Li, X. Lu, M.-H. Whangbo, S.-H. Wei, X. Gong, and H. Xiang, Phys. Rev. Lett. **109**, 107203 (2012).
[33]A. Hajr, A. Hariri, G. Manchon, S. Ghosh, and A. Manchon, Phys. Rev. B **102**, 224427 (2020).
[34]F. Mahfouzi and N. Kioussis, Phys. Rev. B **103**, 094410 (2021).
[35]S. Grytsyuk and U. Schwingenschlögl, Phys. Rev. B **88**, 165414 (2013).
[36]A.-M. Pradipto, K. Yakushiji, W. S. Ham, S. Kim, Y. Shiota, T. Moriyama, K.-W. Kim, H.-W. Lee, K. Nakamura, K.-J. Lee, and T. Ono, Phys. Rev. B **99**, 180410 (2019).
[37]S. Grytsyuk, A. Belabbes, P. M. Haney, H.-W. Lee, K.-J. Lee, M. D. Stiles, U. Schwingenschlögl, and A. Manchon, Phys. Rev. B **93**, 174421 (2016).
[38]A. Verna, P. Alippi, F. Offi, G. Barucca, G. Varvaro, E. Agostinelli, M. Albrecht, B. Rutkowski, A. Ruocco, D. Paoloni, M. Valvidares, and S. Laureti, ACS Appl. Mater. Interfaces **14**, 12766 (2022).
[39]S. Bandiera, R. C. Sousa, B. Rodmacq, and B. Dieny, Appl. Phys. Lett. **100**, 142410 (2012).
[40]R. Chen, Q. Cui, L. Liao, Y. Zhu, R. Zhang, H. Bai, Y. Zhou, G. Xing, F. Pan, H. Yang, and C. Song, Nat. Commun. **12**, 3113 (2021).
[41]G. B. Flores and K. Belashchenko, Phys. Rev. B **105**, 054405 (2022).
[42]B. Zimmermann, W. Legrand, D. Maccariello, N. Reyren, V. Cros, S. Blügel, and A. Fert, Appl. Phys. Lett. **113**, 232403 (2018).
[43]E. Simon, L. Rózsa, K. Palotás, and L. Szunyogh, Phys. Rev. B **97**, 134405 (2018).

CHAPTER 4

EXPERIMENTAL AND THEORETICAL OBSERVATION OF THE DZYALOSHINSKII-MORIYA INTERACTION IN PT/CO/RE THIN FILMS

4.1 Overview of the results

In this chapter, we present the common work done between authors from the Institute of Physics (IFPAN) and the University of Białystok (UwB). The work combines experimental and theoretical studies using density functional theory (DFT) calculations on the investigation of the magnetic properties of Pt/Co/Re thin films. The results recorded in Chapter 3 which include the DMI values achieved from DFT calculations before and after the inclusion of disorder at both interfaces of the system were used as a confirmation for the high value of the Dzyaloshinskii-Moriya interaction (DMI) found in the studied Pt/Co/Re system.

Adding the effect of intermixing has proved the importance of the interface quality on the value of this magnetic parameter. This was revealed by a better agreement with the experimental results where the DMI revealed lower values ranging between 1 and 2 mJ/m^2, closer to the values achieved experimentally. A similar study on the effect of the crystallinity on the value of DMI was done before by Chen et al.[74] upon gradually mixing the interfacial atoms. This theoretical study was motivated by the observed discrepancy upon the deposition of Pt and [Co/Pd] multilayers using e-beam evaporation versus when the same multilayers were grown by magnetron sputtering. The level of atom mixing at the interface led the value of DMI to decrease gradually which was explained through the effect of layer-resolved SOC. Another theoretical study showed the robustness of the DMI value against the intermixing in Co/Pt thin films where it was found that the DMI reduces as an effect of interface disorder[75].

Moreover, it was made clear in other studies that introducing intermixing hinders the achievement of a strong interfacial DMI. It has been shown that in magnetic multilayers of heavy metal

(HM)/ ferromagnet (FM), the sign and the strength of the DMI can be highly affected by structural factors such as material composition, stacking order, and interface quality. Thus, tuning these parameters provides a way to control the DMI strength[81].
In symmetric systems like Pt/Co/Pt, the DMI at each interface are ideally equal and opposite which does not contribute to a DMI value. However, experimentally grown thin films can be deposited by tuning the temperature which increases the level of intermixing. This introduces a discrepancy in the strength of the DMI between the upper and the lower interface by breaking the inversion symmetry of the system contributing to a nonzero DMI value. This again highlights the sensitivity of interface conditions on the interfacial DMI effect[82].
In this paper, theoretical data were used as support for the experimental findings. The theoretical part, including the paragraph about the DFT calculation setup and details, the DFT data points in Figure 6, and the related data and data points in the supplementary materials were provided from my side.

4.2 PAPER II: Evolution of static and dynamic magnetic properties of Re/Co/Pt and Pt/Co/Re trilayers with enhanced Dzyaloshinskii-Moriya interaction

Applied Surface Science 679 (2025) 161151

Contents lists available at ScienceDirect

Applied Surface Science

journal homepage: www.elsevier.com/locate/apsusc

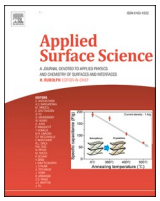

Full Length Article

Evolution of static and dynamic magnetic properties of Re/Co/Pt and Pt/Co/Re trilayers with enhanced Dzyaloshinskii-Moriya interaction

Anuj Kumar Dhiman [a,b], Amar Fakhredine [c], Ryszard Gieniusz [a], Zbigniew Kurant [a], Iosif Sveklo [a,*], Piotr Dłużewski [c], Wojciech Dobrogowski [a], Sukanta Kumar Jena [c], Aleksiej Pietruczik [c], Carmine Autieri [d], Andrzej Wawro [c], Andrzej Maziewski [a]

[a] Faculty of Physics, University of Bialystok, Białystok, Poland
[b] Faculty of Physics, Adam Mickiewicz University, Poznań, Poland
[c] Institute of Physics, Polish Academy of Sciences, Warsaw, Poland
[d] International Research Centre MagTop, Institute of Physics, Polish Academy of Sciences, Aleja Lotników 32/46, PL-02668 Warsaw, Poland

A B S T R A C T

The influence of Re layer insertion either at the bottom or top interface of epitaxially grown Pt/Co/Pt heterostructures on their static and dynamic magnetic properties is discussed in terms of their crystalline structure. Magnetic properties were studied as a function of both Re and Co layer thicknesses (d_{Re} and d_{Co}, respectively) in the matrix-like samples with a double-wedge structure, in which the layer thickness gradients were oriented orthogonally. The comprehensive investigations of the changes in coercivity, perpendicular magnetic anisotropy, spin reorientation transition, interfacial Dzyaloshinskii-Moriya interaction (iDMI) and spin wave damping are reported. Two different magnetic phases depending on the Co layer thickness with volume anisotropies (determined without demagnetization term) of K_V~0.25 (low) and K_V~0.75 MJ/m^3 (high) were observed. The relation between these phases depends on the stack sequence and thickness of Re inserted layer. For $d_{Re} = 0.2 \div 0.7$ nm deposited as the bottom interface, d_{Co} induced transition at $d_{tr} \sim 2$ nm from low to high volume anisotropy phases was observed. Low and high volume anisotropy phases are associated to Co fcc and hcp structural phases. The insertion of half atomic layer of Re had no influence on surface anisotropy but significantly enhanced iDMI above 1 pJ/m and reduced spin wave damping.

1. Introduction

The influence of heavy metal (HM) layers proximity on the magnetic properties of ultrathin ferromagnetic (FM) films such as magnetic anisotropy [1,2], interfacial Dzyaloshinskii-Moriya interaction (iDMI) [1,3,4,5,6,7], and spin wave (SW) damping [8,9] is very substantial. It depends on the thicknesses as well as FM and HM layer stacking order. Magnetic Co thin films adjacent to nonmagnetic HM layers such as Ir, Pt, Au or Pd are currently intensively studied due to the presence of perpendicular magnetic anisotropy (PMA) [10,11,12,13,14] and iDMI [15,16,17,18,19], resulting in topologically stable magnetic texture formations, e.g. skyrmions [7,20]. The influence of the thickness and the stacking order of FM-HM films (with two different heavy metals layers) were investigated in the systems containing Co [21,22,23,24,25], CoFe [21] and CoFeB [26,27,28] layers. A deep understanding of such interfacial phenomena in the wide range of FM layer thickness combined with crystalline ordering as well as HM layer thickness is necessary for engineering multilayered structures with a bigger repetition number of HM-FM units [25,29]. Unlike the bulk, ultrathin Co layers can grow in different crystallographic structures depending on substrate and growth conditions, which affect substantially magnetic properties. The d_{Co}-induced transition in Pt/Co/Pt trilayers from low volume anisotropy phase ($Kv \sim$ -0.06 MJ/m^3) to high volume anisotropy ($Kv \sim$ 0.95 MJ/m^3) was reported in Ref. [30]. This transition occurred at Co thickness $d_{tr} \sim 1.2$ nm and was related to Co fcc to hcp transition. The difference in volume anisotropy of bulk hcp Co ($Kv = 0.45$ MJ/m^3) was explained as the influence of unrealized strains. Significantly thicker magnetic films, when their thicknesses exceed lattice mismatch relaxation depth, demonstrate other structural transitions. The appearance of the hcp phase in fcc Co films was observed in Pt/Co/Pt stacks above the critical Co thickness $d_{cr} \sim 17$ nm, and d_{cr} was lowered when the top or bottom Pt layer was replaced with Ir [31]. The recorded ^{59}Co NMR spectra for 10 and 25 nm Co layers demonstrated the decrease of the fcc phase with d_{Co}, but except hcp phase two stacking fault phases were clearly detected. In thicker Co film the reverse transition from the hcp to the fcc phase was observed [32].

Recently, the magnetic properties of 3d materials (as a magnetic layer) adjacent to 5d transition metals (as capping/buffer layers) were

* Corresponding author.
E-mail address: jo@uwb.edu.pl (I. Sveklo).

https://doi.org/10.1016/j.apsusc.2024.161151
Received 12 June 2024; Received in revised form 12 August 2024; Accepted 1 September 2024
Available online 3 September 2024

analyzed *ab initio* [33,34,35,36,37]. The results suggest that Co/Re interface can induce high iDMI strength [37,38,39] with a sign opposite to Co/Pt interface. Therefore it is expected that the Co-based stack with Re/Co and Co/Pt interfaces should offer large iDMI, due to additive contribution from both interfaces. To our knowledge, so far there is only one published work [38] studying experimentally iDMI for Pt/Co/Re trilayer: samples with single the stack sequence Ti(2 nm, bottom)/Pt (2.5 nm)/Co(1.28 nm)/Re(d_{Re})/Pt(5 nm)/Ti(3 nm, top), ($d_{Re} = 0$, 0.50, 0.77, 1.04, 1.31, and 1.58 nm) deposited by magnetron sputtering.

In this work, we study the evolution of the magnetic properties in epitaxially grown Pt/Co/Pt trilayers driven by the insertion of Re to the bottom or upper interface resulting in Pt/Re/Co/Pt and Pt/Co/Re/Pt stacks, respectively. Although investigations are carried out in a wider component layer thickness range d_{Re} and d_{Co}, our particular attention is focused on substantial modifications induced by a few atomic layers (AL) of inserted Re. The obtained results are compared with those from the symmetric reference Pt/Co/Pt part of the samples. The selected thickness range of continuous Co wedge ($d_{Co} = 0 \div 3$ nm) is wide enough to observe d_{Co}-induced spin reorientation transition (SRT) from out-of-plane to in-plane magnetization state in the whole d_{Re} range, allowing us to discuss various magnetic alignments. In this system type a cooperative contribution from individual interfaces is promising to obtain a high strength of iDMI with the possibility of quasi-independent variation of either iDMI or surface anisotropy. Theoretical calculations provide a deeper insight into the role of interfacial imperfections affecting stack magnetization and iDMI strength.

2. Sample details, experimental and calculation methods

The samples were deposited on Al_2O_3(0001) substrates by molecular beam epitaxy (MBE) technique. A 40 nm thick buffer layer of Pt was deposited on the substrate kept at 750 ^{0}C providing atomically flat Pt (111) terraces with lateral sizes of 50–100 nm [40]. The sequential Co and Re layers were deposited in the orthogonal double wedge geometry: Co as the continuous wedge with thickness range $d_{Co} = 0 \div 3$ nm and Re bottom/top layer with step-like thicknesses $d_{Re} = 0$, 0.1, 0.2, …, 0.7, and 3.0 nm. The top capping Pt layer was 4 nm thick. In the case of Pt/Co/Re (d_{Re})/Pt structure top Pt layer also protects the sample from oxidation and allows to repeat similar thickness d_{Re} sequence as for Pt/Re/Co/Pt sample. Due to such geometry, the samples can be considered as a 2D matrix system with appropriate (d_{Co}, d_{Re}) thicknesses.

Structural details of the investigated samples were deduced from the reflective high energy electron diffraction (RHEED) pattern and transmission electron microscopy (TEM) images. High-resolution TEM with energy-dispersive X-ray spectroscopy measurements were carried out to investigate the quality of the epitaxial growth and interface sharpness in the layered systems.

The measurements were performed with a Titan 80–300 Cube Cs image-corrected microscope operating at 300 kV equipped with energy dispersion X-ray (EDX) detector for elemental analysis and mapping. The cross-section lamellae for the TEM-EDX investigations were prepared with a focused ion-beam (FIB) technique. Using this method a spatially uniform reference sample Pt(40)/Re(1)/Co(3)/Pt(5) (the thickness in parentheses is given in nm), was analyzed in detail. It was grown in the same conditions as the matrix samples. Therefore, one can expect that the drawn conclusions are representative of the investigated matrix samples, as well. The magnetization reversal loops were acquired by means of magneto-optical Kerr effect magnetometry setup operating in polar configuration (PMOKE) and equipped with a high-resolution CCD camera.

The whole sample area was observed in a single measurement run. A sequence of gray scale images with intensity proportional to the local Kerr rotation signal was recorded as a function of the applied magnetic field. It provides the possibility of simultaneous acquisition of the local magnetization reversal loops across the whole sample area. To enhance the magnetic signal, the image from the saturated sample was subtracted from every recorded frame. Other used PMOKE set up was equipped with a dedicated 3D magnet, enabling magnetic field application in any direction. The changes of out-of-plane magnetization as a function of appropriate in-plane and out-of-plane magnetic fields were registered. Magnetic anisotropy fields were extracted as functions of (d_{Co}, d_{Re}) with the application of the Stoner-Wohlfarth model fitting. Magnetization dynamics was investigated using Brillouin light scattering (BLS) technique. Measurements were performed in backscattering geometry measuring Damon-Eshbach mode with an application of a monochromatic green laser (with 532 nm wavelength) beam. The backscattered beam (collected by the focusing lens) was analyzed with the help of a multipass tandem Fabry Perot interferometer (TFP-II, Table Stable). Generally, the BLS spectrum captured by the TFP-II includes the signal from inelastically scattered photons with lower energy (Stokes peak) and higher energy (anti-Stokes peak). The iDMI strength was determined from the frequency shift between Stokes and anti-Stokes peaks. Measured BLS spectra also allowed us to determine magnon damping.

The modeled structures exhibit a face-centered cubic (fcc) stacking, with the lattice constant constrained to the experimental value of Pt (1 1 1), which is equal to 3.92 Å. The structures consist of five atomic layers of platinum and five layers of rhenium, with a variable number of cobalt layers, where each layer contains four atoms. The Kohn-Sham orbitals were expanded using a plane-wave basis set with a cutoff energy of 280 eV. A k-point grid of 4x12x1 was employed for sampling the Brillouin zone. All calculations were performed with structural relaxations to ensure the determination of the most stable configurations. The atoms were allowed to relax until the Hellmann-Feynman forces become less than 0.015 eV/Å. Electron core interactions described by the projector augmented wave method for the pseudopotentials was considered in the Vienna ab initio simulation package (VASP), where the exchange correlation energy is calculated within the generalized gradient approximation of the Perdew-Burke-Ernzerhof (PBE) form [41,42]. The magnetic moments were placed in a constrained manner which is crucial for calculating the iDMI using density functional theory calculations [43]. The computations followed a three-step procedure. Structural relaxations were conducted by initiating a ferromagnetic state without considering the spin–orbit coupling (SOC) effect to ascertain the most stable interfacial geometries. Subsequently, the Kohn-Sham equations were solved without spin–orbit coupling to determine the charge distribution of the system's ground state. Finally, the SOC was introduced, and the self-consistent total energy of the system was calculated as a function of the magnetic moment orientations. Consequently, the interfacial Dzyaloshinskii-Moriya interaction (iDMI) was computed following the approach outlined by Yang et al. in ref. [44]. The iDMI strength (d_{tot} [meV]) parameter was calculated from the energy differences between clockwise and anticlockwise magnetic spirals in the Co layers and was further used to calculate the micromagnetic iDMI surface strength (D_S [pJ/m]) using a conversion similar to the one used in ref. [22]. DFT calculations were also done for models where 50 % Co and 50 % Pt or Re atoms were intermixed at the first two layers of the Pt/Co and Co/Re interfaces, respectively. More details on the method used and information on extended results of the introduced system using DFT computations can be found in ref. [36].

3. Results and discussion

3.1. Structural characterization

The representative sequence of the RHEED patterns for a selected azimuth orientation between the incident electron beam and the sample (with respect to the Pt buffer along in-plane [1-10] direction) recorded after completing every component layer is shown in Fig. S1 in the Supplementary Materials. The clear and continuous streak pattern repeatedly appears every 60 degs during the sample rotation. This indicates very well-developed structural coherence and the sample

crystallinity as well as two-dimensional growth with smooth surfaces. The high-angle annular dark-field (HAADF) cross-sectional TEM images of the same reference sample (as in Fig. S1) are shown in Fig. 1 (a, b). Fig. 1 (a) depicts the low magnification image. All the visible component layer films deposited on the sapphire substrate (bright bottom fragment) are flat and continuous over lateral distances of several tens of nanometers. Due to the low difference in the *Z* parameter between Pt (Z=78) and Re (Z=75) the Z-contrast between Pt and Re layers is negligible. The high-resolution HAADF cross-sectional image [Fig. 1 (b)] with the corresponding EDX elemental line profiles aligned with each layer [Fig. 1 (c)] enables detailed insight into the sample structure with atomic resolution. The crystalline quality of the Pt buffer is perfect – a regular arrangement of atoms is very clear and corresponds to the fcc ABC-stacking sequence in the [111] growth direction. The interatomic distances for pure bulk Pt and Re differ only about 1 % (0.277 and 0.274 nm respectively), so neither lattice mismatch nor Z-contrast can be visible at Pt/Re interface. The subsequent 3 nm thick Co layer exhibits a high quality of crystalline ordering with stacking faults. At the center of the Co layer large area with hcp structure (growth direction [0001]) with AB-stacking is present while on the left-top small part with the fcc structure (growth direction [1 1 1]) with ABC-stacking can be observed. Besides it, some stacking faults are visible even inside the hcp structure. Some rows of Pt atoms in the upper layer are elongated in the [1 1 0] direction due to the interface waviness resulting in their misalignment to the incident electron beam along the [−1 1 0].

3.2. Magneto-static PMOKE characterization

Fig. 2 (a) and (b) present the remnant PMOKE images of the whole areas of the Pt/Re/Co/Pt and Pt/Co/Re/Pt matrix-type samples, respectively. Both samples have the reference stripe Pt/Co/Pt (without Re) on the left side (the boundaries are marked with vertical white dashed lines). The thickness of the Re layer changes in a step-like manner along the x-axis, while Co linear wedge 0 ÷ 3 nm extends

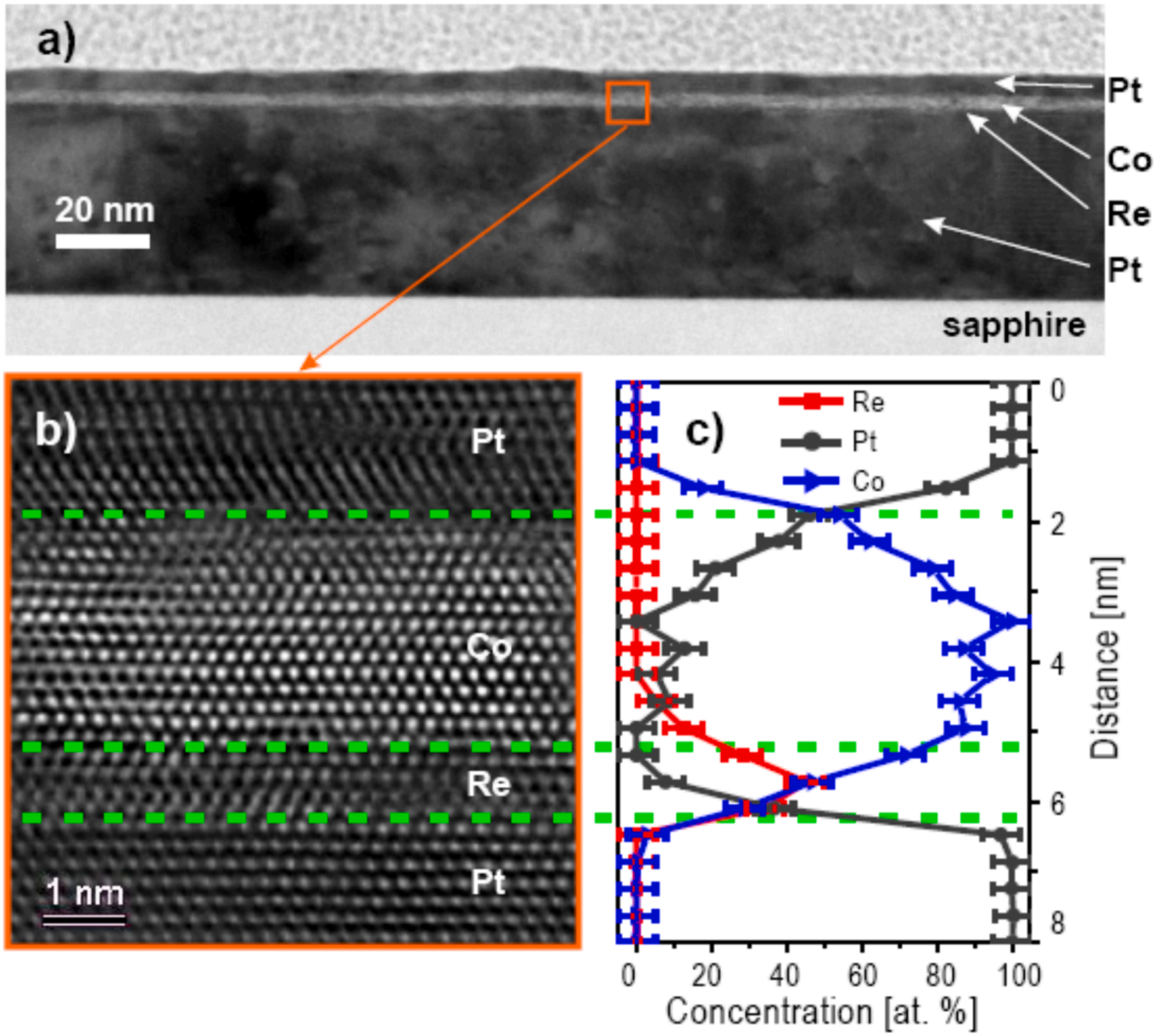

Fig. 1. TEM image of the Pt(40)/Re(1)/Co(3)/Pt(5) reference layered stack cross-section (component layer thickness is given in nm). a) low magnification image. b) high-resolution HAADF image showing atom arrangement in the individual component layers. c) EDX elemental line profile across the layered structure. Green dashed lines are drawn along the visible interfaces in (b).

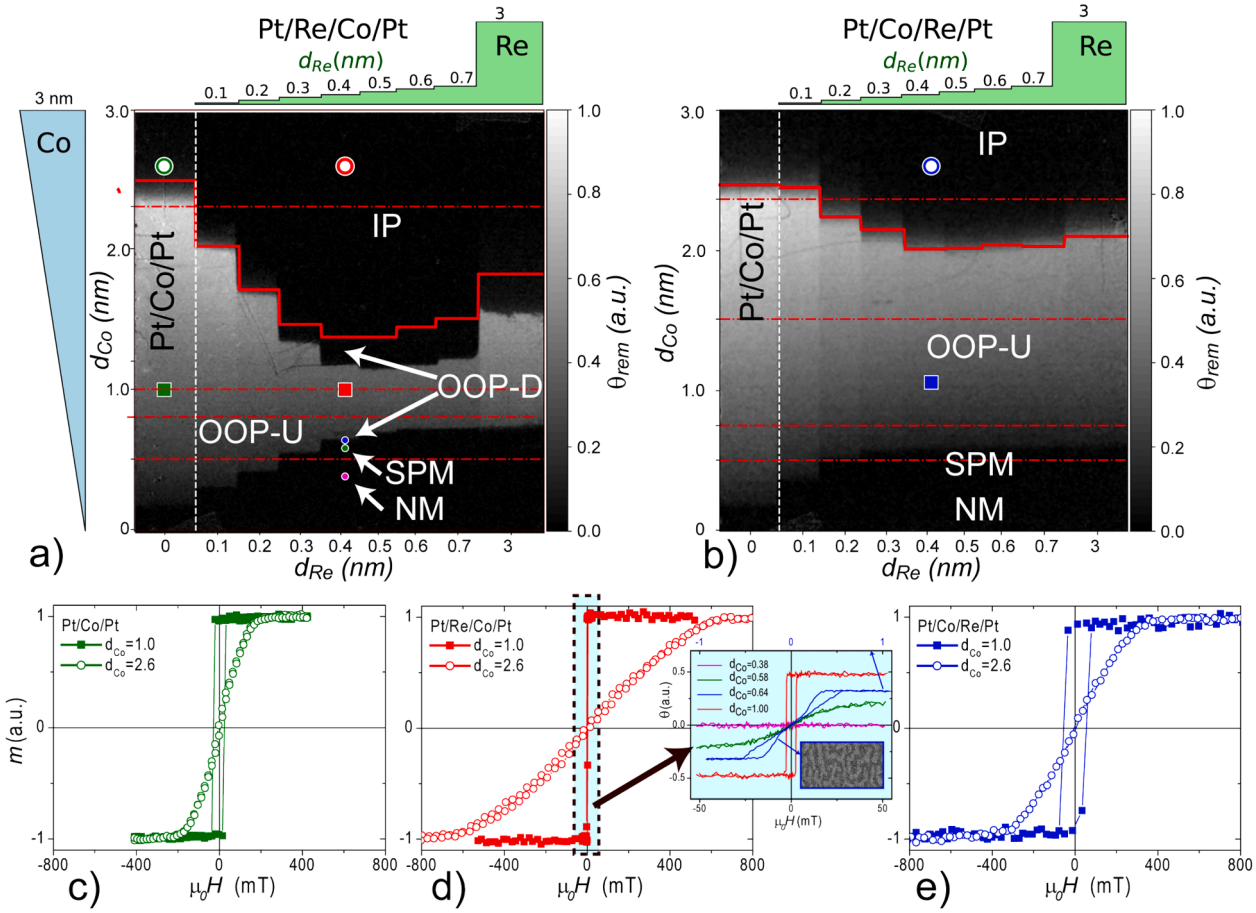

Fig. 2. PMOKE remanence images of a) Pt/Re/Co/Pt and b) Pt/Co/Re/Pt stacks with double wedge configurations: linear Co (along Y-axis) and step-like Re, (along X-axis). Various magnetic states of the sample (description in the text) are imaged as different gray-scale shades. The following magnetic states/regions are distinguished: in-plane uniform magnetization (IP), out-of-plane magnetization uniform (OOP-U), two out-of-plane regions (OOP-D) with negligible remanence and domains, superparamagnetic (SPM) and non-magnetic (NM). Step-like solid red lines indicate the d_{SRT} positions for different d_{Re}. The normalized PMOKE hysteresis loops *m(H)* for two selected thicknesses: $d_{Co} = 1.0$ nm (full squares, OOP-U) and $d_{Co} = 2.6$ nm, (empty circles, IP) are shown for: c) Pt/Co/Pt; d) Pt/Re(0.4)/Co/Pt (the inset represents the non-normalized *m(H)* in the smaller field range, marked by light-blue rectangle, for $d_{Co} = 0.38$, 0.58, 0.64 and 1.0 nm; for $d_{Co} = 0.64$ nm the loop is referred to the top x-axis and in the blue envelope the magnified 45 x 15 μm^2 remanence domains structure is shown); e) Pt/Co/Re(0.4)/Pt. In the Figs. a), b) the appropriate colored and shaped symbols indicate the spots where presented hysteresis loops were measured. Horizontal thin dash-dot red lines in Fig. 2 a, b mark the positions of coercivity profiles shown in Fig. 3 a,b.

along the y-axis as shown in the schematic sample structure. Three magnetization regions can be distinguished in the remanence images obtained from both Pt/Re/Co/Pt and Pt/Co/Re/Pt stacks:

(i) bottom black (negligible remanence, marked in Fig. 2a, b as "NM, SPM"), thin d_{Co} range; in this area the following magnetic states appear with the increase in d_{Co}: non-magnetic (NM); superparamagnetic (SPM) and out-of-plane magnetization state with domains (OOP-D) and negligible coercivity (see domain image in the inset to Fig. 2d for Pt/Re(0.4)/Co(0.64)/Pt) similar to Pt/W(2.4 nm)/Co(0.6 nm) /Pt [45].

(ii) middle bright out-of-plane uniform magnetization state (OOP-U), characterized by rectangular hysteresis loops and normalized remanence equal to one, see Fig.S2 in Supplementary Materials.

(iii) top black region: negligible remanence, marked as in-plane (IP) uniform ferromagnetic zone, appearing in both stacks (Fig. 2 a, b); additionally in Pt/Re/Co/Pt film in the lower d_{Co} range again the out-of-plane magnetization state with domains OOP-D is observed (Fig. 2 a). Magnetic anisotropy measurements, discussed below, enable the determination of Co thickness d_{SRT} (d_{Re}) at which spin reorientation transition (SRT) occurs. The red solid lines visible in both PMOKE images separate the regions with IP ($d_{Co} > d_{SRT}$) and OOP-D ($d_{Co} < d_{SRT}$) magnetic orderings.

A qualitative comparison of the remanence images [Fig. 2 (a) and (b)] reveals that the bottom Re layer modifies the remanent state more significantly than Re overlayer with respect to the reference Pt/Co/Pt part. In both configurations, the border between the bottom dark and gray OOP uniform areas looks similar. However, the location of the upper gray/dark area border is much more sensitive to d_{Re} in the Pt/Re/Co/Pt stack. Moreover, this border is shifted toward smaller d_{Co}, reducing substantially the d_{Co} range with PMA. It should be emphasized that even Re atomic submonolayer significantly affects magnetic properties. Drastic suppression in d_{Co} range with PMA occurs in the lower range $d_{Re} = 0.1 \div 0.5$ nm followed by its moderate expansion up to $d_{Re} =$ 3 nm. The exemplary PMOKE hysteresis loops illustrating magnetization reversal processes for the indicated sample zones are shown in Fig. 2 (c)-(e). Two different shapes typical of out-of-plane ($d_{Co} = 1.0$ nm, square loop) and in-plane ($d_{Co} = 2.6$ nm, reversible loop) magnetizations are very clear. The inset of Fig. 2d (magnified x-scale) shows magnetization curves for different magnetic states: with the increase in d_{Co}, the PMOKE signal increases and the curve shape changes successively from: (i) NM ($d_{Co} = 0.38$ nm), via (ii) SPM ($d_{Co} = 0.58$ nm), (iii) OOP-D domains ($d_{Co} = 0.64$ nm) and finally into (iv) OOP-U monodomain ($d_{Co} = 1.00$ nm) and characterized by a square loop.

In the reference layer Pt/Co/Pt while decreasing d_{Co} from IP uniform state thickness range coercivity field H_C increases reaching maximum H_{CMAX} (≈435 mT) at d_{CoMAX}=0.4 nm and then decreases down to zero at SPM. The existence of large H_{CMAX} was observed for different ultrathin

magnetic layers, e.g. [46], and is ascribed to the magnetic non-continuity at low thicknesses.

The Re insertion has a strong influence on the coercivity field H_C. In comparison to the reference layer Pt/Co/Pt, H_{CMAX} in Pt/Re/Co/Pt decreases about 200 times, respectively. A similar effect has been recently reported for W insertion [47]. This strong decrease one can relate with: (i) decrease in domain wall energy density (which decreases H_C), this energy is expressed as $4\sqrt{A_{ex}K_{eff}} - \pi|D_{eff}|$, where A_{ex} is the exchange stiffness, K_{eff} – effective uniaxial anisotropy energy, and D_{eff} – effective iDMI constant [3,48]; (ii) Co intermixing at the buffer interface, strong H_{CMAX} (≈17 mT) decrease was reported in Pt/Co/Pt layers, where Co-Pt intermixed interfaces were observed [49]; (iii) creation of defects influencing domain wall motion and nucleation different than in the reference Pt/Co/Pt layers. H_{CMAX} decreases four times in Pt/Co/Re/Pt layers with Re overlayer. In this case, the Re deposition on Co layer has a rather minor influence on already formed its crystallographic structure, so mainly near Co/Re interface changes are expected. A similar small H_{CMAX} decrease was observed after Co coverage with Ag or W [46,47]. The influence of Re insertion thickness on coercivity field $H_C(d_{Re}, d_{Co} =$ const) is illustrated in Fig. 3. Three classes of Re induced H_C modifications d_{Co} were selected. Two of them are connected with d_{Re} driven transition from OOP-U state into negligible remanence states: (i) IP state – lines $d_{Co} = 2.3$ nm and (ii) SPM state – lines $d_{Co} = 0.5$ nm. H_C decrease is the biggest in these two classes – from large H_C reference in Pt/Co/Pt into zero in structures with Re insert. The third class of Re insertion driven H_C modifications is presented also while changing d_{Re} within OOP-D state in: (i) Pt/Re/Co/Pt along lines $d_{Co} = 0.8$ and 1 nm, Fig. 3a H_C decrease is noticeable; (ii) Pt/Co/Re/Pt along lines: $d_{Co} = 1.5$ ($H_C(d_{Re})$ changes are negligible) and $d_{Co} = 0.8$ nm $H_C(d_{Re})$ function is non-monotonic with H_C maximum – it is connected with Re induced extension (into higher d_{Co}) of the region of existing of OOP-D/SPM state and it results in H_{CMAX} shift to the higher d_{Co}.

3.3. Magnetic anisotropy studies

The magnetic anisotropy field H_{eff}, considered in the single domain model as the saturation field in the hard direction, was extracted from the PMOKE measurements performed in the crossed perpendicular and in-plane applied magnetic fields [50]. The uniaxial effective magnetic anisotropy K_{eff} is related to the magnetic anisotropy field H_{eff} as $H_{eff} = \frac{2K_{eff}}{\mu_0 M_S}$. Here μ_0 is the vacuum permeability and M_S – the saturation magnetization of Co. K_{eff} can be decomposed into the volume (K_V) and surface (K_S) anisotropy contributions [51], demagnetizing term $-\frac{1}{2}\mu_0 M_S^2$, and intrinsic effective anisotropy constant K'_{eff}, according to the following relation:

$$K_{eff} = \frac{K_S}{d_{Co}} + K_V - \frac{1}{2}\mu_0 M_S^2 = K'_{eff} - \frac{1}{2}\mu_0 M_S^2 \quad (1)$$

K_S contains a sum of contributions from both the bottom and upper interfaces and here the magnetization saturation for both stacks was used as for bulk Co – M_S=1.4 x 10^3 kA/m.

Fig. 4 displays the anisotropy dependence K'_{eff} on d_{Co} in both stacks: (a) Pt/Re/Co/Pt and (b) Pt/Co/Re/Pt. From the fit of the linear part of $K'_{eff} \cdot d_{Co}$ (d_{Co}) one can derive the surface (cross-section with Y-axis) and volume (inclination) anisotropy contributions. Similar values of K_S=2.3 mJ/m^2 and $K_V = 0.25$ MJ/m^3 were determined by the reference parts of both stacks. For Pt/Re/Co/Pt sample in the case of 3 nm Re buffer K_S is reduced to 0.9 mJ/m^2 but K_V rises to 0.7 MJ/m^3 (Fig. 5a). For intermediate d_{Re} thicknesses the inclination $K_{eff} \cdot d_{Co}$ (d_{Co}) changes at $d_{Co} \sim 2$ nm (see dependence for $d_{Re} = 0.5$ nm in Fig. 4a; all data are given in Figs S3 Supplementary Material) and two pairs of K_S, K_V parameters can be determined, and low and high volume magnetic anisotropies phases can be observed. The change of Co volume magnetic anisotropy on d_{Co} was reported earlier [30] and it was connected with d_{Co} induced fcc to hcp Co structure transition that occurred there at $d_{tr} \sim 1.2$ nm. By analogy, we conclude that observed in Pt/Re/Co/Pt stack low and high volume magnetic anisotropies phases are connected with the occurrence of fcc and hcp phases, respectively. In other words, Re buffer thickness induces fcc-hcp structural transition in the Co layer and both surface $K_{S,fcc}$, $K_{S,hcp}$, and volume anisotropies $K_{V,fcc}$, $K_{V,hcp}$ for Pt/Re/Co/Pt stack can be determined for these crystalline orderings (Fig. 4a, 5a).

In the case of Pt/Co/Re/Pt stack Re overlayer reduces K_S but has negligible influence on the volume magnetic anisotropy $K'_{eff} \cdot d_{Co}$ (d_{Co}) dependences slopes are similar (Fig. 4b and Fig.S3 c,d in Supplementary Materials). The thickness of Re overlayer has no influence on fcc structure of the deposited earlier Co layer.

The above anisotropies considerations lead to the following findings. In the reference Pt/Co/Pt stacks the low volume $K_{V,fcc} = 0.3$ MJ/m^3 anisotropy phase with large surface $K_{S,fcc} = 2.2$ mJ/m^2 are observed, which is typical of fcc lattice structure [30,52]. $K_{V,fcc}$ is significantly smaller than the demagnetization term of −1.2 MJ/m^3. The samples prepared by sputtering technique [13] exhibit similar values of K_V, however K_S is twice smaller there. The insertion of 0.1 nm Re at the bottom interface [Pt/Re/Co/Pt stack, Fig. 5(a)] causes small changes (~0.1 MJ/m^3) in $K_{V,fcc}$. When d_{Re} exceeds 0.2 nm, hcp phase appears with $K_{V,hcp} = 0.66$ MJ/m^3 and for the thickest of the bottom Re layer ($d_{Re} = 3$ nm) the volume contribution $K_{V,hcp}$ is enhanced up to 0.76 MJ/m^3; similar K_V values for Co films were reported earlier [46,52,53]. Due to the insertion of Re to the bottom interface the surface anisotropy is strongly suppressed when hcp phase appears ($d_{Re} > 0.2$ nm), while $K_{S,hcp}$ is always approximately twice smaller than $K_{S,fcc}$.

In the case of Pt/Co/Re/Pt stack the changes of K_S, K_V are not so drastic [Fig. 5(b)]: the hcp phase was not observed and K_S slightly decreases to 2 mJ/m^2, while K_V oscillates around 0.25 ± 0.05 MJ/m^3. It can be explained by the minor influence of the upper Re layer on the Co layer crystalline structure already deposited on the Pt buffer. The

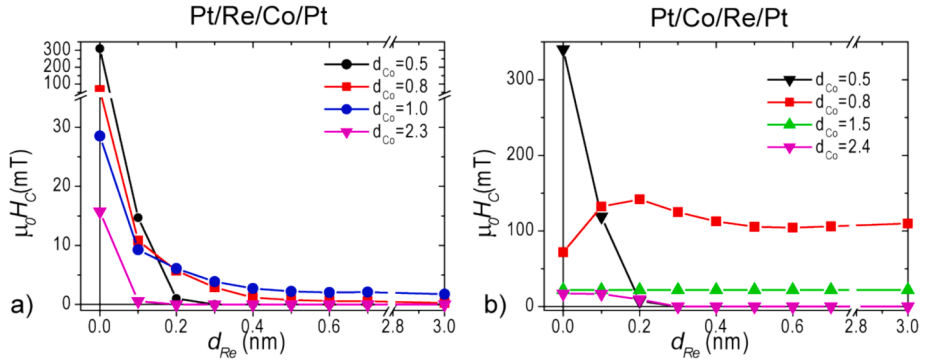

Fig. 3. Coercive field $\mu_0 H_C$ as a function of d_{Re} plotted for selected d_{Co} thicknesses measured along the red dash-dot lines shown in Fig. 2a,b: a) Pt/Re/Co/Pt for d_{Co} = 0.5, 0.8, 1.0, and 2.3 nm; b) Pt/Co/Re/Pt for d_{Co} = 0.5, 0.8 1.5, and 2.4 nm.

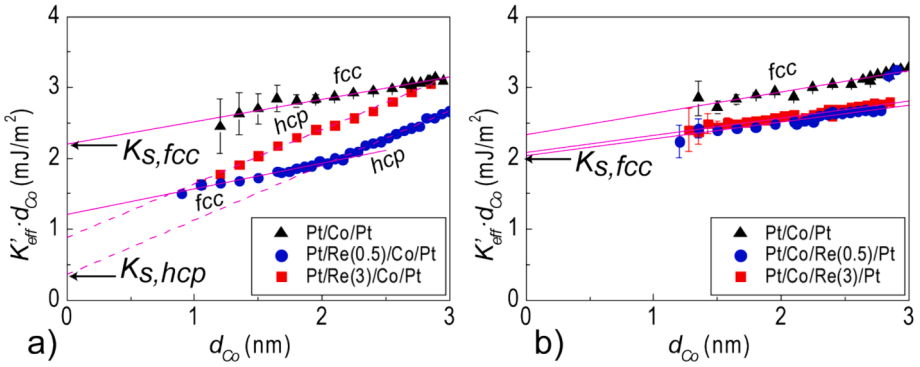

Fig. 4. The selected dependencies of $K'_{eff}{\cdot}d_{Co}$ on d_{Co} for: a) Pt/Re/Co/Pt and b) Pt/Co/Re/Pt stacks and the reference region Pt/Co/Pt. The linear fittings (solid magenta) correspond to the fcc phase whereas these for the hcp phase are shown as dashed lines. The K_V and K_S values are obtained from the slope and y-axis crossing of the fitting straight lines.

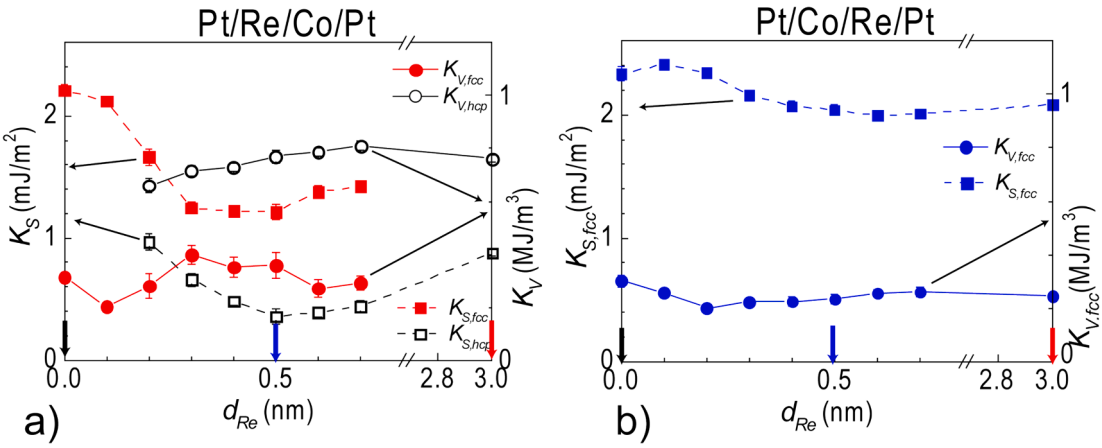

Fig. 5. The dependences of $K_{S,fcc}$, $K_{S,hcp}$ (left y-axis) and $K_{V,fcc}$, $K_{V,hcp}$ (right y-axis) on d_{Re} for: a) Pt/Re/Co/Pt and b) Pt/Co/Re/Pt stacks. The vertical arrows (black, blue, and red) indicate selected d_{Re} thicknesses, for which the data are shown in Fig. 4.

presence of Co fcc phase is expected in the full range of overlayer Re thickness.

The observed difference between K_S values of Pt/Re/Co/Pt and Pt/Co/Re/Pt is attributed to asymmetry of the top–bottom interface anisotropy in the reference Pt/Co/Pt system with major contribution arising from the bottom interface, being related to the interface roughness [54,55]. Furthermore, we observe the reduction in K_S for fcc to hcp transition while layer ordering remains the same. The difference in K_S for fcc and hcp stacking was reported in [37].

The reference Pt/Co/Pt structure reveals $d_{SRT} \approx 2.8$ nm which is significantly larger than d_{SRT} in the similar trilayers deposited by sputtering [49,56]. Generally, the variation of d_{SRT} values for Pt/Co/Pt trilayers is due to K_S ($K_{eff} = 0$ it means $d_{SRT} = K_S/(0.5\mu_0 M_S^2 - K_V)$ is mainly defined by demagnetizing term and results as a difference between deposition techniques [11,13,47,57]. The abrupt changes in d_{SRT} are observed while introducing the Re at the bottom or upper interfaces (see Fig. 2a,b). In the case when Re is a bottom layer, d_{SRT} is reduced to a minimal value (~1.5 nm) for $d_{Re} \approx 0.5$ nm followed by a moderate increase for the bigger Re thicknesses. Meanwhile, placing the Re layer in the upper interface affects d_{SRT} in a weaker way and a minimum $d_{SRT} \approx$ 2.0 nm is achieved for $d_{Re} \approx 0.5$ nm. The Pt/Re/Co/Pt stack depicts a decent increase in d_{SRT} value for the bigger Re layer thickness.

3.4. Dynamical study in BLS measurements

BLS spectroscopy measurements were carried out for the samples saturated with in-plane applied magnetic field perpendicular to the wave vector $\vec{k}$, where the intrinsic non-reciprocity of the classical Damon-Eshbach SW mode can be observed. Using this approach, the strength of iDMI can be calculated from the frequency shift between Stokes (f_S) and anti-Stokes (f_{aS}) lines $\Delta f = f_{aS} - f_S$ [6,16,18]. This method allows us also to investigate a sign of iDMI which defines the chirality of magnetic textures and the motion direction of chiral structures under the influence of magnetic fields and/or electric current.

The effective iDMI constant D_{eff} characterizing the strength of this interaction can be determined from the following equation [16,58,59]:

$$\Delta f = \frac{2\gamma}{\pi M_S} D_{eff} k \tag{2}$$

where γ – gyromagnetic ratio (176 GHz/T), M_S – saturation magnetization taken as for bulk cobalt M_S=1400 kA/m, D_{eff} – the iDMI effective (thickness-averaged) coefficient.

In order to determine the dependence of the surface coefficient D_S ($D_S = D_{eff}{\cdot}d_{Co}$) on d_{Co}, the series of BLS measurements were conducted for in-plane magnetization saturated state (light incident angle of 30^0 corresponds to spin wave (SW) wavevector $k = 11.81$ μm^{-1}). $|D_S|$ as a function of d_{Co} in Pt/Re(3)/Co/Pt (red squares) and Pt/Co/Re(3)/Pt (blue circles) structures is plotted in Fig. 6. Mean magnitudes of $D_S \approx$2.3 pJ/m for Pt/Re/Co/Pt and $D_S \approx$-1.8 pJ/m for Pt/Co/Re/Pt are found. The positive sign of iDMI for Pt/Re/Co/Pt stack is the same as for Ir/Co/Pt structure, while the negative sign possessed by Pt/Co/Re/Pt system corresponds to Pt/Co/Ir [18]. The large D_S values for both our system stacks are similar to D_S=2.1 pJ/m obtained for sputtered Pt/Co/Re films [38]. Small difference in $|D_S|$ value between Pt/Co/Re/Pt and Pt/Re/

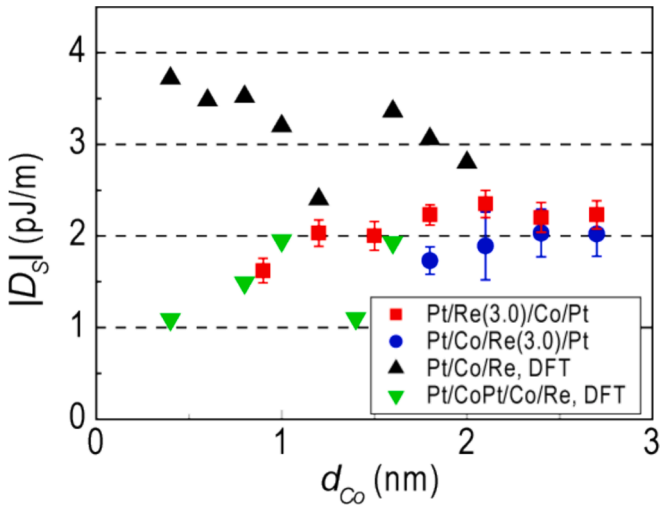

Fig. 6. $|D_S|$ as a function of d_{Co} for Pt/Re(3)/Co/Pt (red squares) and Pt/Co/Re (3)/Pt (blue circles) stacks. Black triangles illustrate the DFT calculated D_S value for the Pt(5AL)/Co/Re(5AL) structure with sharp interfaces, whereas green triangles with 50 % alloyed (CoPt) Pt/Co interface. Data for DFT calculations were taken from [36] and extended here by additional point d_{Co} = 1.6 nm for mixed Co/Pt interface.

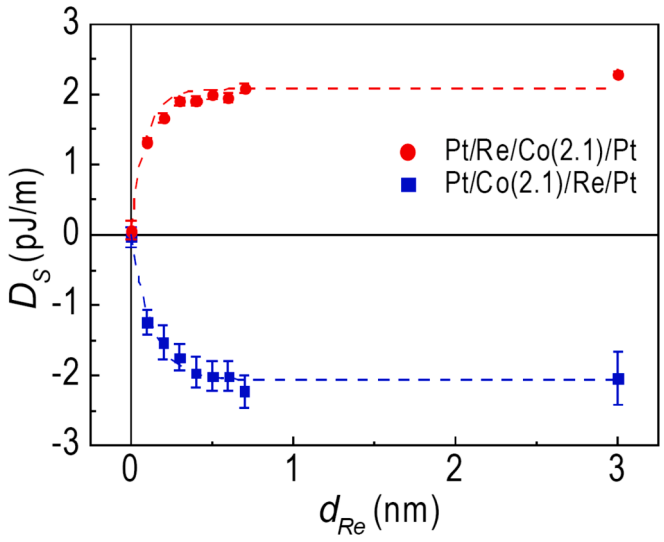

Fig. 7. Dependence of D_S on Re layer thickness d_{Re} for Pt/Re/Co/Pt (red squares) and Pt/Co/Re/Pt (blue circles) stacks with d_{Co} = 2.1 nm. The measurements were carried out for the wave vector k = 11.81 μm^{-1} and in-plane applied saturating field $\mu_0 H$=-0.57 T. Dashed lines are used as eye guides.

Co/Pt stacks indicates the dissimilarity in iDMI energies of the Co/Pt and Co/Re type interfaces depending on the layer sequence order. The Co layer in Pt/Re(3)/Co/Pt grows in hcp phase while in Pt/Co/Re(3)/Pt – in fcc. However, the changes in D_S are relatively small in comparison to $K_{S,fcc}$ and $K_{S,hcp}$ discussed above.

DMI strength was also calculated using DFT for Pt (5AL)/Co(d_{Co})/Re (5AL) stack (AL – atomic layer). In the first approach, the calculations were performed for the case of perfect interfaces and the thickness d_{Co} ranging from 1 AL to 10 AL. The obtained values are evidently larger than those obtained experimentally (Fig. 6). The observed difference can be attributed to intermixing effects at the interfaces [60]. To investigate deeper the influence of the interface structure on experimentally observed effects, we implemented DFT calculations including intermixing at the interface for selected thicknesses of cobalt. The alloyed interface of the system is made of two layers of adjacent Co and Pt atomic layers forming double atomic mixed layers in proportions of 50 % Pt and 50 % Co atoms distributed uniformly to ensure the conservation of the total number of atoms of each element. The calculations were performed for clockwise (CW) and anticlockwise (ACW) spin spirals placed for the remaining full Co layers. In the case of intermixing at the Pt/Co interface, the iDMI strength is lowered by 40 % in comparison to the case of perfect interfaces, as similarly reported in ref. [61] which effectively reproduces the experimental results (Fig. 6). This decrease aligns with the anticipated outcome, as the Co atoms within the mixed layers counteract each other, resulting in a cancellation of their contribution to the iDMI and ultimately yielding an iDMI value of zero. In addition, the presence of half of the Pt atoms at the interface with Co provides a reduction in the strength of SOC which eventually lowers the overall value of the iDMI [62]. The reason lies in the interfacial nature of iDMI and in the fact that the mixed layers do not contribute as much as in the case of perfect interfaces. On the other hand, looking at the case where the intermixing takes place at the Co/Re interface (results not included), the iDMI did not substantially get affected and the contribution is almost the same as in the case of the perfect interface. We could conclude that the intermixing at the Pt/Co interface has a significant impact on the iDMI, leading to a notable decrease in its value which aligns with the experimental findings indicating that improved crystallinity leads to increased iDMI magnitude.

The dependences of $D_S(d_{Re})$ in Pt/Re/Co/Pt and Pt/Co/Re/Pt (d_{Co} = 2.1 nm) samples are shown in Fig. 7. The changes of iDMI strength as a function of adjacent HM layer thickness were reported previously for Co [21,22,63] and CoFeB [27,28,64] layer containing systems. It is visible that for d_{Re} = 0 nm, i.e. the symmetric reference Pt/Co/Pt stack, the magnitude of D_S is negligible (<0.07 pJ/m), what is in agreement with zero DMI observed in similar MBE grown Pt/Co/Pt symmetric trilayers [15]. With d_{Re} increase the D_S value changes abruptly and the saturation is achieved at d_{Re} = 0.4 nm (=2 ALs) at the level slightly above 2 pJ/m, which coincides with the formation of continuous epitaxial layer Re (0001) on Pt(111) [65] and it is similar to that obtained for sputtered Pt/Co/Re trilayers in ref. [38]. Here, it should be mentioned that iDMI is a pure interface effect like in the case of K_S but Co interface stacking order may have different influences on D_S and K_S [37].

In metallic systems, the Gilbert damping coefficient (α) is significantly enhanced [8] mainly due to the presence of conduction electrons. However, the adjacent non-magnetic HM layer also affects damping through the sink of spin angular momentum to the HM layer. The efficiency of this process depends on the spin diffusion length in HM. The engineering of α can be performed by the thickness and stack order of HM layer [8,66,67].

In Fig. 8(a) the BLS spectra measured in Pt/Co/Pt (black), Pt/Re (0.7)/Co/Pt (red) and Pt/Co/Re(0.7)/Pt (blue) stacks with d_{Co} = 2.1 nm are shown. Full width at half maximum (*FWHM*) of Stokes ($FWHM_S$) and anti-Stokes ($FWHM_{aS}$) peaks are extracted from the Lorentzian fits. Usually, the linewidth is considered as a qualitative indicator of damping value [16,21] and connected with spin conductivity [68], which can also be calculated by exploiting more complex procedure and relation between the average *FWHM* value $\delta F = (FWHM_S + FWHM_{aS})/2$ and the applied magnetic field (taking into account inhomogeneous residual linewidth [21]). In Fig. 8(a), the reference structure of Pt/Co/Pt is characterized by the linewidth around 4.5 GHz. With insertion of Re to the bottom interface (Re/Co) the average linewidth δF falls promptly within a single AL down to 2 GHz, and its value is saturated for d_{Re} > 0.6 nm [the red squares in Fig. 8(b)]. This characteristic width $\delta F(d_{Re})$ dependency is similar to the case where hafnium reduces the Gilbert damping in FeCoB/Pt system [69]. Insertion of Re to the upper Co/Pt interface (blue circles) exhibits a weak influence on δF, which is rather connected with the big roughness of the Co layer surface. To isolate it entirely from the covering Pt layer a significantly thicker Re layer should be deposited on the Co layer in comparison to the analogue case for the smooth Pt buffer surface. δF as a function of d_{Co} was determined for both Pt/Re/Co/Pt and Pt/Co/Re/Pt stacks and presented in Fig. S6 in

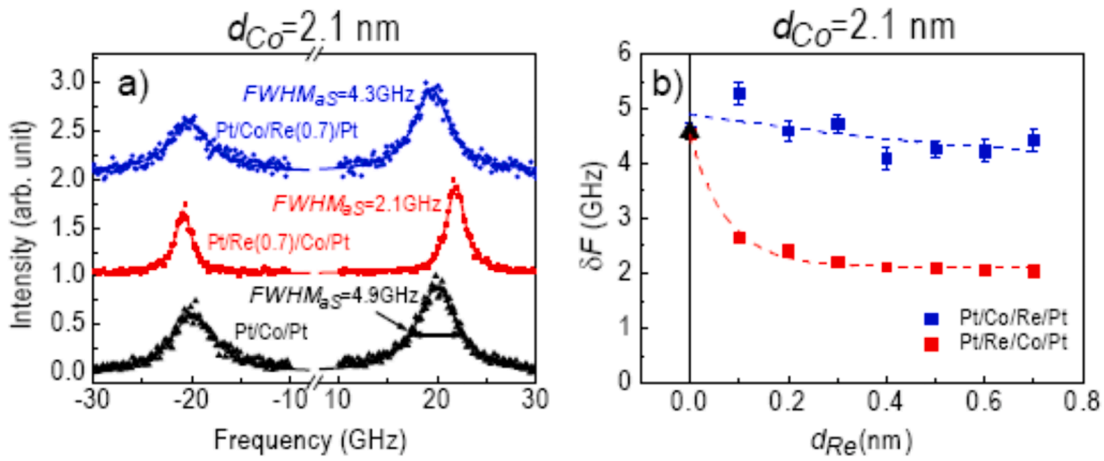

Fig. 8. a) BLS spectra and their Lorentzian fits with determined anti-Stokes line widths $FWHM_{aS}$ for d_{Co} = 2.1 nm in Pt/Co/Pt (black triangles), Pt/Re(0.7)/Co/Pt (red squares) and Pt/Co/Re(0.7)/Pt (blue dots) stacks. b) The dependences of the average δF in Pt/Re/Co/Pt and Pt/Co/Re/Pt stacks on d_{Re}. The black triangle indicates an average δF for the reference Pt/Co/Pt stack (d_{Re} = 0). Dashed lines are used as eye guides.

Supplementary materials. δF decreases while increasing d_{Co} and δF for Pt/Co/Re/Pt stack is larger (in comparison to Pt/Re/Co/Pt one) in the whole d_{Co} range. For a quantitative description and a better understanding of these results, more detailed studies of interfacial contribution to damping parameter are required. Nonetheless, our qualitative findings suggest that manipulation with the linewidth value is possible by introducing a rather thin Re layer at the bottom Co/Pt interface, while modification of the upper Co/Pt interface exhibits weaker influence on damping.

4. Conclusions

Interface-related static and dynamic magnetic properties, characterized by such parameters as: (i) coercivity field H_C, (ii) magnetic anisotropy effective field H_{eff}, (iii) DMI strength D_S and (iv) *FWHM* linewidth were studied as a function of component layer thicknesses (d_{Co}, d_{Re}) in Pt/Re(d_{Re})/Co(d_{Co})/Pt and Pt/Co(d_{Co})/Re(d_{Re})/Pt sandwiches. The relations of all these parameters determined for both stack sequences are explained in the context of the Co layer growth mode and interface quality. In general, the predominant influence is exerted by the bottom non-magnetic layer. Insertion of the Re layer is very effective and strong changes of these parameters are observed for the thickness range as small as 0.1–0.2 nm. In comparison to the reference Pt/Co(d_{Co})/Pt region, the coercivity abruptly decreases in Pt/Re/Co/Pt whereas the decrease in coercivity is observed only for $d_{Co} < 0.4$ nm in Pt/Co/Re/Pt stacks. The d_{Co}-induced transition from the phase with low volume anisotropy to high volume anisotropy was observed. This transition is driven by the buffer d_{Re} thickness and occurred at $d_{Co} \sim 2$ nm. Surface anisotropy of low magnetocrystalline anisotropy (MCA) phase is twice bigger than in the case of high MCA one, while it has negligible influence on iDMI strength. The low MCA phase is ascribed to the Co fcc structure whereas the high MCA to the hcp structure. This effect is explained by Co layer structural transformation from fcc to hcp phase, as both phases are visible in TEM images. In the case of Pt/Co/Re/Pt system, the upper Re layer does not influence significantly the crystallinity of the already deposited Co layer. D_S reaches a large value as high as 2 pJ/m and due to the different sequence of the component layers its sign is positive in Pt/Re/Co/Pt and negative in Pt/Co/Re/Pt stacks. The linewidth of Stokes and anti-Stokes lines becomes smaller with increasing thickness of Re layer in the Pt/Re/Co/Pt stack evidencing a lower damping than in Pt/Co/Pt system, where enhanced spin pumping may play a substantial role. DFT calculations of sandwich magnetization and iDMI strength were performed for two different interface quality (perfect or mixed). These calculations well describe qualitatively the induced changes in magnetic properties by Re layer insertion and predict with good accuracy the iDMI strength, offering a deeper insight into the real fine crystalline structure of the studied sandwiches. Understanding the magnetic parameters driven by the thickness of the Re layer is essential for further studies of interlayer coupling and stack designing toward the successful fabrication of heterostructures with desired properties, e.g. artificial antiferromagnets hosting skyrmion textures.

CRediT authorship contribution statement

Anuj Kumar Dhiman: Writing – review & editing, Writing – original draft, Investigation. **Amar Fakhredine:** Writing – original draft, Investigation. **Ryszard Gieniusz:** Writing – original draft, Investigation. **Zbigniew Kurant:** Writing – original draft, Investigation. **Iosif Sveklo:** Writing – review & editing, Writing – original draft, Investigation, Data curation. **Piotr Dłużewski:** Writing – original draft, Investigation. **Wojciech Dobrogowski:** Writing – original draft, Investigation. **Sukanta Kumar Jena:** Writing – review & editing, Writing – original draft, Investigation. **Aleksiej Pietruczik:** Investigation. **Carmine Autieri:** Writing – review & editing, Writing – original draft, Investigation. **Andrzej Wawro:** Writing – review & editing, Writing – original draft, Supervision, Funding acquisition, Conceptualization. **Andrzej Maziewski:** Writing – review & editing, Writing – original draft, Supervision, Funding acquisition, Conceptualization.

Declaration of competing interest

The authors declare that they have no known competing financial interests or personal relationships that could have appeared to influence the work reported in this paper.

Data availability

Data will be made available on request.

Acknowledgements

We would like to acknowledge Polish National Science Center projects as our funding source: OPUS-19 (2020/37/B/ST5/02299) and M-ERA.NET 3 (2022/04/Y/ST5/00164). C. A. is supported by the Foundation for Polish Science through the International Research Agendas program co-financed by the European Union within the Smart Growth Operational Programme (Grant No. MAB/2017/1). A.F. and C. A. acknowledge the access to the computing facilities of the

Interdisciplinary Center of Modeling at the University of Warsaw, Grant g91-1418, g91-1419 and g91-1426 for the availability of high-performance computing resources and support. We acknowledge the CINECA award under the ISCRA initiative IsC99 “SILENTS”, IsC105 ”SILENTSG“ and IsB26 ”SHINY“ grants for the availability of high-performance computing resources and support. A. F. and C. A. acknowledge the access to the computing facilities of the Poznan Supercomputing and Networking Center Grant No. 609. SKJwould like to acknowledge the Foundation for Polish Science (FNP) under the European Regional Development Fund– Program [REINTEGRATION 2017 OPIE 14-20].

Appendix A. Supplementary data

Supplementary data to this article can be found online at https://doi.org/10.1016/j.apsusc.2024.161151.

References

[1] F. Hellman, A. Hoffmann, Y. Tserkovnyak, G.S.D. Beach, E.E. Fullerton, C. Leighton, A.H. MacDonald, D.C. Ralph, D.A. Arena, H.A. Dürr, P. Fischer, J. Grollier, J.P. Heremans, T. Jungwirth, A.V. Kimel, B. Koopmans, I.N. Krivorotov, S.J. May, A.K. Petford-Long, J.M. Rondinelli, N. Samarth, I.K. Schuller, A.N. Slavin, M.D. Stiles, O. Tchernyshyov, A. Thiaville, B.L. Zink, Rev. Mod. Phys. 89 (2017) 025006, https://doi.org/10.1103/RevModPhys.89.025006.
[2] M.T. Johnson, P.J.H. Bloemen, F.J.A. den Broeder, J.J. de Vries, Rep. Prog. Phys. 59 (1996) 1409, https://doi.org/10.1088/0034-4885/59/11/002.
[3] A. Crépieux, C. Lacroix, J. Magn. Magn. Mater. 182 (1998) 341–349, https://doi.org/10.1016/S0304-8853(97)01044-5.
[4] M. Heide, G. Bihlmayer, S. Blügel, Phys. Rev. B 78 (2008) 140403, https://doi.org/10.1103/PhysRevB.78.140403.
[5] A. Thiaville, S. Rohart, E. Jué, V. Cros, A. Fert, Europhys. Lett. 100 (2012) 57002, https://doi.org/10.1209/0295-5075/100/57002.
[6] J. Cho, N. Kim, S. Lee, J.S. Kim, R. Lavrijsen, A. Solignac, Y.X. Yin, D.S. Han, N.J. J. van Hoof, H.J.M. Swagten, B. Koopmans, C.Y. You, Nat. Commun. 6 (2015) 7635, https://doi.org/10.1038/Ncomms8635.
[7] A. Fert, N. Reyren, V. Cros, Nat. Rev. Mater. 2 (2017) 17031, https://doi.org/10.1038/natrevmats.2017.31.
[8] S. Azzawi, A. Hindmarch, D. Atkinson, J. Phys. D. Appl. Phys. 50 (2017) 473001, https://doi.org/10.1088/1361-6463/aa8dad.
[9] S. Akansel, A. Kumar, V.A. Venugopal, R. Esteban-Puyuelo, R. Banerjee, C. Autieri, R. Brucas, N. Behera, M.A. Sortica, D. Primetzhofer, S. Basu, M.A. Gubbins, B. Sanyal, P. Svedlindh, Phys. Rev. B 99 (2019) 174408, https://doi.org/10.1103/PhysRevB.99.174408.
[10] P.F. Carcia, A.D. Meinhaldt, A. Suna, Appl. Phys. Lett. 47 (1985) 178–180, https://doi.org/10.1063/1.96254.
[11] J.A.C. Bland, B. Heinrich, Ultrathin Magnetic Structures I, Springer, Berlin, 1994.
[12] V. Grolier, J. Ferré, A. Maziewski, E. Stefanowicz, D. Renard, Appl. Phys. 73 (1993) 5939, https://doi.org/10.1063/1.353528.
[13] Y.-C. Lau, Z. Chi, T. Taniguchi, M. Kawaguchi, G. Shibata, N. Kawamura, M. Suzuki, S. Fukami, A. Fujimori, H. Ohno, M. Hayashi, Phys. Rev. Mat. 3 (2019) 104419, https://doi.org/10.1103/PhysRevMaterials.3.104419.
[14] W.-B. Wu, J. Kasiuk, J. Przewoźnik, C. Kapusta, I. Svito, D.T. Tran, H.M. Do, H. M. Dinh, J. Åkerman, T.N.A. Nguyen, Appl. Surf. Sci 648 (2024) 158957, https://doi.org/10.1016/j.apsusc.2023.158957.
[15] A. Hrabec, N.A. Porter, A. Wells, M.J. Benitez, G. Burnell, S. McVitie, D. McGrouther, T.A. Moore, C.H. Marrows, Phys. Rev. B 90 (2014) 020402(R), https://doi.org/10.1103/PhysRevB.90.020402.
[16] K. Di, V.L. Zhang, H.S. Lim, S.C. Ng, M.H. Kuok, J. Yu, J. Yoon, X. Qiu, H. Yang, Phys. Rev. Lett. 114 (2015) 047201, https://doi.org/10.1103/PhysRevLett.114.047201.
[17] M. Belmeguenai, Y. Roussigné, S. Chérif, A. Stashkevich, T. Petrisor, M. Nasui, M. Gabor, J. Phys. D Appl. Phys. 52 (2019) 125002, https://doi.org/10.1088/1361-6463/aafdf5.
[18] A.K. Dhiman, M. Matczak, R. Gieniusz, I. Sveklo, Z. Kurant, U. Guzowska, F. Stobiecki, A. Maziewski, J. Magn. Magn. Mater. 519 (2021) 167485, https://doi.org/10.1016/j.jmmm.2020.167485.
[19] A.G. Kolesnikov, M.E. Stebliy, A.V. Davydenko, A.G. Kozlov, I.S. Osmushko, V. V. Korochentsev, A.V. Ognev, A.V. Gerasimenko, A.V. Sadovnikov, V.A. Gubanov, S.A. Nikitov, X. Wang, C.H. Wan, C. Fang, M. Zhao, X.F. Han, A. Samardak, Appl. Surf. Sci 543 (2021) 148720, https://doi.org/10.1016/j.apsusc.2020.148720.
[20] J. Brandão, D.A. Dugato, M.V. Puydinger dos Santos, F. Béron, J.C. Cezar, Appl. Surf. Sci. 585 (2022) 152598, https://doi.org/10.1016/j.apsusc.2022.152598.
[21] D. Ourdani, Y. Roussigné, S.M. Chérif, M.S. Gabor, M. Belmeguenai, Phys. Rev. B 104 (2021) 104421, https://doi.org/10.1103/PhysRevB.104.104421.
[22] W. Legrand, Y. Sassi, F. Ajejas, S. Collin, L. Bocher, H. Jia, M. Hoffmann, B. Zimmermann, S. Blügel, N. Reyren, V. Cros, A. Thiaville, Phys. Rev. Materials 6 (2022) 024408, https://doi.org/10.1103/PhysRevMaterials.6.024408.
[23] R. Tolley, S.A. Montoya, E.E. Fullerton, Phys. Rev. Materials 2 (2018) 044404, https://doi.org/10.1103/PhysRevMaterials.2.044404.
[24] A.S. Samardak, A.V. Ognev, A.G. Kolesnikov, M.E. Stebliy, V.Y. Samardak, I. G. Iliushin, A.A. Pervishko, D. Yudin, M. Platunov, T. Ono, F. Wilhelm, A. Rogalev, Phys. Chem. Chem. Phys. 24 (2022) 8225, https://doi.org/10.1039/d1cp05456b.
[25] S.K. Jena, R. Islam, E. Milińska, M.M. Jakubowski, R. Minikayev, S. Lewińska, A. Lynnyk, A. Pietruczik, P. Aleszkiewicz, C. Autieri, A. Wawro, Nanoscale 13 (2021) 7685–7693, https://doi.org/10.1039/D0NR08594D.
[26] J. Torrejon, J. Kim, J. Sinha, S. Mitani, M. Hayashi, M. Yamanouchi, H. Ohno, Nat. Commun. 5 (2014) 4655, https://doi.org/10.1038/ncomms5655.
[27] S. Tacchi, R.E. Troncoso, M. Ahlberg, G. Gubbiotti, M. Madami, J. Åkerman, Phys. Rev. Lett. 118 (2017) 147201, https://doi.org/10.1103/PhysRevLett.118.147201.
[28] A.K. Chaurasiya, S. Choudhury, J. Sinha, A. Barman, Phys. Rev. Appl. 9 (2018) 014008, https://doi.org/10.1103/PhysRevApplied.9.014008.
[29] C. Moreau-Luchaire, C. Moutafis, N. Reyren, J. Sampaio, C.A.F. Vaz, N.V. Horne, K. Bouzehouane, K. Garcia, C. Deranlot, P. Warnicke, P. Wohlhüter, J.-M. George, M. Weigand, J. Raabe, V. Cros, A. Fert, Nat. Nanotech. 11 (2016) 444, https://doi.org/10.1038/nnano.2015.313.
[30] D. Weller, A. Carl, R. Savoy, T.C. Huang, M.F. Toney, C. Chappert, J. Phys. Chem. Solids 56 (1995) 1563–1566, https://doi.org/10.1016/0022-3697(95)00129-8.
[31] J. Lucassen, C.F. Schippers, M.A. Verheijen, P. Fritsch, E.J. Geluk, B. Barcones, R. A. Duine, S. Wurmehl, H.J.M. Swagten, B. Koopmans, R. Lavrijsen, Phys. Rev. B 101 (2020) 064432, https://doi.org/10.1103/PhysRevB.101.064432.
[32] G. Patel, F. Ganss, R. Salikhov, S. Stienen, L. Fallarino, R. Ehrler, R.A. Gallardo, O. Hellwig, K. Lenz, J. Lindner, Phys. Rev. B 108 (2023) 184429, https://doi.org/10.1103/PhysRevB.108.184429.
[33] A. Belabbes, G. Bihlmayer, F. Bechstedt, S. Blügel, A. Manchon, Phys. Rev. Lett. 117 (2016) 247202, https://doi.org/10.1103/PhysRevLett.117.247202.
[34] P. Jadaun, L. Register, S. Banerjee, Npj Comput Mater. 6 (2020) 88, https://doi.org/10.1038/s41524-020-00351-1.
[35] E. Simon, L. Rózsa, K. Palotás, L. Szunyogh, Phys. Rev. B 97 (2018) 134405, https://doi.org/10.1103/PhysRevB.97.134405.
[36] A. Fakhredine, A. Wawro, C. Autieri, J. Appl. Phys. 135 (2024) 035303, https://doi.org/10.1063/5.0177260.
[37] S. Paul, S. Heinze, Phys. Rev. B 109 (2024) 064417, https://doi.org/10.1103/PhysRevB.109.064417.
[38] A. Nomura, T. Gao, S. Haku, K. Ando, AIP Advances 12 (2022) 015215, https://doi.org/10.1063/5.0077683.
[39] B. Ojha, S. Mohanty, S. Bedanta, arXiv:2405.05361, (2024), http://arXiv.org/abs/2405.05361.
[40] M.M. Jakubowski, M.O. Liedke, M. Butterling, E. Dynowska, I. Sveklo, E. Milińska, Z. Kurant, R. Böttger, J. von Borany, A. Maziewski, A. Wagner, A. Wawro, J. Phys.: Condens. Matter 31 (2019) 185801, https://doi.org/10.1088/1361-648X/ab0351.
[41] G. Kresse, J. Hafner, Phys. Rev. B 47 (1993) 558, https://doi.org/10.1103/PhysRevB.47.558.
[42] G. Kresse, J. Furthmuller, Phys. Rev. B 54 (1996) 11169, https://doi.org/10.1103/PhysRevB.54.11169.
[43] M.G. Morshed, K.H. Khoo, Y. Quessab, J.-W. Xu, R. Laskowski, P.V. Balachandran, A.D. Kent, A.W. Ghosh, Phys. Rev. B 103 (2021) 174414, https://doi.org/10.1103/PhysRevB.103.174414.
[44] H. Yang, A. Thiaville, S. Rohart, A. Fert, M. Chshiev, Phys. Rev. Lett. 115 (2015) 267210, https://doi.org/10.1103/PhysRevLett.115.267210.
[45] Z. Kurant, S.K. Jena, R. Gieniusz, U. Guzowska, M. Kisielewski, P. Mazalski, I. Sveklo, A. Pietruczik, A. Lynnyk, A. Wawro, A. Maziewski, J. Magn. Magn. Mater. 558 (2022) 169485, https://doi.org/10.1016/j.jmmm.2022.169485.
[46] M. Kisielewski, A. Maziewski, M. Tekielak, A. Wawro, L.T. Baczewski, Phys. Rev. Lett. 89 (2002) 087203, https://doi.org/10.1103/PhysRevLett.89.087203.
[47] W. Dobrogowski, R. Gieniusz, U. Guzowska, Z. Kurant, I. Sveklo, A. Wawro, A. Maziewski, J. Magn. Magn. Mater. 587 (2023) 171339, https://doi.org/10.1016/j.jmmm.2023.171339.
[48] J.A. Brock, E. Fullerton, Adv. Mater. Interfaces 9 (2022) 2101708, https://doi.org/10.1002/admi.202101708.
[49] M. Kisielewski, A. Maziewski, M. Tekielak, J. Ferré, S. Lemerle, V. Mathet, C. Chappert, J. Magn. Magn. Mater. 260 (2003) 231, https://doi.org/10.1016/S0304-8853(02)01333-1.
[50] A.K. Dhiman, T. Dohi, W. Dobrogowski, Z. Kurant, I. Sveklo, S. Fukami, H. Ohno, A. Maziewski, J. Magn. Magn. Mater. 529 (2021) 167699, https://doi.org/10.1016/j.jmmm.2020.167699.
[51] L. Néel, J. Phys. Radium 20 (1959) 215–221, https://doi.org/10.1051/jphysrad:01959002002-3021500.
[52] T.H. Ho, D. Odkhuu, S. Rhim, S. Hong, Current Appl. Phys. 41 (2022) 148–155, https://doi.org/10.1016/j.cap.2022.07.001.
[53] A. Wawro, Z. Kurant, M. Tekielak, P. Nawrocki, E. Milińska, A. Pietruczik, M. Wójcik, P. Mazalski, J. Kanak, K. Ollefs, F. Wilhelm, A. Rogalev, A. Maziewski, J. Phys. D: Appl. Phys. 50 (2017) 215004, https://doi.org/10.1088/1361-6463/a694.
[54] T.Y. Lee, Y. Won, D. Son, S. Lim, S. Lee, I.E.E.E. Magn Lett. 5 (2014) 1000104, https://doi.org/10.1109/LMAG.2014.2321350.
[55] S. Bandiera, R. Sousa, B. Rodmacq, B. Dieny, I.E.E.E. Magn Lett. 2 (2011) 3000504, https://doi.org/10.1109/LMAG.2011.2174032.
[56] P.J. Metaxas, J.P. Jamet, A. Mougin, M. Cormier, J. Ferré, V. Baltz, B. Rodmacq, B. Dieny, R.L. Stamps, Phys. Rev. Lett. 99 (2007) 217208, https://doi.org/10.1103/PhysRevLett.99.217208.
[57] G. Winkler, A. Kobs, A. Chuvilin, D. Lott, A. Schreyer, H.P. Oepen, J. Appl. Phys. 117 (2015) 105306, https://doi.org/10.1063/1.4914039.
[58] M. Kostylev, J. Appl. Phys. 115 (2014) 233902, https://doi.org/10.1063/1.4883181.

[59] J.-H. Moon, S.-M. Seo, K.-J. Lee, K.-W. Kim, J. Ryu, H.-W. Lee, R. McMichael, M. D. Stiles, Phys. Rev. B 88 (2013) 184404, https://doi.org/10.1103/PhysRevB.88.184404.
[60] B. Zimmermann, W. Legrand, D. Maccariello, N. Reyren, V. Cros, S. Blügel, A. Fert, Appl. Phys. Lett. 113 (2018) 232403, https://doi.org/10.1063/1.5049876.
[61] A. Verna, P. Alippi, F. Offi, G. Barucca, G. Varvaro, E. Agostinelli, M. Albrecht, B. Rutkowski, A. Ruocco, D. Paoloni, M. Valvidares, S. Laureti, ACS Appl. Mater. Interfaces 14 (2022) 12766–12776, https://doi.org/10.1021/acsami.1c22341.
[62] R. Chen, Q. Cui, L. Liao, Y. Zhu, R. Zhang, H. Bai, Y. Zhou, G. Xing, F. Pan, H. Yang, C. Song, Nat. Commun. 12 (2021) 3113, https://doi.org/10.1038/s41467-021-23414-3.
[63] K. Shahbazi, J.-V. Kim, H.T. Nembach, J. Shaw, A. Bischof, M.D. Rossell, V. Jeudy, T.A. Moore, C. Marrows, Phys. Rev. B 99 (2019) 094409, https://doi.org/10.1103/PhysRevB.99.094409.
[64] X. Ma, G. Yu, X. Li, T. Wang, D. Wu, K.S. Olsson, Z. Chu, K. An, J.Q. Xiao, K. L. Wang, X. Li, Phys. Rev. B 94 (2016) 180408(R), https://doi.org/10.1103/PhysRevB.94.180408.
[65] D.J. Godbey, G.A. Somorjai, Surface Sci. 202 (1988) 204–226, https://doi.org/10.1016/0039-6028(88)90069-6.
[66] E. Barati, M. Cinal, Phys. Rev. B 95 (2017) 134440, https://doi.org/10.1103/PhysRevB.95.134440.
[67] S. Azzawi, A. Ganguly, M. Tokaç, R.M. Rowan-Robinson, J. Sinha, A.T. Hindmarch, A. Barman, D. Atkinson, Phys. Rev. B 93 (2016) 054402, https://doi.org/10.1103/PhysRevB.93.054402.
[68] E.M. Hankiewicz, G. Vignale, Y. Tserkovnyak, Phys. Rev. B 78 (2008) 020404(R), https://doi.org/10.1103/PhysRevB.78.020404.
[69] M.-H. Nguyen, C.-F. Pai, K.X. Nguyen, D.A. Muller, D.C. Ralph, R.A. Buhrman, Appl. Phys. Lett. 106 (2015) 222402, https://doi.org/10.1063/1.4922084.

CHAPTER 5

ANOMALOUS HALL EFFECT IN WEYL SEMIMETALS

5.1 Overview of the results

The anomalous Hall effect (AHE) is observed in solids without time-reversal symmetry, typically in ferromagnets. It is proportional to the spin-orbit coupling (SOC), therefore, to be sizeable, heavy atom electrons are essential at the Fermi level. In this chapter, we study the anomalous Hall effect in the CeAlSi Weyl semimetal (WSM), however, the AHE can also be induced in other systems exhibiting a non-zero magnetization such as altermagnets which will be discussed in Chapter 6. CeAlSi combines two properties that can lead to the recognition of Weyl nodes, the broken inversion symmetry and the broken time-reversal symmetry which makes it capable of controlling the AHE. The f moments from the Ce^{3+} ion interact with the non-centrosymmetric lattice of this WSM and results in a non-collinear ferromagnetic order [83].
Studying the AHE in a solid requires a deeper understanding of its underlying topology and geometry such as the concept of the Berry curvature[24] which was earlier known as the “anomalous velocity". Electronic structure calculations serve as a very useful tool, especially for establishing a band structure that shows the band crossings and anticrossings near the Fermi level which has been proven capable of inducing a huge AHE[84].
Weyl nodes are topological points that appear as a result of a crossing between two bands with a lifted Kramer’s degeneracy, while they also act as sinks and sources of the Berry curvature. Detecting Weyl nodes specifically close to the Fermi level is known to affect the transverse electronic response such as the AHE by manipulating the direction of the magnetization[85]. We obtained the band structures of CeAlSi for three different configurations depending on the direction of the magnetization using DFT calculations and Wannierization techniques. The band structures showed discrepancies in the position of the Fermi level and the positions of the Weyl points as

well as the band anticrossings at the vicinity of the Fermi level. From the AHE calculations done by a tight-binding approach using Wannier functions, we detected the sign change which is impacted by changing the orientation of the magnetization. In agreement with the experimental findings, the results show an inverted sign of the anomalous Hall conductivity (AHC) between the magnetic system with the magnetization along the a-axis and that along the c-axis. Moreover, a shift detected between the two spikes of the AHC for both systems at the Fermi level was associated with the shift of the Weyl nodes observed in the band structures.
The appearance of Weyl points is magnetically promising for exhibiting complex magnetic structures such as spin spirals[86]. From the three studied magnetic orderings of CeAlSi, we found that the system with non-collinear magnetization displaying spins perpendicular to each other is the ground state. We suspect that in such a case, due to the presence of strong spin-orbit coupling and the broken inversion symmetry, the Dzyaloshinskii Moriya interaction (DMI) must be necessary to stabilize the structure. The DMI was not calculated in this work since it is out of the scope of the experimental observations presented in the paper.
Recently ab-initio calculations have revealed a newly studied WSM, GdAlSi which like CeAlSi, has both properties of broken time-reversal symmetry and broken inversion symmetry[87]. Interestingly enough, this WSM belongs to the family of the *altermagnets*, being a collinear antiferromagnet that exhibits relativistic spin-splitting in the momentum space. Along the paths where GdAlSi indicates a spin splitting, the avoided crossings have large but opposite contributions to the Berry curvature which contributes to the anomalous Hall effect.
My contribution to this paper involved performing DFT calculations to generate the band structure figures and to obtain results for the anomalous Hall effect across the three distinct magnetic configurations of CeAlSi.

5.2 PAPER III: Sign change of anomalous Hall effect and anomalous Nernst effect in the Weyl semimetal CeAlSi

Sign change of anomalous Hall effect and anomalous Nernst effect in the Weyl semimetal CeAlSi

Md Shahin Alam,[1,*] Amar Fakhredine,[2] Mujeeb Ahmad,[1] P. K. Tanwar,[1] Hung-Yu Yang,[3] Fazel Tafti,[3] Giuseppe Cuono,[1] Rajibul Islam,[1] Bahadur Singh,[4] Artem Lynnyk,[2] Carmine Autieri,[1,†] and Marcin Matusiak[1,5,‡]

[1]*International Research Centre MagTop, Institute of Physics, Polish Academy of Sciences, Aleja Lotników 32/46, PL-02668 Warsaw, Poland*

[2]*Institute of Physics, Polish Academy of Sciences, Aleja Lotników 32/46, PL-02668 Warsaw, Poland*

[3]*Department of Physics, Boston College, Chestnut Hill, Massachusetts 02467, USA*

[4]*Department of Condensed Matter Physics and Materials Science, Tata Institute of Fundamental Research, Mumbai 400005, India*

[5]*Institute of Low Temperature and Structure Research, Polish Academy of Sciences, ulica Okólna 2, 50-422 Wrocław, Poland*

(Received 17 October 2022; revised 14 December 2022; accepted 18 January 2023; published 3 February 2023; corrected 1 March 2023)

We report the anomalous Hall effect (AHE) and the anomalous Nernst effect (ANE) data for the noncollinear Weyl semimetal CeAlSi. The anomalous Hall conductivity (σ_{ij}^{A}) was measured for two different orientations of the magnetic field (B), namely σ_{yz}^{A} for $B||a$ and σ_{xy}^{A} for $B||c$, where a and c denote the crystallographic axes. We find that σ_{xy}^{A} and σ_{yz}^{A} are of opposite sign and both are large below the Curie temperature (T_C). In the paramagnetic phase, σ_{xy}^{A} rises even more and goes through a maximum at $T \approx 170$ K, whereas the absolute value of σ_{yz}^{A} decreases with increasing temperature. The origin of the sign difference between σ_{xy}^{A} and σ_{yz}^{A} was attributed to the reconstruction of the band structure under the variation of the spin orientation. Further, in a system where humps in the AHE are present and scalar spin chirality is zero, we show that the **k**-space topology plays an important role to determine the transport properties at both low and high temperatures. We also observed the anomalous contribution in the Nernst conductivity (α_{xy}^{A}) measured for $B||c$. α_{xy}^{A}/T turns out to be sizeable in the magnetic phase and above T_C slowly decreases with temperature. We were able to recreate the temperature dependencies of σ_{xy}^{A} and α_{xy}^{A}/T in the paramagnetic phase using a single band toy model assuming a nonzero Berry curvature in the vicinity of the Weyl node. A decisive factor appears to be a small energy distance between the Fermi level and a Weyl point.

DOI: 10.1103/PhysRevB.107.085102

I. INTRODUCTION

Topological Weyl semimetals (WSMs) are characterized by linear energy dispersions of the valence and conduction bands touching each other in momentum space at Weyl nodes [1–4]. The emergence of massless Weyl fermions as low-energy excitations manifests in many exotic physical effects like the presence of Fermi arcs on the surface [5], chiral anomaly induced negative magnetoresistance [6], chiral zero sound effect [7,8], etc. The subclass of WSMs that also exhibit magnetic ordering is a particularly interesting object of study [9–15]. These materials allow, for example, the manipulation of the anomalous Hall and anomalous Nernst effect [16,17], which is interesting from both scientific and applicative points of view. Recently, huge efforts have been made to investigate the sign change of the anomalous Hall effect (AHE) in Weyl fermions or closely relevant systems as the collinear ferromagnet $SrRuO_3$ [18]. It turns out that many factors, such as the value of the magnetization [19], the presence of the interface which can tune the spin-orbit coupling (SOC), or breaking of the inversion symmetry [20], can change the sign of AHE. Moreover, in the presence of the sign change, the anomalous Hall effect may take values smaller than other features, such as humps in the hysteresis loop of AHE [19,20]. The presence of these humps seems to be particularly favored by a large spin-orbit coupling as well as the absence of inversion symmetry [19,20] and in CeAlSi they were dubbed the loop Hall effect [21]. In CeAlSi, the humps are related to the **k**-space topology [21]. In order to get more insight into the **k**-space topology that governs these humps in CeAlSi, we investigated CeAlSi focusing on the transport properties in magnetic fields and looking for the sign change of the AHE. Additionally, we also measured the anomalous Nernst effect (ANE), whose response to nonzero Berry curvature around the Fermi energy is different than that expected for AHE. In the paramagnetic phase of CeAlSi, the simultaneous temperature evolution of both ANE and AHE can be well described by a simple model assuming the presence of the Weyl node about 20 meV from the Fermi level. The paper is organized as follows: We describe the material and methods in Sec. II; in Sec. III, we present our experimental results; in Sec. IV, we discuss our results, and in Sec. V we summarize our conclusions.

II. MATERIAL AND METHODS

CeAlSi single crystals were grown by a self-flux method using the Canfield crucible sets. The starting materials were weighed in the ratio Ce : Al : Si = 1 : 10 : 1, placed inside a crucible in an evacuated quartz tube, heated to 1000 °C at 3 °C/min, held at 1000 °C for 12 h, cooled to 700 °C at

*shahin@magtop.ifpan.edu.pl
†autieri@magtop.ifpan.edu.pl
‡matusiak@magtop.ifpan.edu.pl

0.1 °C/min, stayed at 700 °C for 12 h, and centrifuged to decant the residual Al flux.

For electrical and thermoelectrical transport measurements a suitable single crystal was cut into a plate with dimensions of $1.4 \times 1.3 \times 0.4$ mm^3 with sides parallel to the natural crystallographic $a \times a \times c$ axes. The electrical and thermal currents were applied along the longest side of the sample (a axis), while the magnetic field (B) was applied parallel to the c axis and perpendicular to the thermal and electrical currents. For electrical measurements with B applied along the crystallographic a axis we selected another single crystal, which was cut into a plate with dimensions of $0.2 \times 2.9 \times 0.6$ mm^3 ($a \times a \times c$). The electrical current (J) was applied along the a axis and B was perpendicular to the current and parallel to another a axis.

For the electrical measurements, the contacts were arranged in the Hall-bar geometry with 25-μm-thick gold wires attached to the sample using DuPont 4929N silver paste. During the measurements of thermoelectric power (S_{xx}) and Nernst signal (S_{yx}) the sample was mounted between two blocks made of phosphor bronze. The temperature difference was determined using two Cernox thermometers and the thermal gradient was implied using a strain gauge as a resistive heater. For selected temperatures, the magnetic field was swept from -14.5 to $+14.5$ T to extract the field voltage components that were antisymmetric and symmetric in B. All the presented data were symmetrized and antisymmetrized for the positive and negative magnetic fields.

Magnetic properties of the sample have been investigated using a Quantum Design Magnetic Property Measurement System MPMS XL equipped with a superconducting quantum interference device. The reciprocating sample option has been chosen to provide a precision of about 10^{-8} emu during the direct current (dc) measurements. A magnetic moment as a function of external dc magnetic field has been measured in the range –7 to +7 T after cooling at zero field. To study the temperature dependencies of susceptibility, alternative current (ac) option has been utilized. An ac field of 1 Oe amplitude and 1 kHz of frequency has been applied during the measurements.

III. RESULTS

The electrical transport properties of CeAlSi were studied for two different orientations of the magnetic field (B), which was applied along the a axis (magnetically easy) or along the c axis (magnetically hard). The temperature (T) dependence of the longitudinal resistivity (ρ_{xx}) for the electrical current (J) parallel to the a axis and $B = 0$ T (see Fig. 1) shows semimetallic behavior with the residual resistivity ratio of 3.2 (see Fig. 1). A kink at $T_C \approx 8.5$ K appears due to the transition from the high-temperature-paramagnetic (PM) phase to the low-temperature ferromagnetic (FM) phase [21]. The value of the transition temperature and overall temperature dependence of ρ_{xx} agree well with the previous reports [21–23]. The magnetic field dependencies of the longitudinal resistivity (ρ_{xx}) and Hall resistivity (ρ_{yx}) ($B||c$ and $J||a$), as well as ρ_{yy} and ρ_{zy} (B and $J||a$, $B\perp J$) are shown in Fig. 2. The Hall resistivities for both orientations of B [Figs. 2(b) and 2(d)] becomes negative at low temperature and high magnetic field,

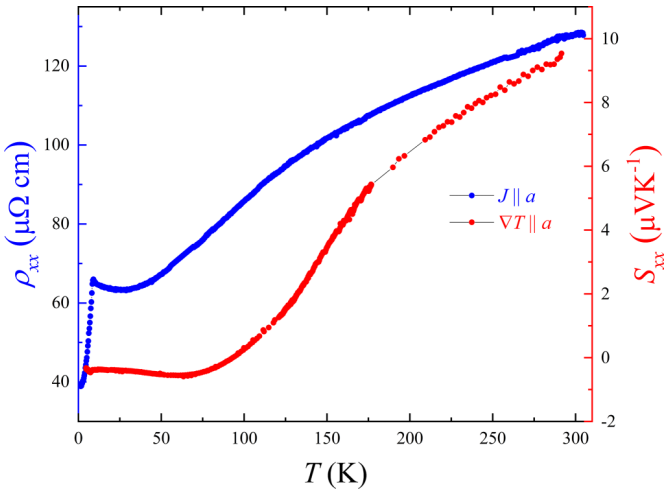

FIG. 1. Temperature dependencies of the zero field resistivity (ρ_{xx}) and the thermoelectric power (S_{xx}) of the noncollinear Weyl semimetal CeAlSi with the current (J) or thermal gradient (∇T) applied parallel to a axis.

which indicates that the electronlike charge carriers dominate electrical transport in this region. Specifically, at $B = 14.5$ T, $\rho_{yx} \approx -35$ $\mu\Omega$ cm for $T \approx 5.4$ K and $\rho_{zy} \approx -65$ $\mu\Omega$ cm for $T \approx 1.7$ K. However, the high-field slope of the ρ_{yx} Hall resistivity evolves with temperature and becomes slightly positive at room temperature ($d\rho_{yx}/dB = 1.2 \times 10^{-9}$ m^{-3} C^{-1} at $T = 301$ K), which might be due to the slowly increasing with temperature role of holes in the electrical transport.

A prominent characteristic of the Hall resistivity in CeAlSi is its nonlinear field dependence [see Fig. 2(b)]. Although this type of behavior might be due to simultaneous contributions from different types of charge carriers [24,25], it seems to be not the case in CeAlSi. In fact, ρ_{yx} varies linearly at high field, but $\rho_{yx}(B)$ does not extrapolate to $\rho_{yx} = 0$ $\mu\Omega$ cm at $B = 0$ T. The field dependence of ρ_{yx} cannot be satisfactorily explained within the two-band model approach as shown in Fig. S1 in the Supplemental Materials (SM) [26] (see also Refs. [27–31] therein), which is in line with the previous reports indicating that the transport in CeAlSi is dominated at low temperatures by a single type of charge carrier [32]. A likely cause for the nonlinear behavior of the Hall resistivity in CeAlSi is a contribution from the anomalous Hall effect (AHE) [21,33–36]. In general, the magnetic field dependencies of Hall resistivity in the presence of the anomalous contribution can be expressed as

$$\rho_{yx} = R_0 B + \rho_{yx}^A, \tag{1}$$

where R_0 is the ordinary Hall coefficient and ρ_{yx}^A is the anomalous Hall resistivity. To determine R_0 and to separate ρ_{yx}^A (or ρ_{zy}^A) from the total Hall resistivity, $\rho_{yx}(B)$ [or $\rho_{zy}(B)$] was fitted with a linear function in the high-field regime (>3 T) [see Figs. 3(a) and 3(b)]. At low temperature, the fitting range of the former was restricted to $B_{\max} = 9$ T, because of a change in the $\rho_{yx}(B)$ slope happening at this field. This anomaly is also visible in the field dependencies of ρ_{xx} [Fig. 2(a)] and it is likely related to the magnetic phase transition caused by increasing magnetic field perpendicular to the initially FM

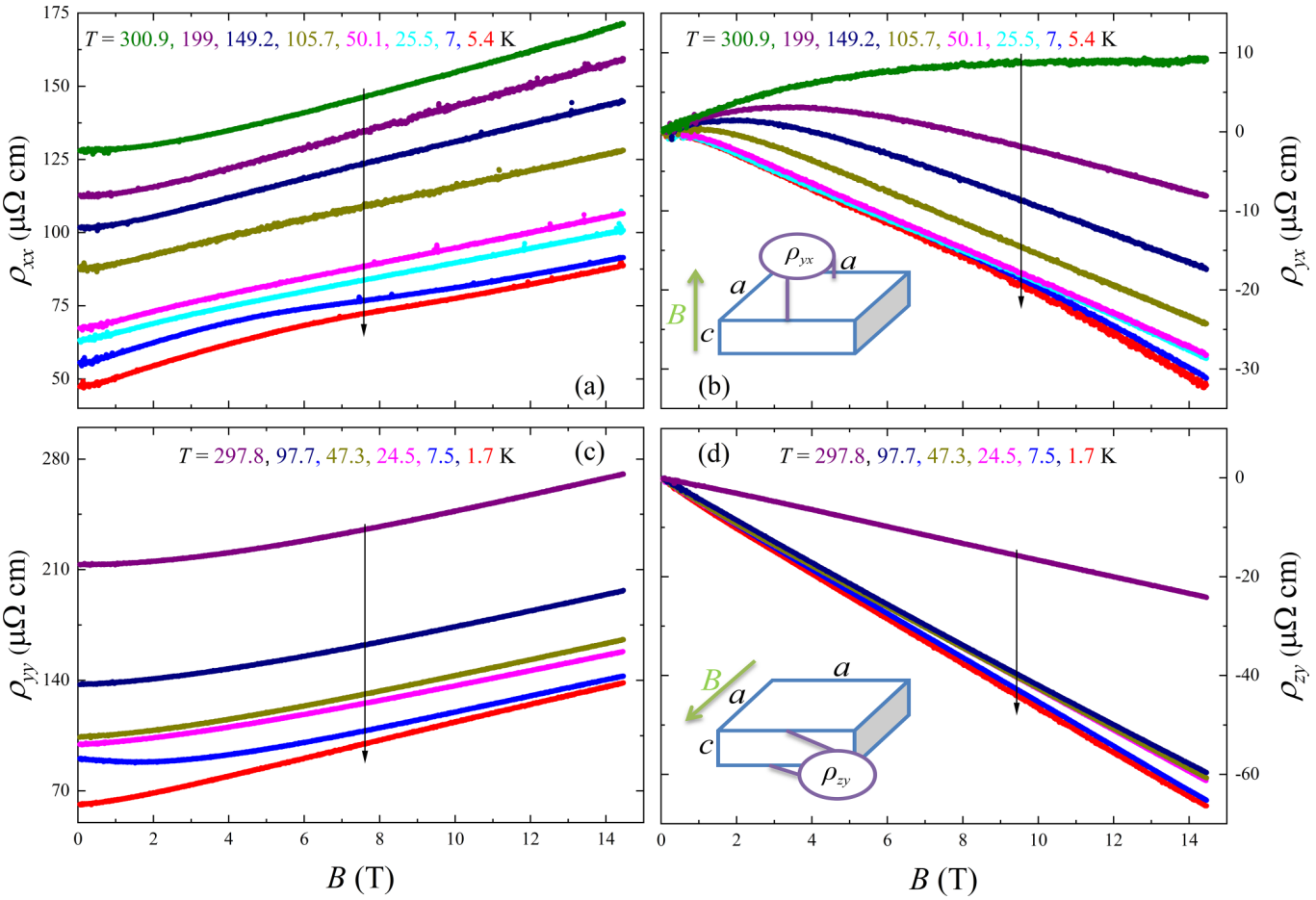

FIG. 2. Magnetic field dependencies of the longitudinal resistivity and Hall resistivity in CeAlSi for two different configurations of the sample. For $J \parallel a$ and $B \parallel c$, (a) longitudinal resistivity (ρ_{xx}); (b) Hall resistivity (ρ_{yx}), $J \parallel a$, $B \parallel a$, and $B \perp J$; (c) longitudinal resistivity (ρ_{yy}); (d) Hall resistivity (ρ_{zy}). The black vertical arrows in all the panels indicate variation of the temperature.

ordered spins [37]. The extracted field dependencies of the anomalous Hall resistivity for $B||c$ (ρ^A_{yx}) and $B||a$ (ρ^A_{zy}) are presented in Figs. 3(c) and 3(d). In the FM phase, both ρ^A_{yx} and ρ^A_{zy} are sizeable, but different in sign and magnitude. In the PM phase, the absolute value of ρ^A_{yx} becomes significantly larger than ρ^A_{zy}.

In general, the AHE can be of intrinsic or extrinsic origin and the latter can be due to the skew-scattering or side-jump processes [27]. If there were a contribution from an extrinsic mechanism, one would expect a specific relation between the resulting anomalous Hall conductivity (AHC, σ^A_{ij}) and the longitudinal conductivity (σ_{ii}). Namely, for the skew scattering, the AHC should follow a linear relationship with the longitudinal conductivity, whereas for the side jump (which is expected to be somewhat smaller [38]) $\sigma^A_{ij} \sim \sigma^2_{ii}$ [39]. In our data we observe neither of them (Fig. S2 in the SM [26]). Furthermore, in topological semimetals with the Fermi level in the vicinity of Weyl nodes, the AHE has been predicted to be predominantly intrinsic and determined by the location of the Weyl points [40,41]. Since CeAlSi has been identified as a Weyl semimetal with Weyl nodes close to the Fermi level [21], one can expect a nonzero AHE due to its nontrivial topological properties [21–23,42]. These are expected to manifest themselves also in other transport phenomena.

The magnetic field dependence of thermoelectric power with the thermal gradient $\nabla T||a$ and $B||c$ is presented in Fig. 4(a). $S_{xx}(B)$ can be satisfactorily fitted with the semiclassical phenomenological model proposed by Liang *et al.* [43]:

$$S_{xx}(B) = S^0_{xx}\frac{1}{1+(\mu B)^2} + S^\infty_{xx}\frac{(\mu B)^2}{1+(\mu B)^2}, \qquad (2)$$

where S^0_{xx} and S^∞_{xx} are the amplitudes of the thermopower at zero and high field limits respectively, and μ is the mobility of charge carriers. A shift of S^0_{xx} from negative at low temperatures to positive at high temperatures can be a sign of an increase in the participation of holes, which is consistent with the Hall resistivity data discussed earlier. If these holes have low mobility, then their contribution will be only slightly field dependent and will not disturb the fitting procedure, which in fact works well for all the data [see Fig. 4(a)]. At low temperatures, we restricted again the fitting field range due to the change in $S_{xx}(B)$ slope at $B \sim 8$–9 T owing to the aforementioned field-induced transition. The temperature dependence of S_{xx} at zero magnetic field is shown in Fig. 1.

Figure 4 presents the field dependencies of the Nernst effect signal measured for a configuration analogous to ρ_{yx}, i.e., $\nabla T \parallel a$ and $B||c$. Results are fitted with the empirical model [44] describing the behavior of the Nernst effect in a

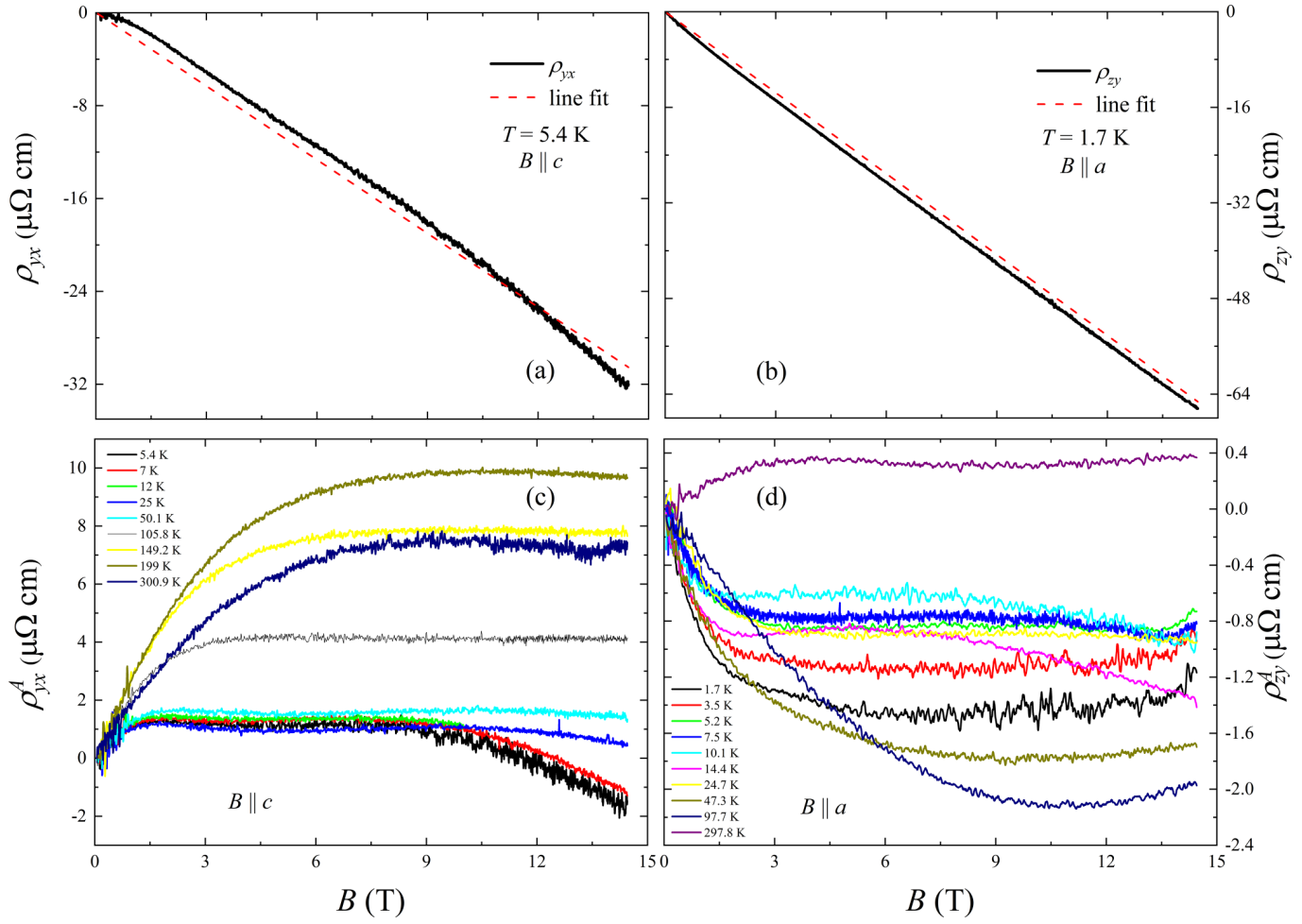

FIG. 3. Magnetic field dependencies of the Hall resistivity in CeAlSi: (a) Hall resistivity (ρ_{yx}) as a function of B at $T = 5.4$ K (black line); (b) Hall resistivity (ρ_{zy}) as a function of B at $T = 1.7$ K (black line). Red dashes lines in (a) and (b) represent the high-field ($B > 3$ T) linear fits. (c) Anomalous contribution to the Hall resistivity (ρ^A_{yx}) extracted from $\rho_{yx}(B)$ for several temperatures. (d) Anomalous contribution to the Hall resistivity (ρ^A_{zy}) extracted from $\rho_{zy}(B)$ for several temperatures.

topologically nontrivial material. Here, the total Nernst signal is similar to the Hall resistivity and is divided into a normal (S^N_{yx}) and an anomalous (S^A_{yx}) part:

$$S_{yx} = S^N_{yx} + S^A_{yx}, \tag{3}$$

where their field dependencies are expressed as

$$S^N_{yx} = S^N_0 \frac{\mu}{1 + (\mu B)^2}, \tag{4}$$

$$S^A_{yx} = S^A_{yx} \tanh(B/B_s), \tag{5}$$

μ is the mobility, and B_s is the saturation field at which the plateau of the anomalous signal is reached. Apparently, the field dependencies of S_{yx} cannot be described only by the conventional Nernst contributions [Eq. (4)] (see Fig. S1 in the SM [26]), but they are very well approximated when the anomalous component [Eq. (5)] is taken into consideration [see Fig. 4(b)]. The temperature dependence of the normalized (divided by temperature) S^A_{yx} is displayed in the inset of Fig. 5(b). In the FM phase S^A_{yx}/T steeply increases with decreasing the temperature (reaching $S^A_{yx} \approx -0.1\ \mu\text{VK}^{-2}$ at 2.5 K), but also in the PM phase there is a nonvanishing anomalous contribution (in the order of $S^A_{yx} \approx -0.02\ \mu\text{VK}^{-2}$) slowly decreasing with temperature.

IV. DISCUSSION

The anomalous Hall (σ^A_{ij}) and transverse thermoelectric (α^A_{ij}) conductivities can be calculated as [45–47]

$$\sigma^A_{ij} = \frac{\rho^A_{ji}}{\rho^2_{ii}}, \tag{6}$$

$$\alpha^A_{ij} = S^A_{ji}\sigma_{ii} - S_{ii}\sigma^A_{ij}, \tag{7}$$

if $\rho_{ii} \gg \rho^A_{ji}$. The resulting temperature dependencies of $\sigma^A_{xy}(T)$ and $\alpha^A_{xy}/T(T)$ are presented in Fig. 5. Two temperature regions can be distinguished: (i) $T < T_C$ (FM phase) and (ii) $T > T_C$ (PM phase).

(i) In the ferromagnetic phase σ^A_{xy} gradually increases with decreasing temperature reaching $\sim 550\ \Omega^{-1}\ \text{cm}^{-1}$ at $T = 5.4$ K [Fig. 5(a)]. The loop Hall effect (LHE) was reported to occur in CeAlSi in the FM phase with $B||c$ field orientation [21], but the appearance of this phenomenon changes from sample to sample depending on a slight off-stoichiometry

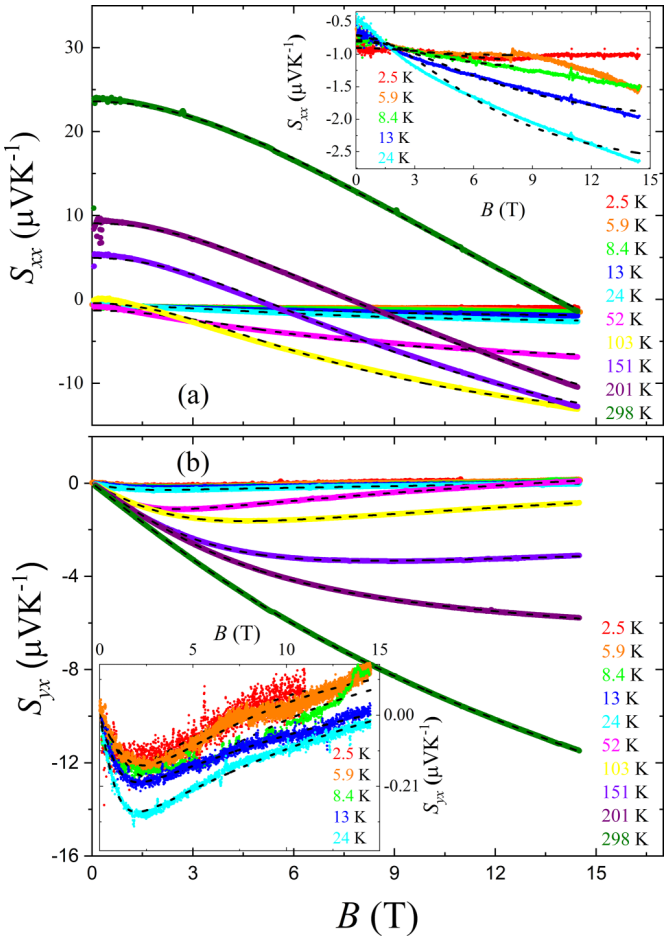

FIG. 4. Magnetic field dependence of the Seebeck (a) and Nernst (b) signal in CeAlSi for various temperatures. Insets show low-temperature field dependencies of the respective coefficients. The black dashed lines in (a) and (b) show fits prepared using Eqs. (2) and (4).

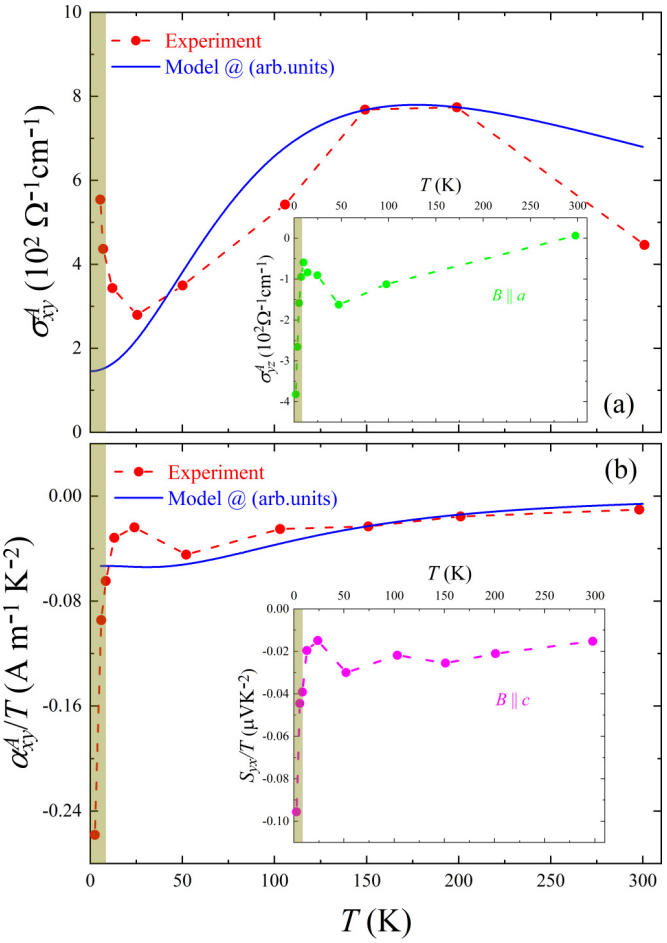

FIG. 5. The temperature dependencies of the anomalous Hall conductivity (σ^A_{xy}) (a) and the anomalous Nernst conductivity (b) for $B||c$ in CeAlSi. Inset in the upper panel shows temperature dependent anomalous conductivity (σ^A_{yz}) for $B||a$; inset in the lower panel presents the temperature dependence of normalized anomalous Nernst effect for $B||c$. Blue solid lines in both panels present the σ^A_{xy} and α^A_{xy}/T T emperature dependencies calculated in arbitrary units using Eqs. (8) and (9). Vertical dark yellow areas in all panels represent the FM regime.

of Si and Al [21]. In this material class, the Weyl nodes are generated due to the lack of inversion symmetry in the noncollinear phase [21,22], while for the ferromagnetic phase Weyl points can be generated also by the breaking of time-reversal symmetry [42]. A recent study on CeAlSi suggested a nontrivial π Berry phase that has been experimentally reported in the FM regime for the magnetic field oriented along the c axis [23].

Similarly to σ^A_{xy}, we also determined the T dependence of σ^A_{yz} for the magnetic field oriented along the easy axis. $\sigma^A_{yz}(T)$ is presented in the inset of Fig. 5(a). We found $\sigma^A_{yz} \approx -380\ \Omega^{-1}\ \mathrm{cm}^{-1}$ at $T = 1.7$ K, a magnitude that is consistent with the previous reports [21]. Differences in values of σ^A_{xy} and σ^A_{yz} can be attributed to the anisotropic electronic structure of CeAlSi, while the observed sign change may be relevant for the detection of topological features in the AHE. Its occurrence, for example, was recently associated with the presence of humplike features in $\rho_{yx}(B)$ [19,48]. A physical origin of this anomaly is under strong debate, but it could derive from topological effects in the k space and/or in the real space. In CeAlSi the appearance of the analogous loop Hall effect appears to be dependent on the position of the Fermi level [21].

We study the magnetic configurations with spins along the a and the c axis (x and z, respectively) in addition to the noncollinear magnetic configuration that is the ground state. Using density functional theory (DFT) and Wannierization techniques, we perform the self-consistent and band structure calculations for different magnetic configurations to investigate the sign change of the AHE in the magnetic phase below $T_C = 8.5$ K.

From the self-consistent calculation, we note that the magnetization is mostly coming from the $4f$ electrons of Ce. The local magnetic moment per Ce atom is approximatively constant in all magnetic configurations. The magnetic moment for the $4f$ orbitals is 0.85–0.89μ_B where the lowest value is for the noncollinear magnetic configuration and the highest is for both collinear configurations. We have an intrinsic magnetic moment from $4f$ orbitals and an induced magnetic moment on the $5d$ orbitals of Ce that is 0.03μ_B within DFT. The f electrons induce a ferromagnetic moment on

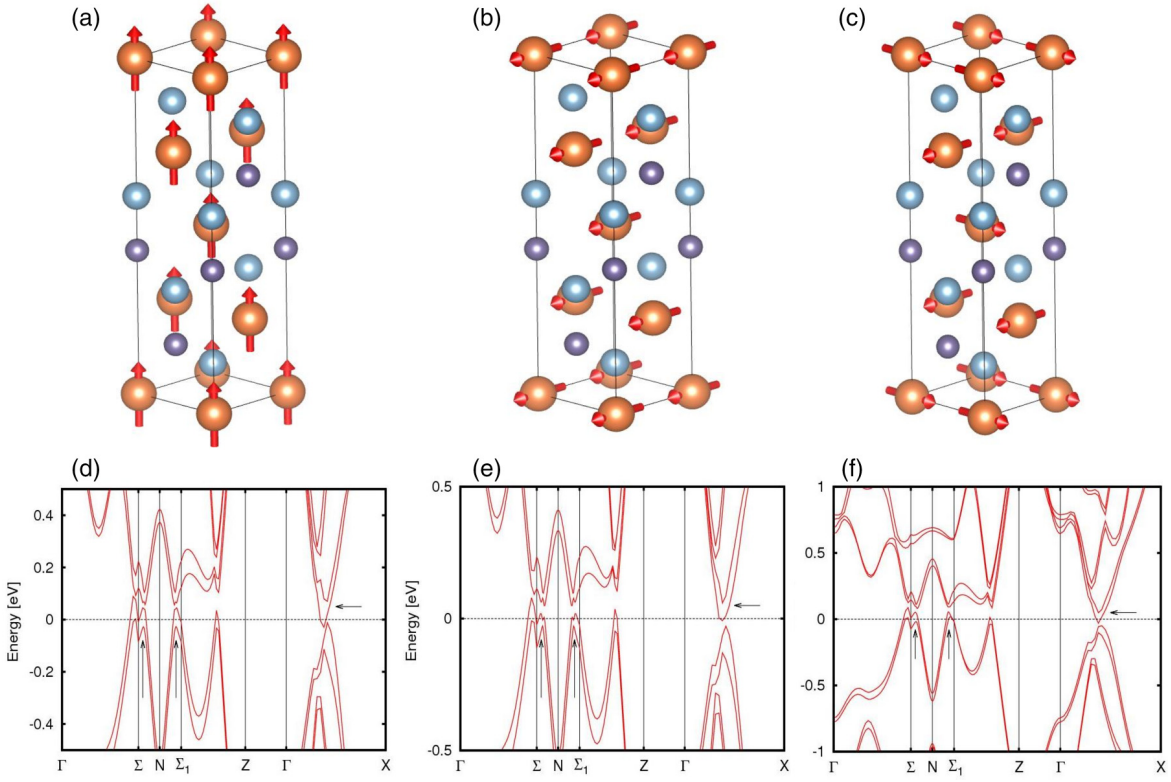

FIG. 6. Magnetic configurations and associated band structures of the CeAlSi Weyl semimetal. (a) Collinear FM order with spins aligned along the a axis. (b) Collinear FM order with spins aligned along the c axis. (c) Noncollinear FM order. (d)–(f) represent the band structure of CeAlSi along the high symmetry paths including spin-orbit coupling in the three mentioned configurations respectively. The vertical arrows represent the band crossings at the Fermi surfaces between **Σ**-**N** and N-$\mathbf{\Sigma_i}$, while the horizontal arrows point at the minimum of the conduction band between **Γ** and **X**.

the d electrons of Ce in the same fashion as happens in the $EuTiO_3/SrTiO_3$ system [49]. The presence of magnetic f electrons far from the Fermi level and d electrons at the Fermi level makes it difficult to produce a simplified tight-binding model containing both d and f orbitals. The bands associated with the Weyl points mainly come from the d electrons of Ce and the sp electrons of Al and Si as clearly visible in the local density of states (see part E in the SM [26]).

We report in Figs. 6(a)–6(c) the magnetic configurations with the Ce spins along the a axis, the c axis, and with the noncollinear configuration, respectively, where a and c are the lattice constants of the conventional unit cell shown in the figure. The band structures associated with these magnetic configurations are in the respective bottom panels in Figs. 6(d)–6(f). The main features of the three band structures are the same, but the different magnetic configurations slightly move the details of the low energy features and switch the position of the Weyl points [50]. One relevant change for the AHE appears along the high-symmetry path **Σ**-**N** and N-$\mathbf{\Sigma_i}$ where we can see at the position of the vertical arrows that the bands close to the Fermi level are slightly lower in energy in the case of the magnetic configuration with spin along the c axis shown in Fig. 6(e); as a consequence the minimum of the conduction band along **ΓX** goes higher in energy in Fig. 6(e). Therefore, the AHE will be modified by an energy shift approximatively equal to the difference between the Weyl points for the case with spin along the c axis (E^{z}_{WP}) and the a axis (E^{x}_{WP}). Defined as $\Delta E_{WP} = E^{z}_{WP} - E^{x}_{WP} > 0$, this shift will be reflected in the AHE calculations. Basically, the different magnetic orderings influence the position of the Fermi level and the energy position of the Weyl points, and the anticrossing points close to the Fermi level.

It is known that close to the high-symmetry line **ΓX** T here are several Weyl points [42]. In CeAlSi, there are Weyl points from the breaking of the inversion symmetry and Weyl points from the breaking of the time-reversal symmetry. The Weyl points from the breaking of the time reversal present along **ΓX** are expected to be more sensitive to the orientation of the magnetic order, therefore strong changes in the AHE are expected.

Given the three band structures in Figs. 6(d)–6(f), we extracted the Wannier tight-binding model (see the SM for details [26]) and calculated the anomalous Hall effect for the three magnetic configurations shown in Fig. 7. We report σ_{xy} for the magnetic configuration with spin along the c axis (hard axis), and σ_{yz} for the configurations with spins along the a axis (easy axis) and the noncollinear phase. In the calculated energy range between -0.5 and 0.5 eV, the calculated AHC is always positive except for a negative spike present for all configurations. While for in-plane magnetic configuration this spike is at the Fermi level, for the out-of-plane magnetic configuration this negative spike is shifted by the quantity ΔE_{WP} deriving from the band structure effects. This implies that the change of the magnetization from the a to the c axis plays a

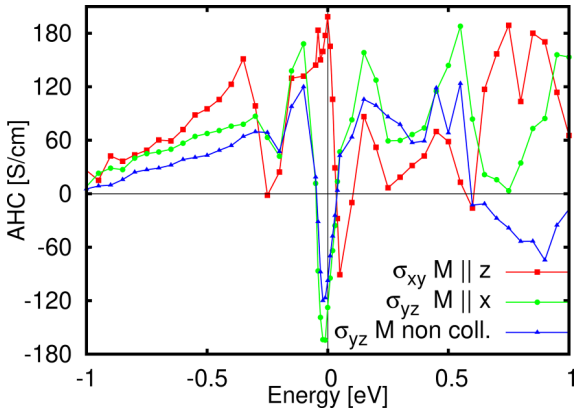

FIG. 7. Calculated intrinsic anomalous Hall conductivity for the collinear ferromagnetic configuration with spins along the a axis (green with circle points), along the c axis (red with square points), and in the noncollinear magnetic configuration (blue with triangle points). The energy range is between -1 and $+1$ eV. The Fermi level is set to zero for all three magnetic configurations.

role in inverting the sign of the anomalous Hall conductivity. The AHC is positive for the out-of-plane magnetic field and negative for the in-plane magnetic field in agreement with the experimental results reported in Fig. 5(a). The presence of consecutive and negative large values of the Berry curvature is a signature of the Weyl points; indeed, in a simplified Weyl points model, the Berry curvature goes from being strongly positive to strongly negative when you go from below to above the Weyl points [51] (see part D of the SM [26]). Hence, the sign change of AHE comes directly from the presence of the **k**-space topology (Weyl points) close to the Fermi level.

Our theoretical results developed at low temperatures could be qualitatively valid also above T_C, where the magnetization rotates from the easy axis towards the axis of the applied strong magnetic field. Since the Weyl points at the Fermi level do not come from $4f$-electron bands, we expect that AHE is weakly dependent if the induced magnetic moment on $5d$ electrons comes from the $4f$-Ce intrinsic magnetic moment or from the external magnetic field. Therefore, the AHE above Curie temperature can be large too and AHE below and above T_C can be of the same order of magnitude. Therefore, the large AHE in the paramagnetic phase emerges due to the presence of the **k**-space topology (Weyl points) close to the Fermi level. Indeed, the Weyl points are close to the Fermi level giving a large contribution even in the presence of the external magnetic field.

(ii) In the paramagnetic phase, the anomalous Hall conductivity for $B||a$ (σ^A_{yz}) decreases with increasing temperature and practically vanishes at room temperature. On the contrary, the anomalous Hall conductivity for $B||c$ (σ^A_{xy}) goes through a maximum at $T \approx 170$ K [see Fig. 5(a)], and reaches higher values than in the FM phase. The corresponding anomalous Nernst conductivity (ANC, α^A_{xy}/T) slowly decreases with increasing temperature [see Fig. 5(b)].

It is worth noting here that a sizeable anomalous response was already reported in other nonmagnetic topological materials [52,53]. The lack of correlation between magnetization and the ANE was even used to indicate that the observed phenomenon is due to nonzero Berry curvature [44]. In topological semimetals the AHE as well as the ANE originate from large Berry curvature generated by Weyl nodes and their presence in the paramagnetic phase of CeAlSi was recently confirmed experimentally [22]. In the presence of a finite Berry curvature, σ^A_{xy} and α^A_{xy} can be calculated as [53,54]

$$\sigma^A_{xy} = \frac{e^2}{\hbar}\sum_n \int \frac{d^3k}{(2\pi)^3}\Omega^n_{xy} f_n, \tag{8}$$

$$\alpha^A_{xy} = -\frac{1}{T}\frac{e}{\hbar}\sum_n \int \frac{d^3k}{(2\pi)^3}\Omega^n_{xy}\Big[(E_n - E_F)f_n + k_B T \ln\left(1 + \exp\frac{(E_n - E_F)}{-k_B T}\right)\Big], \tag{9}$$

where f_n is the Fermi-Dirac distribution, E_F represents the Fermi energy, Ω^n_{xy} is the Berry curvature, and E_n are the eigenenergies for eigenstates n. From the above equations, a general form of ANC and AHC can be written as [51]

$$\lambda_{xy} = \frac{e^2}{\hbar}\sum_n \int \frac{d^3k}{(2\pi)^3}\Omega^n_{xy} w_\lambda(E_n - E_F) \text{ with } \lambda = \sigma, \alpha. \tag{10}$$

Hence, both anomalous conductivities are basically the product of Ω^n_{xy} and weighting factor (w), where the latter reads as [51]

$$w_\sigma(E_n - E_F) = f^T_n(E_n - E_F), \tag{11}$$

$$w_\alpha(E_n - E_F) = -\frac{1}{eT}\Big[(E_n - E_F)f^T_n + k_B T \ln\left(1 + \exp\frac{(E_n - E_F)}{-k_B T}\right)\Big]. \tag{12}$$

Here f^T_n is the Fermi-Dirac distribution function at a given temperature. To model the temperature dependencies of σ^A_{xy} and α^A_{xy} in the PM phase, we introduce a single-band toy model including a nonzero Berry curvature in the vicinity of the Weyl points. $\Omega_{xy}(E)$ is simplistically assumed to change linearly at the Weyl node from positive to negative (see in Fig. S4 in the SM [26]). To match the experimental results, we restricted the energy range of nonzero Ω_{xy} to F $\pm$ 25 meV, which is similar to the range reported in Ref. [51]. As for the energy distance between the Fermi level and a Weyl node, the electronic structure calculations reported by [21] for CeAlSi indicate two sets W_1 and W_2 present close to E_F, which are expected to dominate the low energy physics of this material [21]. Each set contains different Weyl points defined as $W_1^{1,2,3,4}$ and $W_2^{1,2,3,4}$. In our model, the Weyl node is placed at -20 meV away from the E_F, which is consistent with the position of the W_2 nodes [21]. The calculated energy dependencies of AHC, ANC, and w at room temperature are shown in Fig. S4 of the SM [26]. The temperature dependencies of σ^A_{xy} and α^A_{xy}/T calculated using Eqs. (8) and (9) are presented in Fig. 5 as solid lines along with the experimental data. They appear to be governed by a broadening of the Fermi function with temperature, which allows states further away from the E_F to be included in the integration [44,52,53].

Apparently, this crude approach reproduces the characteristics of the experimental data quite well, reflecting

differences between energy dependencies of weighting factors for the anomalous Hall and Nernst effects. Namely, the calculated σ_{xy}^A increases up to $T \approx 170$ K, reaches a maximum, and then decreases, while α_{xy}^A/T slowly decreases with the increasing temperature at a rate similar to the one observed in the experiment. Moreover, the signs of both σ_{xy}^A and α_{xy}^A/T also match the experimental data.

V. CONCLUSION

We studied the anomalous Hall and Nernst effects in the noncollinear Weyl semimetal CeAlSi from room to low temperature. In the ferromagnetic phase, the anomalous Hall conductivity turns out to be positive for the magnetic field applied along the magnetically hard axis ($\sigma_{xy}^A > 0$) and negative for B parallel to the easy axis ($\sigma_{yz}^A < 0$). Density functional theory calculations attributed the different signs of the AHE to a shift of Weyl points along the Γ-X direction and this shift is induced by the reconstructions in the band structure driven by the magnetic configuration. In the paramagnetic phase, σ_{yz}^A significantly decreases, whereas σ_{xy}^A reaches values even higher than at the low-temperature limit. The temperature dependence of σ_{xy}^A as well as the respective Nernst conductivity (α_{xy}^A) can be well approximated using a simple model assuming the presence of a Weyl point in the vicinity of the Fermi level. Properties of the anomalous Hall and Nernst effects appear to be dominated by **k**-space topology at both low and high temperatures.

Note added. After submission of this paper, we became aware of a very recent work that also reports on the anomalous Hall and Nernst effect in CeAlSi [55].

ACKNOWLEDGMENTS

We acknowledge W. Brzezicki, R. Citro, and K. Das for the useful discussions. This work was supported by the Foundation for Polish Science through the International Research Agendas program cofinanced by the European Union within the Smart Growth Operational Programme. A.F. was supported by the Polish National Science Centre under Project No. 2020/37/B/ST5/02299. We also acknowledge the access to the computing facilities of the Interdisciplinary Center of Modeling at the University of Warsaw, Grants No. G84-0, No. GB84-1, and No. GB84-7. We acknowledge the CINECA award under the ISCRA initiative IsC93 "RATIO" and IsC99 "SILENTS" grants for the availability of high-performance computing resources and support. The work at Boston College was funded by the National Science Foundation under Award No. DMR-2203512.

[1] N. P. Armitage, E. J. Mele, and A. Vishwanath, Weyl and Dirac semimetals in three-dimensional solids, Rev. Mod. Phys. **90**, 015001 (2018).

[2] B. Yan and C. Felser, Topological materials: Weyl semimetals, Annu. Rev. Condens. Matter Phys. **8**, 337 (2017).

[3] R. Islam, B. Ghosh, G. Cuono, A. Lau, W. Brzezicki, A. Bansil, A. Agarwal, B. Singh, T. Dietl, and C. Autieri, Topological states in superlattices of HgTe class of materials for engineering three-dimensional flat bands, Phys. Rev. Research **4**, 023114 (2022).

[4] A. S. Wadge, B. J. Kowalski, C. Autieri, P. Iwanowski, A. Hruban, N. Olszowska, M. Rosmus, J. Kołodziej, and A. Wiśniewski, Topological Lifshitz transition in Weyl semimetal NbP decorated with heavy elements, Phys. Rev. B **105**, 235304 (2022).

[5] X. Wan, A. M. Turner, A. Vishwanath, and S. Y. Savrasov, Topological semimetal and Fermi-arc surface states in the electronic structure of pyrochlore iridates, Phys. Rev. B **83**, 205101 (2011).

[6] X. Huang, L. Zhao, Y. Long, P. Wang, D. Chen, Z. Yang, H. Liang, M. Xue, H. Weng, Z. Fang, X. Dai, and G. Chen, Observation of the Chiral-Anomaly-Induced Negative Magnetoresistance: In 3D Weyl Semimetal TaAs, Phys. Rev. X **5**, 031023 (2015).

[7] J. Xiang, S. Hu, Z. Song, M. Lv, J. Zhang, L. Zhao, W. Li, Z. Chen, S. Zhang, J. T. Wang, Y. F. Yang, X. Dai, F. Steglich, G. Chen, and P. Sun, Giant Magnetic Quantum Oscillations in the Thermal Conductivity of TaAs: Indications of Chiral Zero Sound, Phys. Rev. X **9**, 031036 (2019).

[8] P. K. Tanwar, M. S. Alam, M. Ahmad, D. Kaczorowski, and M. Matusiak, Severe violation of the Wiedemann-Franz law in quantum oscillations of NbP, Phys. Rev. B **106**, L041106 (2022).

[9] I. Belopolski, K. Manna, D. S. Sanchez, G. Chang, B. Ernst, J. Yin, S. S. Zhang, T. Cochran, N. Shumiya, H. Zheng, B. Singh, G. Bian, D. Multer, M. Litskevich, X. Zhou, S. M. Huang, B. Wang, T. R. Chang, S. Y. Xu, A. Bansil *et al.*, Discovery of topological Weyl fermion lines and drumhead surface states in a room temperature magnet, Science **365**, 1278 (2019).

[10] K. Kim, J. Seo, E. Lee, K. T. Ko, B. S. Kim, B. G. Jang, J. M. Ok, J. Lee, Y. J. Jo, W. Kang, J. H. Shim, C. Kim, H. W. Yeom, B. Il Min, B. J. Yang, and J. S. Kim, Large anomalous Hall current induced by topological nodal lines in a ferromagnetic van der Waals semimetal, Nat. Mater. **17**, 794 (2018).

[11] H. B. Noam Morali, R. Batabyal, P. K. Nag, E. Liu, Q. Xu, Y. Sun, B. Yan, C. Felser, and N. Avraham, Fermi-arc diversity on surface terminations of the magnetic Weyl semimetal $Co_3Sn_2S_2$, Science **365**, 1286 (2019).

[12] E. Liu, Y. Sun, N. Kumar, L. Muechler, A. Sun, L. Jiao, S. Y. Yang, D. Liu, A. Liang, Q. Xu, J. Kroder, V. Süß, H. Borrmann, C. Shekhar, Z. Wang, C. Xi, W. Wang, W. Schnelle, S. Wirth, Y. Chen, S. T. B. Goennenwein, and C. Felser, Giant anomalous Hall effect in a ferromagnetic kagome-lattice semimetal, Nat. Phys. **14**, 1125 (2018).

[13] Y. Yao, L. Kleinman, A. H. MacDonald, J. Sinova, T. Jungwirth, D. sheng Wang, E. Wang, and Q. Niu, First Principles Calculation of Anomalous Hall Conductivity in Ferromagnetic bcc Fe, Phys. Rev. Lett. **92**, 037204 (2004).

[14] J. Gaudet, H. Y. Yang, S. Baidya, B. Lu, G. Xu, Y. Zhao, J. A. Rodriguez-Rivera, C. M. Hoffmann, D. E. Graf, D. H. Torchinsky, P. Nikolić, D. Vanderbilt, F. Tafti, and

C. L. Broholm, Weyl-mediated helical magnetism in NdAlSi, Nat. Mater. **20**, 1650 (2021).

[15] R. Yang and M. Corasaniti, Charge dynamics of a noncentrosymmetric magnetic Weyl semimetal, npj Quantum Mater. **7**, 101 (2022).

[16] P. Li, J. Koo, W. Ning, J. Li, L. Miao, L. Min, Y. Zhu, Y. Wang, N. Alem, C. X. Liu, Z. Mao, and B. Yan, Giant room temperature anomalous Hall effect and tunable topology in a ferromagnetic topological semimetal Co_2MnAl, Nat. Commun. **11**, 3476 (2020).

[17] K. Geishendorf, P. Vir, C. Shekhar, C. Felser, J. I. Facio, J. Van Den Brink, K. Nielsch, A. Thomas, and S. T. B. Goennenwein, Signatures of the magnetic entropy in the thermopower signals in nanoribbons of the magnetic Weyl semimetal $Co_3Sn_2S_2$, Nano Lett. **20**, 300 (2020).

[18] S. Itoh, Y. Endoh, T. Yokoo, S. Ibuka, J. G. Park, Y. Kaneko, K. S. Takahashi, Y. Tokura, and N. Nagaosa, Weyl fermions and spin dynamics of metallic ferromagnet $SrRuO_3$, Nat. Commun. **7**, 11788 (2016).

[19] D. J. Groenendijk, C. Autieri, T. C. Van Thiel, W. Brzezicki, J. R. Hortensius, D. Afanasiev, N. Gauquelin, P. Barone, K. H. W. Van Den Bos, S. Van Aert, J. Verbeeck, A. Filippetti, S. Picozzi, M. Cuoco, and A. D. Caviglia, Berry phase engineering at oxide interfaces, Phys. Rev. Res. **2**, 023404 (2020).

[20] T. C. Van Thiel, W. Brzezicki, C. Autieri, J. R. Hortensius, D. Afanasiev, N. Gauquelin, D. Jannis, N. Janssen, D. J. Groenendijk, J. Fatermans, S. Van Aert, J. Verbeeck, M. Cuoco, and A. D. Caviglia, Coupling Charge and Topological Reconstructions at Polar Oxide Interfaces, Phys. Rev. Lett. **127**, 127202 (2021).

[21] H. Y. Yang, B. Singh, J. Gaudet, B. Lu, C. Y. Huang, W. C. Chiu, S. M. Huang, B. Wang, F. Bahrami, B. Xu, J. Franklin, I. Sochnikov, D. E. Graf, G. Xu, Y. Zhao, C. M. Hoffman, H. Lin, D. H. Torchinsky, C. L. Broholm, A. Bansil, and F. Tafti, Noncollinear ferromagnetic Weyl semimetal with anisotropic anomalous Hall effect, Phys. Rev. B **103**, 115143 (2021).

[22] A. P. Sakhya, C. Huang, G. Dhakal, X. Gao, S. Regmi, X. Yao, R. Smith, M. Sprague, and B. Singh, Observation of Fermi arcs and Weyl nodes in a non-centrosymmetric magnetic Weyl semimetal, arXiv:2203.05440.

[23] M. M. Piva, J. C. Souza, V. Brousseau-Couture, K. R. Pakuszewski, J. K. John, C. Adriano, M. Côté, P. G. Pagliuso, and M. Nicklas, Tuning the nontrivial topological properties of the Weyl semimetal CeAlSi, arXiv:2111.05742.

[24] C. M. Hurd, *The Hall Effect in Metals and Alloys*, International Cryogenics Monograph Series (Springer, Berlin, 1972).

[25] M. S. Alam, P. K. Tanwar, K. Dybko, A. S. Wadge, P. Iwanowski, A. Wiśniewski, and M. Matusiak, Temperature-driven spin-zero effect in $TaAs_2$, J. Phys. Chem. Solids **170**, 110939 (2022).

[26] See Supplemental Material at http://link.aps.org/supplemental/10.1103/PhysRevB.107.085102 for additional experimental data, modeled anomalous Hall and Nernst conductivities in the presence of nonzero Berry curvature, and a detailed discussion of band structure calculations.

[27] G. Kresse and J. Hafner, *Ab initio* molecular dynamics for liquid metals, Phys. Rev. B **47**, 558 (1993).

[28] G. Kresse and J. Furthmüller, Efficient iterative schemes for ab initio total-energy calculations using a plane-wave basis set, Phys. Rev. B **54**, 11169 (1996).

[29] W. E. Pickett, Implementation of the LDA + U method using the full-potential linearized augmented plane-wave basis, Phys. Rev. B **60**, 10763 (1999).

[30] A. A. Mostofi, J. R. Yates, G. Pizzi, Y. S. Lee, I. Souza, D. Vanderbilt, and N. Marzari, An updated version of WANNIER90: A tool for obtaining maximally-localised wannier functions, Comput. Phys. Commun. **185**, 2309 (2014).

[31] M. Zeer, D. Go, J. P. Carbone, T. G. Saunderson, M. Redies, M. Kläui, J. Ghabboun, W. Wulfhekel, S. Blügel, and Y. Mokrousov, Spin and orbital transport in rare-earth dichalcogenides: The case of EuS_2, Phys. Rev. Mater. **6**, 074004 (2022).

[32] W. Cao, Y. Su, Q. Wang, C. Pei, L. Gao, Y. Zhao, C. Li, N. Yu, J. Wang, Z. Liu, Y. Chen, G. Li, J. Li, and Y. Qi, Quantum oscillations in noncentrosymmetric Weyl semimetal SmAlSi, Chin. Phys. Lett. **39**, 047501 (2022).

[33] N. Nagaosa, J. Sinova, S. Onoda, A. H. MacDonald, and N. P. Ong, Anomalous Hall effect, Rev. Mod. Phys. **82**, 1539 (2010).

[34] K. S. Takahashi, H. Ishizuka, T. Murata, Q. Y. Wang, Y. Tokura, N. Nagaosa, and M. Kawasaki, Anomalous Hall effect derived from multiple Weyl nodes in high-mobility $EuTiO_3$ films, Sci. Adv. **4**, eaar7880 (2018).

[35] M. Tanaka, Y. Fujishiro, M. Mogi, Y. Kaneko, T. Yokosawa, N. Kanazawa, S. Minami, T. Koretsune, R. Arita, S. Tarucha, M. Yamamoto, and Y. Tokura, Topological kagome magnet $Co_3Sn_2S_2$ thin flakes with high electron mobility and large anomalous Hall effect, Nano Lett. **20**, 7476 (2020).

[36] B. Meng, H. Wu, Y. Qiu, C. Wang, Y. Liu, Z. Xia, S. Yuan, H. Chang, and Z. Tian, Large anomalous Hall effect in ferromagnetic Weyl semimetal candidate PrAlGe, APL Mater. **7**, 051110 (2019).

[37] J. F. Wang, Q. X. Dong, Z. P. Guo, M. Lv, Y. F. Huang, J. Sen Xiang, Z. A. Ren, Z. J. Wang, P. J. Sun, G. Li, and G. F. Chen, NdAlSi: A magnetic Weyl semimetal candidate with rich magnetic phases and atypical transport properties, Phys. Rev. B **105**, 144435 (2022).

[38] S. Onoda, N. Sugimoto, and N. Nagaosa, Intrinsic versus Extrinsic Anomalous Hall Effect in Ferromagnets, Phys. Rev. Lett. **97**, 126602 (2006).

[39] L. Berger, Side-jump mechanism for the Hall effect of ferromagnets, Phys. Rev. B **2**, 4559 (1970).

[40] A. A. Burkov, Anomalous Hall Effect in Weyl Metals, Phys. Rev. Lett. **113**, 187202 (2014).

[41] A. Sekine, D. Culcer, and A. H. MacDonald, Quantum kinetic theory of the chiral anomaly, Phys. Rev. B **96**, 235134 (2017).

[42] G. Chang, B. Singh, S. Y. Xu, G. Bian, S. M. Huang, C. H. Hsu, I. Belopolski, N. Alidoust, D. S. Sanchez, H. Zheng, H. Lu, X. Zhang, Y. Bian, T. R. Chang, H. T. Jeng, A. Bansil, H. Hsu, S. Jia, T. Neupert, H. Lin, and M. Z. Hasan, Magnetic and noncentrosymmetric Weyl fermion semimetals in the RAlGe family of compounds (R = Rare Earth), Phys. Rev. B **97**, 041104(R) (2018).

[43] T. Liang, Q. Gibson, J. Xiong, M. Hirschberger, S. P. Koduvayur, R. J. Cava, and N. P. Ong, Evidence for massive bulk Dirac fermions in $Pb_{1-x}Sn_xSe$ from Nernst and thermopower experiments, Nat. Commun. **4**, 2696 (2013).

[44] T. Liang, J. Lin, Q. Gibson, T. Gao, M. Hirschberger, M. Liu, R. J. Cava, and N. P. Ong, Anomalous Nernst Effect in the Dirac Semimetal Cd_3As_2, Phys. Rev. Lett. **118**, 136601 (2017).

[45] J. Hu, B. Ernst, S. Tu, M. KuveŽdić, A. Hamzić, E. Tafra, M. Basletić, Y. Zhang, A. Markou, C. Felser, A. Fert, W. Zhao,

J. P. Ansermet, and H. Yu, Anomalous Hall and Nernst Effects in Co_2TiSn and $Co_2Ti_{0.6}V_{0.4}Sn$ Heusler Thin Films, Phys. Rev. Appl. **10**, 044037 (2018).

[46] Y. Pu, D. Chiba, F. Matsukura, H. Ohno, and J. Shi, Mott Relation for Anomalous Hall and Nernst Effects in $Ga_{1-x}Mn_xAs$ Ferromagnetic Semiconductors, Phys. Rev. Lett. **101**, 117208 (2008).

[47] D. Xiao, Y. Yao, Z. Fang, and Q. Niu, Berry-Phase Effect in Anomalous Thermoelectric Transport, Phys. Rev. Lett. **97**, 026603 (2006).

[48] A. K. Nayak, J. E. Fischer, Y. Sun, B. Yan, J. Karel, A. C. Komarek, C. Shekhar, N. Kumar, W. Schnelle, J. Kübler, C. Felser, and S. S. P. Parkin, Large anomalous Hall effect driven by a nonvanishing berry curvature in the noncolinear antiferromagnet Mn_3Ge, Sci. Adv. **2**, e1501870 (2016).

[49] R. Di Capua, M. Verma, M. Radovic, V. N. Strocov, C. Piamonteze, E. B. Guedes, N. C. Plumb, Y. Chen, M. D'Antuono, G. M. De Luca, E. Di Gennaro, D. Stornaiuolo, D. Preziosi, B. Jouault, F. Miletto Granozio, A. Sambri, R. Pentcheva, G. Ghiringhelli, and M. Salluzzo, Orbital selective switching of ferromagnetism in an oxide quasi two-dimensional electron gas, npj Quantum Mater. **7**, 41 (2022).

[50] M. Yao, H. Lee, N. Xu, Y. Wang, J. Ma, O. V. Yazyev, Y. Xiong, M. Shi, G. Aeppli, and Y. Soh, Switchable Weyl nodes in topological kagome ferromagnet Fe_3Sn_2, arXiv:1810.01514.

[51] J. Noky, J. Gooth, C. Felser, and Y. Sun, Characterization of topological band structures away from the Fermi level by the anomalous Nernst effect, Phys. Rev. B **98**, 241106(R) (2018).

[52] T. Liang, J. Lin, Q. Gibson, S. Kushwaha, M. Liu, W. Wang, H. Xiong, J. A. Sobota, M. Hashimoto, P. S. Kirchmann, Z. X. Shen, R. J. Cava, and N. P. Ong, Anomalous Hall effect in $ZrTe_5$, Nat. Phys. **14**, 451 (2018).

[53] F. Caglieris, C. Wuttke, S. Sykora, V. Süss, C. Shekhar, C. Felser, B. Büchner, and C. Hess, Anomalous Nernst effect and field-induced Lifshitz transition in the Weyl semimetals TaP and TaAs, Phys. Rev. B **98**, 201107(R) (2018).

[54] D. Xiao, M. C. Chang, and Q. Niu, Berry phase effects on electronic properties, Rev. Mod. Phys. **82**, 1959 (2010).

[55] E. Cheng, L. Yan, X. Shi, M. Behnami, J. Yuan, Y. Xu, Y. Xu, Y. Wan, W. Xia, N. Pavlovskii, D. C. Peets, W. Zhao, Y. Guo, S. Li, W. Yang, and B. Büchner, Anomalous transverse transport and phase transitions in Weyl semimetals RAlSi (R = La, Ce), arXiv:2301.03800.

Correction: The units shown on the *y* axis of the previously published Figure 5(b) were incorrect. The figure has been replaced.

CHAPTER 6

ALTERMAGNETISM

6.1 Overview of the results

Altermagnetic compounds have been the subject of attention recently due to the emerging properties they exhibit. They incorporate characteristics of a spin-split band structure due to a broken time-reversal symmetry which occurs typically in ferromagnets, and a zero net magnetization due to anti-parallel spin ordering which is an aspect of antiferromagnetism[7, 8]. Research on altermagnets showing the lifting of Kramer's degeneracy has proved the advantage of compounds with compensated magnetization over ferromagnets, especially in spintronics after they have been excluded from the field for a long time. The disadvantage in ferromagnets, demonstrated in their weak resistance to external magnetic fields, is no longer a challenge in the case of zero-magnetization compounds showing alternating spin polarization with a broken time-reversal symmetry. In antiferromagnetic systems, where Kramer's degeneracy is preserved even in the presence of spin-orbit coupling (SOC), it was believed that responses to the time-reversal symmetry breaking such as the anomalous Hall effect (AHE), due to zero net magnetization, would not occur. This was contradicted by the unfolding phenomenon of altermagnetism (AM). Several studies were done on antiferromagnets such as RuO_2 and MnTe [88, 89] where the AHE effect was observed in the absence of an external field and the presence of a vanishing net magnetization and where the time-reversal symmetry is broken in a specific unconventional phase that arises due to the crystal environment of the magnetic atoms. Altermagnets have magnetization densities that obey the non-relativistic spin symmetry combining a two-fold spin-space rotation with a real-space rotation which are known by proper or improper and symmorphic or non-symmorphic symmetries. In addition to the absence of the non-relativistic global dipole magnetization, these magnetization densities do not have to contain even the local

dipole moments.
The combinations of point group operations with nonprimitive lattice translations, that are dubbed nonsymmorphic symmetries, can lead to new topological phases[90]. These kinds of symmetries impose global topological constraints on the band structure of a system which leads to additional crossings/anticrossings of bands near the Fermi level. There the Berry curvature has the highest contributions and may reveal novel topological response phenomena and unique magnetotransport properties[91].
CrAs belongs to the Pnma family and hosts nonsymmorphic symmetries[92] which results in many special band structure characteristics, such as the emergence of semi-Dirac points which are points having a linear dispersion along only one direction in the k-space[93, 94]. The presence of the non-magnetic atoms (As) in the crystal structure of CrAs is involved in breaking the inversion symmetry and the translation symmetry which connects the two sublattices of opposite directions. Consequently, the time-reversal symmetry was broken which was revealed by the spin splitting in the band structure of the C-type CrAs. The interplay between these two properties appearing at certain time-reversal invariant momenta (TRIM) points reveals interesting changes demonstrated by degeneracies at the edges of the Brillouin zone and the appearance of semi-Dirac points. In the non-magnetic phase, where the Kramer's degeneracy is protected, we show the network of the bands crossing and others avoiding each other in the band structure of the C-type CrAs. Upon the inclusion of SOC, we show that the magnetic space group can change depending on the direction of the Néel vector which causes a selective removal of the spin degeneracy. The band crossings and anti-crossings are generally further split by the effect of SOC when the orientation of the Néel vector is modified except at one point which could be a nodal line protected by the glide operator upon directing the Néel vector along x. The appearance of semi-Dirac points leads to several avoided band crossings which contribute to the Berry curvature and in turn enhance electronic transport properties such as the AHE which was confirmed and calculated using the Wannierization technique.
My contribution to this work has been related to performing and analyzing the theoretical calculations and producing all the figures except those related to the anomalous Hall conductivity.

6.2 PAPER IV: Interplay between altermagnetism and nonsymmorphic symmetries generating large anomalous Hall conductivity by semi-Dirac points induced anticrossings

Interplay between altermagnetism and nonsymmorphic symmetries generating large anomalous Hall conductivity by semi-Dirac points induced anticrossings

Amar Fakhredine [1,2] Raghottam M. Sattigeri,[2] Giuseppe Cuono [2,*] and Carmine Autieri [2]
[1]*Institute of Physics, Polish Academy of Sciences, Aleja Lotników 32/46, PL-02668 Warsaw, Poland*
[2]*International Research Centre Magtop, Institute of Physics, Polish Academy of Sciences, Aleja Lotników 32/46, PL-02668 Warsaw, Poland*

(Received 12 June 2023; revised 8 September 2023; accepted 8 September 2023; published 19 September 2023)

We investigate the interplay between altermagnetic spin-splitting and nonsymmorphic symmetries using the space group No. 62 as a testbed. Studying different magnetic orders by means of first-principles calculations, we find that the altermagnetism (AM) is present in the *C*-type magnetic configuration while it is absent for the *G*-type and *A*-type configurations due to different magnetic space group types. The nonsymmorphic symmetries constrain the system to a fourfold degeneracy at the border of the Brillouin zone with semi-Dirac dispersion. In the case of large hybridization as for transition metal pnictides, the interplay between AM and nonsymmorphic symmetries generates an intricate network of several crossings and anticrossings that we describe in terms of semi-Dirac points and glide symmetries. When we add the spin-orbit coupling (SOC), we find a Néel-vector dependent spin-orbit splitting at the time-reversal invariant momenta points since the magnetic space groups depend on the Néel vector. The magnetic space group type I produces antiferromagnetic hourglass electrons that disappear in the type III. When the Néel vector is along x, we observe a glide-protected crossing that could generate a nodal line in the altermagnetic phase. The SOC splits the remaining band crossings and band anticrossings, producing a large anomalous Hall effect in all directions excluding the Néel-vector direction.

DOI: 10.1103/PhysRevB.108.115138

I. INTRODUCTION

Until a few years ago, the two collinear magnetic phases were known in condensed matter physics as ferromagnetism and antiferromagnetism, displaying completely different properties. Very recently, a new variant of the collinear antiferromagnetism was discovered called altermagnetism (AM), or collinear antiferromagnets with noninterconvertible spin-structure motif pair [1–6], which hosts both properties of the ferromagnets and usual antiferromagnets. Unlike ferromagnetism, where the crystal has a net magnetization and there is time-reversal symmetry (TRS) breaking, and unlike antiferromagnetism, where the total magnetization is zero, altermagnetism hosts systems in which the magnetization in the real space is zero but there is breaking of the spin degeneracy in the reciprocal space like in ferromagnetic compounds. The condition to observe the AM is the absence of a translation, an inversion, or a combination of both that maps the spin-up charge to the spin-down charge. In this case, only a rototranslation or mirror can map the spin-up charge in the spin-down charge. From the point of view of group theory, the altermagnetic compounds must belong to type-I and type-III magnetic space groups (MSG) [7]. The type-I MSGs are crystallographic space groups without any additional symmetry while the type-III are crystallographic space groups with additional antisymmetry versions of half of the symmetry operations [8].

The altermagnetic systems exhibit nonrelativistic spin splitting and may produce anomalous Hall effect (AHE) [9,10] once the relativistic effects are included. The AHE is enhanced by avoided crossings, also called anticrossings. While further investigations should be made in order to assure the possession of AHE, AM can produce an AHE along the direction of the Hall vector, but a very limited number of altermagnetic systems are metallic. Regarding technological applications, altermagnets could be assumed as a leading role in realizing concepts in spincaloritronics [11]. They can be also used in Josephson junctions [12], room-temperature magnetoresistance in an all-antiferromagnetic tunnel junction [13], and to generate neutral currents for spintronics [14].

One of the space groups in which the altermagnetic phase was established is the Pnma space group [7]. In a recent work, a new route to search altermagnetic states was introduced and it was taken into consideration the example of the Pnma perovskites [15]; it was shown that distinctive signatures on the band structure emerge from the angular variation of magnetization components in altermagnets. These signatures manifest as protected nodal lines along mirror planes of the crystal structure and pinch points on the Fermi surface, which act akin to type-II Weyl nodes [15]. The Pnma presents several nonsymmorphic symmetries [16–18], which are a composition of fractional lattice translations with point-group operations, like mirror reflection (glide plane) or rotation (screw axis). The glide symmetry or glide reflection symmetry is a symmetry operation that consists of a combination of a mirror reflection with respect to a plane and then a translation parallel to that plane. The eigenvalues of the glide

*gcuono@magtop.ifpan.edu.pl

symmetry are $+1$ and -1, and the eigenvectors are orthogonal; therefore, the bands produce a protected band crossing. In the absence of magnetism and SOC, the nonsymmorphic symmetries force the electronic bands to be degenerate at the borders of the Brillouin zone with the presence of semi-Dirac points [16,19], generating linear magnetoresistance [20], unconventional topological phases [21–27] with unique surface states, Fermi surfaces with reduced dimensionality [28], and topological nonsymmorphic crystalline superconductivity with $\mathbb{Z}_4$ topological invariant [26,27]. In the presence of SOC and magnetism, the system presents a partial or selective removal of the degeneracy [28]. The semi-Dirac points exhibit linear band dispersion in one direction (the high-symmetry direction at least in the space group 62) and quadratic band dispersion in the orthogonal direction [29]. The existence of these semi-Dirac points in the space group 62 and its relation with the nonsymmorphic symmetries has been widely demonstrated in literature [20,28,30–32]. The connection between semi-Dirac points and glide symmetry will be described later in the text.

An example of a material with the Pnma crystal phase is the CrAs compound [33,34] in the MnP-type phase, which is a rare itinerant antiferromagnet [33,34] that could exhibit AHE due to AM. Additionally, the CrAs system is not ionic, therefore, p and d bands are strongly hybridizing with a large bandwidth of the order of 11 eV [35]. This grants us the possibility to observe induced AM in the p bands. The magnetic ground state of the CrAs is a helimagnetic phase, with the components of the magnetic moment [33,34,36,37] in the a-b plane and with a spin-orbit coupling mostly from the p states of As [32,35,38]. Here we investigate the CrAs as a testbed exclusively in hypothetical collinear magnetic orders since we are mainly interested in the interplay between nonsymmorphic symmetries and AM. Further investigations are necessary to extend these results to the noncollinear phase and to understand how much AM will survive in the noncollinear phase [39]. CrAs will work as a prototype for other itinerant antiferromagnets of the same space group as $MnPd_2$, FeP, MnP, or CuMnAs that may have a smaller AHE due to the lower spin-orbit coupling [20]. Different from most studied altermagnetic Pnma compounds until now [40–42], such as $LaMnO_3$, YVO_3, and $CaCrO_3$ that have their magnetic atoms in the Wyckoff positions 4b [43], the atoms of CrAs are only present in the 4c Wyckoff positions, therefore, the system belongs to a different magnetic space group that should be more symmetric and host unexplored properties.

In this paper, we study the interplay between the altermagnetic properties of the Pnma phase and the nonsymmorphic symmetries using first-principle calculations. The computational details are reported in Appendix A. Investigating different collinear magnetic configurations as the A-type, G-type and C-type shown in Figs. 1(a)–1(c), respectively, we obtained that the altermagnetic spin-splitting is present only in the C-type configuration while it is absent in the A-type and G-type ones. Even if the C-type is not the ground state [35], we are interested in the interplay between altermagnetism and nonsymmorphic symmetries that is a general aspect that could appear in several other compounds. We find that the altermagnetic spin-splitting can be up to 0.5 eV in the d bands close to the Fermi level while it gets reduced to 0.2 eV in the p bands. Furthermore, we find that the interplay between AM and nonsymmorphic symmetries produces an intricate network of crossings and anticrossings in large areas of the Brillouin zone. As a result, the presence of nonsymmorphic symmetries generates a large anomalous Hall conductivity. The paper is organized as follows: in Sec. II, we show the main results, while Section III is devoted to conclusions.

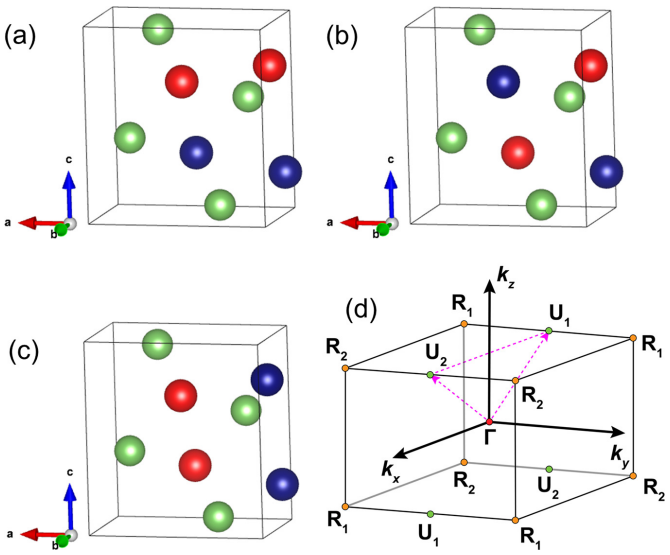

FIG. 1. Crystal structure and collinear magnetic orders for CrAs as (a) A-type, (b) G-type and (c) C-type. The balls with colors blue and red represent the Cr atoms with the opposite spin moments. Green balls represent the As atoms. (d) Symmetries of the irreducible Brillouin zone of the orthorhombic primitive cell for the C-type magnetic order. The C-type is the only magnetic order that can host AM. The position of the high-symmetry k points U_1, U_2, R_1, and R_2 are highlighted in green and yellow. The dashed magenta line indicates the high-symmetry path U_1-Γ-U_2, which is one of the possible paths to show the AM in this magnetic space group.

II. RESULTS

This Section is divided into two subsections with the results without SOC in the first one and the results with SOC in the second one. We report the electronic properties focusing on the interplay between AM and nonsymmorphic symmetries by considering different magnetic orders. The semi-Dirac points generate a large number of crossings and anticrossings that we describe. When we add the SOC in the second subsection, the calculation of the anomalous Hall conductivity (AHC) confirms a relatively large value due to the several crossings and anticrossings.

A. Electronic properties without SOC and nonsymmorphic symmetries

In the nonmagnetic phase, the bands are twofold degenerate at any k vector of the Brillouin zone due to the presence of the inversion-time reversal symmetry. This is the Kramers degeneracy and it is protected under the action of the spin-orbit coupling interaction. The nonsymmorphic symmetries produce additional degeneracy at the border of the Brillouin zone. The Γ and R points are time-reversal invariant momenta

(TRIM) points. In the Pnma space group without magnetism, the Γ point has only the Kramer degeneracy, two additional nonsymmorphic symmetries along the SR line produce an eightfold degeneracy at R and S, while X, Y, Z, U, and T have degeneracy 4 due to one nonsymmorphic symmetry. When we consider the *C*-type magnetism, Γ is a TRIM point and it still presents a twofold degeneracy. In this magnetic configuration, the TRIM points R, S, and T have fourfold degeneracy due to an additional nonsymmorphic symmetry while all the other high-symmetry points have degeneracy 2. The fourfold degeneracy at the TRIM point R makes this space group one of the few where we can study the coexistence of AM and nonsymmorphic symmetries.

We find AM in the *C*-type magnetic order, but not in the other magnetic orders and this is due to the following reasons. In the space group No. 62, there are 16 different magnetic space groups. Eight of these magnetic space groups can host AM, while the other eight groups cannot [44]. In the *C*-type magnetic order, the space groups that depend on the Néel vector belong to type I and type III. Both of these types present AM. Changing the magnetic configuration to *G*-type or *A*-type, the magnetic space group changes to type II or type IV, therefore, different magnetic configurations can have different altermagnetic properties. The CrAs contains 4*c* Wyckoff positions for both Cr and As, therefore the altermagnetic properties of the Pnma CrAs are different from the Pnma perovskites that have the magnetic atoms in 4*b* Wyckoff positions [41,42]. A spin symmetry group analysis [45] would provide additional understanding of the system.

The BZ for the *C*-type magnetic order is reported in Fig. 1(d). With subscripts 1 and 2, we indicate the two points in the k space that have opposite nonrelativistic spin splitting. In this case, the k path connecting the Γ point with U and R shows altermagnetic spin splitting. In this paper, we will take as an example for the discussion the altermagnetic properties along the path R_1-Γ-R_2. Similar arguments will be valid for the altermagnetic properties along U_1-Γ-U_2, however, the presence of multiple k paths where the AM is present means that there is a large area of the k space where the altermagnetic spin splittings reside.

We stress the relevant role of the semi-Dirac points in the generation of the band crossings and anticrossings. We focus on the semi-Dirac points at the R point, but they are present at all borders of the Brillouin zone. From the nonsymmorphic symmetries in space group No. 62, we obtain that the energy spectrum at the point $R = (\pi, \pi, \pi)$ is always a semi-Dirac point with the dispersion relations for spin-up and spin-down as

$$E_{\uparrow}(\pi - \epsilon, \pi - \epsilon, \pi - \epsilon) = \varepsilon_0 \pm v\epsilon, \quad (1)$$

$$E_{\downarrow}(\pi - \epsilon, \pi - \epsilon, \pi - \epsilon) = \varepsilon_0 \pm v\epsilon, \quad (2)$$

with ε_0 being a combination of the onsite energies and v a combination of the first-neighbor hopping parameters [28]. Since the Dirac velocity does not depend on the energy difference between majority and minority electrons, it is the same for the spin-up or spin-down channel. In the case of large hybridization between the *p*-*d* electrons, as happens in CrAs, the Dirac velocities are also large. The presence of multiple orbitals and semi-Dirac bands with large Dirac velocities, which can be positive and negative, favors the creation of several band crossings and band anticrossings which are observable in the band structure as presented in Fig. 2. What we have shown in Fig. 2 for the Cr-*d* bands close to the Fermi level happens qualitatively also for the As-*p* bands as we have described in Appendix B. The bands with opposite Dirac velocity $+v$ and $-v$ also have opposite glide eigenvalues and orthogonal eigenvectors. Therefore, the bands with opposite glide eigenvalues are orthogonal and do not hybridize each other [16,46,47]; this is exactly true for the bands with linear dispersion very close to the border of the Brillouin zone, while away from the Brillouin zone border the bands tend to show mixing of the eigenvectors. In Fig. 2, we have reported with black circles the band crossings protected by the glide symmetry.

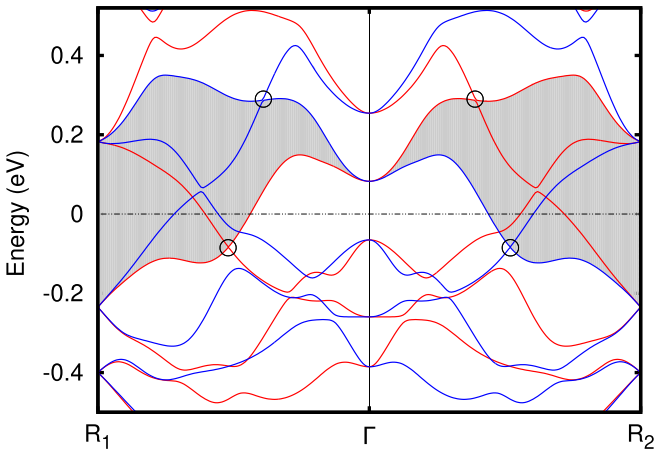

FIG. 2. Band structure of the *C*-type magnetic order along the k path R_1-Γ-R_2. The spin-up channel is shown in blue, while the spin-down channel is shown in red. The grey area represents the nonrelativistic spin splitting. The band structure is plotted between −0.5 and +0.5 eV where the *d* electrons dominate. The black circles represent the band crossings protected by glide symmetry.

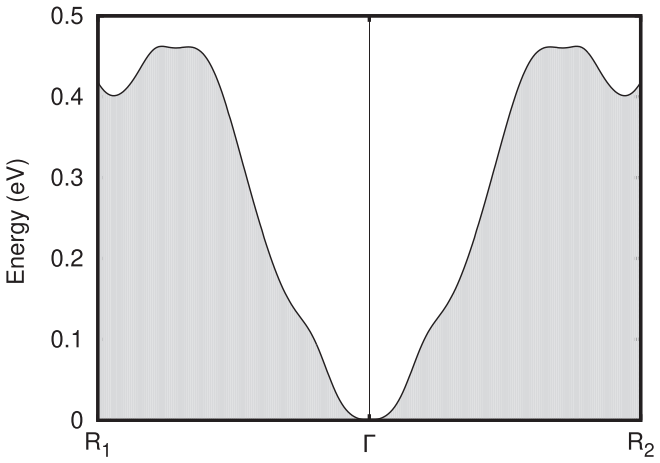

FIG. 3. Nonrelativistic spin splitting along the R_1-Γ-R_2 for the first bands above the Fermi level at the Γ point. The spin splitting reaches the value of 0.46 eV. For every couple of bands producing a finite spin splitting at the TRIM point, another couple of bands will produce an opposite spin splitting.

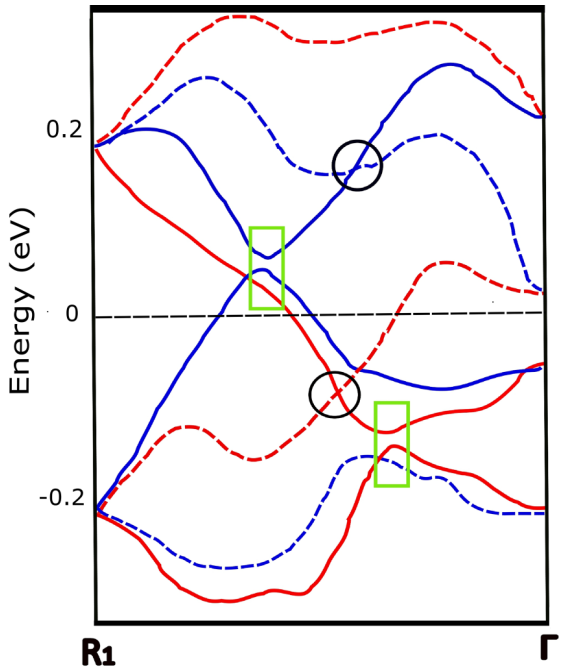

FIG. 4. Schematic representation of the crossings and anticrossings network in altermagnetic semi-Dirac fermions without SOC. The spin-up channel is shown in blue, while the spin-down channel is shown in red. The solid line is used for the positive eigenvalues of the glide operator, while the dashed line is used for the negative eigenvalue of the glide operator. The black circles represent the band crossings between band with opposite glide eigenvalues, while the green boxes represent the band anticrossings between bands with the same glide eigenvalues.

Now, we move to the analysis of the nonrelativistic spin splitting in the presence of nonsymmorphic symmetries. If we consider the Kramers pair bands which at the Γ point are at 0.1 eV above the Fermi level and follow them, we can see that the spin-up and spin-down channels have both a glide-protected band crossing and then they reach the R points at two different eigenvalues creating, surprisingly, a finite nonrelativistic spin splitting at a TRIM point as shown in Fig. 3. The nonzero value of the spin splitting at the point R apparently contradicts the concept of TRIM point, but there would be another couple of bands that would produce the opposite nonrelativistic spin splitting to preserve the total spin splitting at a given TRIM point. Due to these exceptional conditions, the nonrelativistic spin splitting for those bands, reported in Fig. 3, reaches a maximum of 0.46 eV.

In Fig. 4, we plot a schematic figure with the spin channels in blue and red colors, with the solid (dashed) line used for the positive (negative) eigenvalues of the glide operator. We have the expected intrachannel avoided band crossings and the interchannel band crossings. Additionally, we have intrachannel band crossings, namely crossings between bands with opposite glide eigenvalues. In the next subsection, we will deliberate on how these crossings will evolve with SOC as a function of the Néel vector orientation.

B. Electronic properties with SOC and Anomalous Hall conductivity

In the nonmagnetic case, when we consider the SOC, we have shown in a previous work [28] a selective removal of the bands degeneracy due to the nonsymmorphic symmetries at the TRIM points and at the borders of the Brillouin zone. In the *C*-type magnetic configuration, when we include the SOC interaction, we observe a selective removal of the spin degeneracy depending on the Néel vector direction and consequently on the magnetic space group. Indeed, the variation of the Néel vector direction changes the magnetic space group. We define the x, y, and z axis as parallel to the a, b, and c lattice constants, respectively, as defined in Fig. 1. When the Néel vector is along y, the magnetic space group is 62.441, which is a type I. When the magnetization is along x and z, the magnetic space groups are 62.446 and 62.447, respectively, which are type III. This selective removal of the degeneracy is valid along k paths with and without AM. Looking at Figs. 5 and 6, we can see that the spin-orbit splitting is qualitatively and quantitatively different depending on the magnetic space group.

It was shown that, in the nonmagnetic case, the SOC acts selectively at the TRIM points and Brillouin zone border due to the nonsymmorphic symmetries [32]. We will investigate the SOC effects in the magnetic phase as a function of the Néel vector starting from the path R_1-S-R_2 where no AM is present. Without SOC, the entire RS line including the TRIM points have degeneracy 4. The band structure with SOC along the R_1-S-R_2 k path is reported in Fig. 5. When the Néel vector is along x, the spin orbit splits the bands at R but not at S. When the Néel vector is along z, the spin orbit splits the bands at S

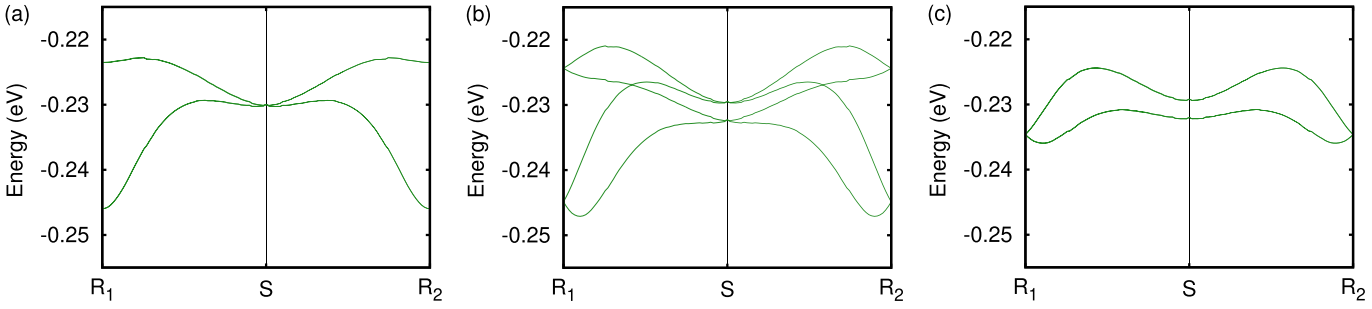

FIG. 5. Band structure along the R_1-S-R_2 k path for the *C*-type magnetic order including SOC with the Néel vector along the (a) x axis, (b) y axis and (c) z axis. No AM is present along this k path. In panel (b), we obtain the antiferromagnetic hourglass fermions with a magnetic space group type I. No hourglass fermions are found in the magnetic space groups of type III.

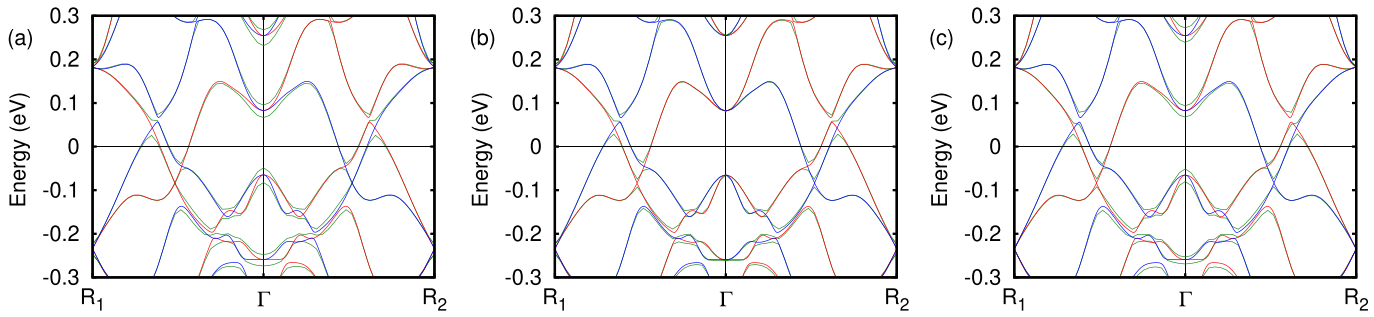

FIG. 6. Band structure of the *C*-type magnetic order along the k path R_1-Γ-R_2 with Néel vector along the (a) x axis, (b) y axis, and (c) z axis, respectively. The spin-up channel is shown in blue, the spin-down channel is shown in red, while the band structure with SOC is plotted in green. The band structure is plotted between -0.3 and $+0.3$ eV where the d electrons dominate.

but not at R. When the Néel vector is along y, the spin orbit splits the bands at both R and S, and therefore, in this latter case, we find antiferromagnetic hourglass fermions. These hourglass fermions are relativistic features already present along the RS line without magnetism [21,48,49]. Recently, the ferromagnetic and antiferromagnetic hourglass fermions were investigated. However, we find the antiferromagnetic hourglass in the magnetic space group 62.441 that was not reported before [50].

The spin orbit acts selectively also along the R_1-Γ-R_2 path where the nonrelativistic spin splitting is present. The effects of the SOC for different Néel vector orientations are reported in Fig. 6; we will highlight in the discussion the k points where the SOC is not effective. When the Néel vector is along x, we have additional SOC splittings for all the crossing and anticrossing points except that for the intrachannel crossing point at around -0.1 eV, which is protected by the glide operator as shown in Fig. 6(a). A magnification of Figs. 6(a)–6(c) is reported in Figs. 7(a)–7(c), respectively, to highlight the band crossings protected by the glide against SOC when the Néel vector is along x. Indeed, the band crossing in the black circle in Fig. 7(a) is not split by SOC, while the SOC splitting is evident in Figs. 7(b)and 7(c). It was shown that this kind of glide-protected band crossings can generate a nonisoenergetic nodal line [46,47]. Therefore, this case would be a nodal line in the altermagnetic phase; further investigations in this direction using model Hamiltonian calculations could be interesting for the topological matter community. When the Néel vector is along y, we do not have SOC splitting at the Γ point as obtained in Fig. 6(b). When the Néel vector is along z as shown in Fig. 6(c), we do not have SOC splitting at the R_1 and R_2 points coherently with what is observed in Fig. 5(c).

The Hall vector in altermagnetic systems with space group No. 62 can lie in all possible directions in principle [9]. However, when the structural details are added, the Hall vector has a precise orientation. It was shown that in space group No. 62, we can expect the Hall vector in directions orthogonal to the Néel vector [42]. Several anticrossing points appear in the whole Brillouin zone boundary due to the presence of the semi-Dirac points. These anticrossing points generate large Berry curvature and consequently a large anomalous Hall effect since, as it is well known from the literature [51–59], the intrinsic anomalous Hall effect can be expressed in terms of the Berry curvature. The semi-Dirac points and the glides linked to the nonsymmorphic symmetries are key ingredients to the generation of these several crossings and anticrossings. When we add the SOC, avoided band crossings are obtained and a large AHC is expected. Therefore, we can claim that the interplay between AM and nonsymmorphic symmetries generates large anomalous Hall conductivity. We calculate the AHC between -0.25 and $+0.25$ eV and we report it in Fig. 8 for different Néel vector orientations along the principal axes. The three AHC components that we have calculated are σ_{yz}, σ_{xz}, and σ_{xy}, the numerical details are reported in Appendix A. We obtain large values of the AHE in the two directions orthogonal to the Néel vector. When the Néel vector is along x, we obtain AHCs values up to -400 S/cm for the σ_{xy} and 300 S/cm for the σ_{xz} [see Fig. 8(a)]. When the Néel vector is

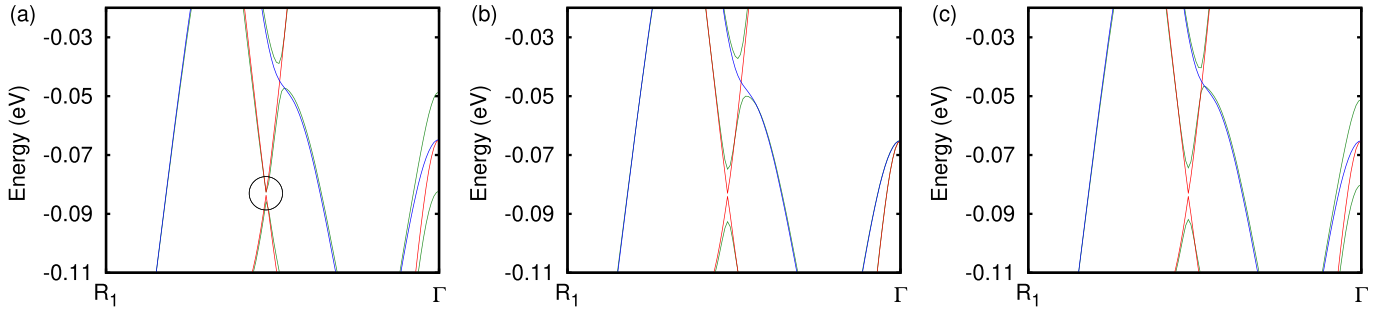

FIG. 7. Magnification of the band structure in Fig. 6. Band structure of the *C*-type magnetic order along the k path R_1-Γ with the Néel vector along the (a) x axis, (b) y axis, and (c) z axis. The band structure is plotted between -0.11 and -0.02 eV where there are the bands linear in k with opposite glide eigenvalues. The black circle in panel (a) describes the band crossing between opposite glide eigenvalues not split by SOC when the Néel vector is along x.

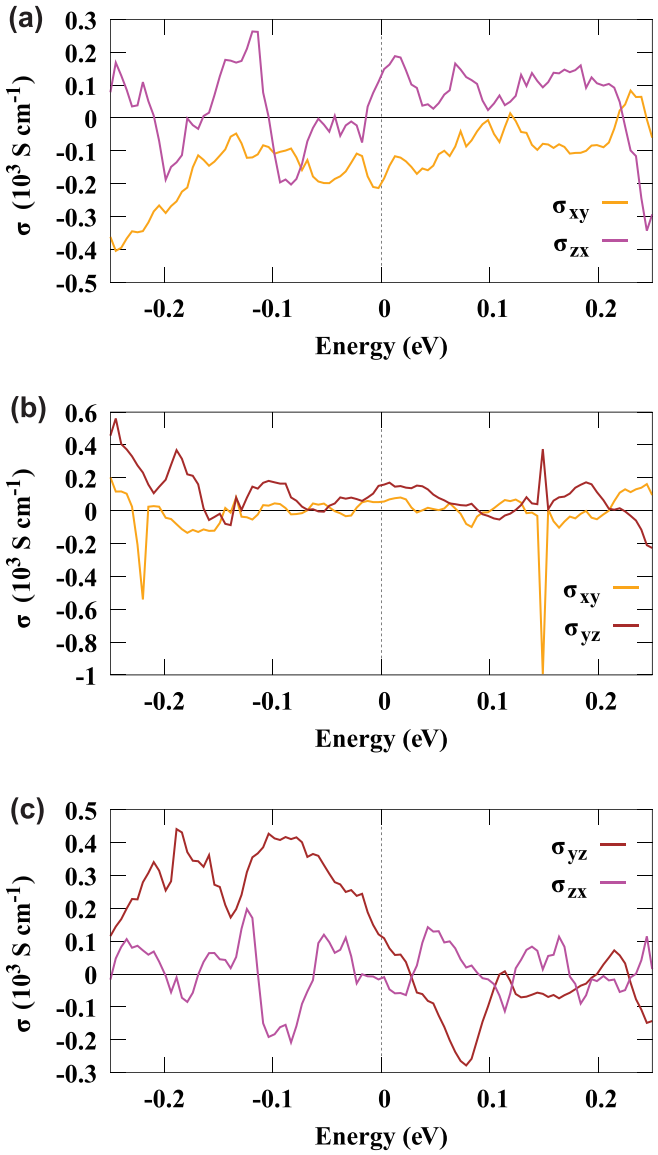

FIG. 8. Anomalous Hall effect in altermagnetic *C*-type magnetic order with Néel vector along x, along y, and along z reported in panels (a), (b), and (c), respectively. In every case, we show the AHCs σ_{xy}, σ_{xz}, and σ_{yz} for a Hall vector orthogonal to the Néel vector. The AHCs are presented between -0.25 and $+0.25$ eV, in this energy range the maximum in absolute value was reached by σ_{xy} around $-1000\ \mathrm{S\,cm^{-1}}$ with Néel vector along y axis. The Fermi energy is set to zero.

along y, we obtain AHC values up to -1000 for the σ_{yz} and $+600$ S/cm for the σ_{xy} [see Fig. 8(b)], the spike that produces the large values at $+0.14$ eV was verified with a denser energy grid. Finally, when the Néel vector is along z, we obtain AHC values up to 450 for the σ_{yz} and -200 S/cm for the σ_{xz} [see Fig. 8(c)]. We observe a strong change of all the AHCs when we switch the Néel vector from the one axis to another. The compounds with space group No. 62 and magnetic atoms in Wyckoff position 4*b* hosts the AHC in one component [42], however, compounds with the same space group but different Wyckoff positions host a Hall vector orthogonal to the Néel vector. These values are smaller but of the same order of magnitude as the AHC in other altermagnetic metallic compounds [9,42] such as RuO_2 and $CaCrO_3$.

III. CONCLUSIONS

The presence of AM varies with the magnetic configuration, since the magnetic space group type strongly depends on the magnetic configuration. For the space group No. 62 with magnetic atoms in 4*c* Wyckoff position, the nonrelativistic spin splitting is present for the *C*-type magnetic order while it is absent in *G*-type and *A*-type magnetic orders. Following a couple of bands with opposite spin from the degenerate Γ point through the glide-protected crossing, we can end up with a finite spin splitting at the TRIM points R_1 and R_2, however, there would be another couple of bands that would produce the opposite spin splitting, restoring the zero nonrelativistic spin splitting at the TRIM points. The magnetic space group is type I when the Néel vector is along y and type III when the Néel vector is along x or z. A selective removal of the spin degeneracy acts as a function of the magnetic space group at the TRIM points. For example, in the type-I magnetic space group, we find antiferromagnetic hourglass electrons that are not present when the Néel vector is along x or z. When the Néel is along x, we have a glide-protected crossing that could generate a nodal line in the altermagnetic phase. Due to the semi-Dirac points and glide symmetries, the interplay between AM and nonsymmorphic symmetries produces several band crossings and avoided band crossings; once we apply the SOC these crossings generate a large AHC of the same order of magnitude found in altermagnetic RuO_2 and $CaCrO_3$.

ACKNOWLEDGMENTS

We thank Tomasz Dietl, Canio Noce, and Rajibul Islam for useful discussions. The work is supported by the Foundation for Polish Science through the International Research Agendas program cofinanced by the European Union within the Smart Growth Operational Program (Grant No. MAB/2017/1). A.F. was supported by the Polish National Science Center under Project No. 2020/37/B/ST5/02299. We acknowledge the access to the computing facilities of the Interdisciplinary Center of Modeling at the University of Warsaw, Grants No. g91-1418, No. g91-1419, and No. g91-1426, for the availability of high-performance computing resources and support. We acknowledge the CINECA award under the ISCRA initiative Grants No. IsC99 "SILENTS", No. IsC105 "SILENTSG", and No. IsB26 "SHINY" for the availability of high-performance computing resources and support. We acknowledge the access to the computing facilities of the Poznan Supercomputing and Networking Center Grant No. 609.

APPENDIX A: COMPUTATIONAL DETAILS

We performed density-functional theory (DFT) calculations by using the VASP package [60–62]. We employed the local density approximation and the Perdew–Zunger [63] parametrization of the Ceperly-Alder data [64]. The same parameters of previous works [35] as the lattice constants and atomic positions of Ref. [36] have been used. The lat-

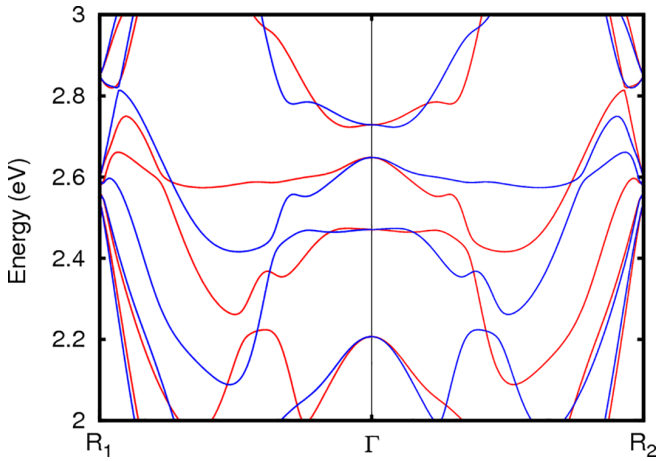

FIG. 9. Band structure of the C-type magnetic order along the k-path R_1-Γ-R_2. The spin-up channel is shown in blue, while the spin-down channel is shown in red. The band structure is plotted between +2 and +3 eV where the As p-electrons dominate.

tice constants are a = 5.60499 Å, b = 3.58827 Å, and c = 6.13519 Å, while the Wyckoff positions both in 4c are Cr: (0.0070, 1/4, 0.2049) and As: (0.2045, 1/4, 0.5836). The band structure plots were obtained with 130 k points for every path. Close to the Fermi level we have the Cr d orbitals sandwiched between As p orbitals [35]. We performed the wannierization [65,66] by using the WANNIER90 code [67] and we considered the Cr-3d and As-4p orbitals as we have already done in previous papers [28,32,68–71]. For the calculation of the anomalous Hall conductivity we used WANNIERTOOLS code [72]; we have used a k grid 200 × 200 × 200. The AHC calculations were verified with a k grid of 300 × 300 × 300 that reproduces the same results with negligible differences [73]. The information about the magnetic space groups were extracted by the Bilbao Crystallographic Server [44].

APPENDIX B: INDUCED ALTERMAGNETISM IN *P* BANDS

As mentioned in the main text, the system hosts a strong p-d hybridization [28], therefore, the AM can be induced from the Cr d bands to the As p bands. The d bands dominate up to 1.5 eV above the Fermi level [32], while above 2 eV the bands are mainly composed by As-4p spectral weight. The altermagnetic spin splitting is of the order of 0.5 eV on the magnetic d bands close to the Fermi level and survives in the p bands through the d-p hybridization but it gets reduced. The largest spin splitting in the p orbitals is around 0.2 eV, as we can see in Fig. 9. The Cr d bands induce AM in As p bands, this is slightly different from the AM in $EuIn_2As_2$ where the magnetic f bands of Eu induce AM on the d bands of the same Eu atoms [74].

[1] L. Šmejkal, J. Sinova, and T. Jungwirth, Phys. Rev. X **12**, 040501 (2022).
[2] L. Šmejkal, J. Sinova, and T. Jungwirth, Phys. Rev. X **12**, 031042 (2022).
[3] L.-D. Yuan and A. Zunger, Adv. Mater. **35**, 2211966 (2023).
[4] S. Hayami, Y. Yanagi, and H. Kusunose, J. Phys. Soc. Jpn. **88**, 123702 (2019).
[5] S. Hayami, Y. Yanagi, and H. Kusunose, Phys. Rev. B **102**, 144441 (2020).
[6] X. Chen, D. Wang, L. Li, and B. Sanyal, Appl. Phys. Lett. **123**, 022402 (2023).
[7] Y. Guo, H. Liu, O. Janson, I. C. Fulga, J. van den Brink, and J. I. Facio, Mater. Today Phys. **32**, 100991 (2023).
[8] C. Bradley and A. P. Cracknell, *The Mathematical Theory of Symmetry in Solids*, Oxford Classic Texts in the Physical Sciences (Oxford University Press, London, England, 2009).
[9] L. Šmejkal, R. González-Hernández, T. Jungwirth, and J. Sinova, Sci. Adv. **6**, eaaz8809 (2020).
[10] Z. Feng, X. Zhou, L. Šmejkal, L. Wu, Z. Zhu, H. Guo, R. González-Hernández, X. Wang, H. Yan, P. Qin, X. Zhang, H. Wu, H. Chen, Z. Meng, L. Liu, Z. Xia, J. Sinova, T. Jungwirth, and Z. Liu, Nat. Electron. **5**, 735 (2022).
[11] X. Zhou, W. Feng, R.-W. Zhang, L. Smejkal, J. Sinova, Y. Mokrousov, and Y. Yao, arXiv:2305.01410 [cond-mat.mtrl-sci].
[12] J. A. Ouassou, A. Brataas, and J. Linder, Phys. Rev. Lett. **131**, 076003 (2023).
[13] P. Qin, H. Yan, X. Wang, H. Chen, Z. Meng, J. Dong, M. Zhu, J. Cai, Z. Feng, X. Zhou, L. Liu, T. Zhang, Z. Zeng, J. Zhang, C. Jiang, and Z. Liu, Nature (London) **613**, 485 (2023).
[14] D.-F. Shao, S.-H. Zhang, M. Li, C.-B. Eom, and E. Y. Tsymbal, Nat. Commun. **12**, 7061 (2021).
[15] R. M. Fernandes, V. S. de Carvalho, T. Birol, and R. G. Pereira, arXiv:2307.12380 [cond-mat.mes-hall].
[16] Y. X. Zhao and A. P. Schnyder, Phys. Rev. B **94**, 195109 (2016).
[17] H. Watanabe, H. C. Po, M. P. Zaletel, and A. Vishwanath, Phys. Rev. Lett. **117**, 096404 (2016).
[18] A. König and N. D. Mermin, Phys. Rev. B **56**, 13607 (1997).
[19] B. J. Wieder, Y. Kim, A. M. Rappe, and C. L. Kane, Phys. Rev. Lett. **116**, 186402 (2016).
[20] D. J. Campbell, J. Collini, J. Sławińska, C. Autieri, L. Wang, K. Wang, B. Wilfong, Y. S. Eo, P. Neves, D. Graf, E. E. Rodriguez, N. P. Butch, M. Buongiorno Nardelli, and J. Paglione, npj Quantum Mater. **6**, 38 (2021).
[21] Z. Wang, A. Alexandradinata, R. J. Cava, and B. A. Bernevig, Nature (London) **532**, 189 (2016).
[22] T. Bzdušek, Q. Wu, A. Rüegg, and M. Sigrist, Nature (London) **538**, 75 (2016).
[23] S. A. Parameswaran, A. M. Turner, D. P. Arovas, and A. Vishwanath, Nat. Phys. **9**, 299 (2013).
[24] B. J. Wieder and C. L. Kane, Phys. Rev. B **94**, 155108 (2016).
[25] W. Brzezicki and M. Cuoco, Phys. Rev. B **95**, 155108 (2017).
[26] T. Yoshida, A. Daido, N. Kawakami, and Y. Yanase, Phys. Rev. B **99**, 235105 (2019).
[27] A. Daido, T. Yoshida, and Y. Yanase, Phys. Rev. Lett. **122**, 227001 (2019).
[28] G. Cuono, F. Forte, M. Cuoco, R. Islam, J. Luo, C. Noce, and C. Autieri, Phys. Rev. Mater. **3**, 095004 (2019).
[29] P. Adroguer, D. Carpentier, G. Montambaux, and E. Orignac, Phys. Rev. B **93**, 125113 (2016).

[30] Q. Niu, W. C. Yu, K. Y. Yip, Z. L. Lim, H. Kotegawa, E. Matsuoka, H. Sugawara, H. Tou, Y. Yanase, and S. K. Goh, Nat. Commun. **8**, 15358 (2017).

[31] Q. Niu, W. C. Yu, E. I. Paredes Aulestia, Y. J. Hu, K. T. Lai, H. Kotegawa, E. Matsuoka, H. Sugawara, H. Tou, D. Sun, F. F. Balakirev, Y. Yanase, and S. K. Goh, Phys. Rev. B **99**, 125126 (2019).

[32] G. Cuono, C. Autieri, G. Guarnaccia, A. Avella, M. Cuoco, F. Forte, and C. Noce, Eur. Phys. J.: Spec. Top. **228**, 631 (2019).

[33] W. Wu, X. Zhang, Z. Yin, P. Zheng, N. Wang, and J. Luo, Sci. China: Phys., Mech. Astron. **53**, 1207 (2010).

[34] W. Wu, J. Cheng, K. Matsubayashi, P. Kong, F. Lin, C. Jin, N. Wang, Y. Uwatoko, and J. Luo, Nat. Commun. **5**, 5508 (2014).

[35] C. Autieri and C. Noce, Philos. Mag. **97**, 3276 (2017).

[36] Y. Shen, Q. Wang, Y. Hao, B. Pan, Y. Feng, Q. Huang, L. W. Harriger, J. B. Leao, Y. Zhao, R. M. Chisnell, J. W. Lynn, H. Cao, J. Hu, and J. Zhao, Phys. Rev. B **93**, 060503(R) (2016).

[37] L. Keller, J. S. White, M. Frontzek, P. Babkevich, M. A. Susner, Z. C. Sims, A. S. Sefat, H. M. Rønnow, and C. Rüegg, Phys. Rev. B **91**, 020409(R) (2015).

[38] A. S. Wadge, G. Grabecki, C. Autieri, B. J. Kowalski, P. Iwanowski, G. Cuono, M. F. Islam, C. M. Canali, K. Dybko, A. Hruban, A. Łusakowski, T. Wojciechowski, R. Diduszko, A. Lynnyk, N. Olszowska, M. Rosmus, J. Kołodziej, and A. Wiśniewski, J. Phys.: Condens. Matter **34**, 125601 (2022).

[39] Y.-P. Zhu, X. Chen, X.-R. Liu, P. Liu, H. Zha, C. Hong, J. Li, Z. Jiang, X.-M. Ma, Y.-J. Hao, W. Liu, M. Zeng, J. Ding, S. Mo, Z. Liu, M. Ye, D. Shen, R.-H. He, S. Qiao, Q. Liu, and C. Liu, arXiv:2303.04549 [cond-mat.mtrl-sci].

[40] R. M. Sattigeri, G. Cuono, and C. Autieri, arXiv:2307.10146 [cond-mat.mtrl-sci].

[41] G. Cuono, R. M. Sattigeri, J. Skolimowski, and C. Autieri, J. Magn. Magn. Mater. **586**, 171163 (2023).

[42] T. P. T. Nguyen and K. Yamauchi, Phys. Rev. B **107**, 155126 (2023).

[43] C. Autieri, M. Cuoco, G. Cuono, S. Picozzi, and C. Noce, Phys. B: Condens. Matter **648**, 414407 (2023).

[44] S. V. Gallego, E. S. Tasci, G. de la Flor, J. M. Perez-Mato, and M. I. Aroyo, J. Appl. Crystallogr. **45**, 1236 (2012).

[45] P. Liu, J. Li, J. Han, X. Wan, and Q. Liu, Phys. Rev. X **12**, 021016 (2022).

[46] X. Zhou, C.-H. Hsu, H. Aramberri, M. Iraola, C.-Y. Huang, J. L. Mañes, M. G. Vergniory, H. Lin, and N. Kioussis, Phys. Rev. B **104**, 125135 (2021).

[47] J. Bannies, E. Razzoli, M. Michiardi, H.-H. Kung, I. S. Elfimov, M. Yao, A. Fedorov, J. Fink, C. Jozwiak, A. Bostwick, E. Rotenberg, A. Damascelli, and C. Felser, Phys. Rev. B **103**, 155144 (2021).

[48] L. Wang, S.-K. Jian, and H. Yao, Phys. Rev. B **96**, 075110 (2017).

[49] S. Li, Y. Liu, S.-S. Wang, Z.-M. Yu, S. Guan, X.-L. Sheng, Y. Yao, and S. A. Yang, Phys. Rev. B **97**, 045131 (2018).

[50] Y. Hu, X. Wan, and F. Tang, Phys. Rev. B **106**, 165128 (2022).

[51] N. Nagaosa, J. Sinova, S. Onoda, A. H. MacDonald, and N. P. Ong, Rev. Mod. Phys. **82**, 1539 (2010).

[52] D. Xiao, M.-C. Chang, and Q. Niu, Rev. Mod. Phys. **82**, 1959 (2010).

[53] Y. Taguchi, Y. Oohara, H. Yoshizawa, N. Nagaosa, and Y. Tokura, Science **291**, 2573 (2001).

[54] T. Chakraborty, K. Samanta, S. N. Guin, J. Noky, I. n. Robredo, S. Prasad, J. Kuebler, C. Shekhar, M. G. Vergniory, and C. Felser, Phys. Rev. B **106**, 155141 (2022).

[55] C.-P. Zhang, X.-J. Gao, Y.-M. Xie, H. C. Po, and K. T. Law, Phys. Rev. B **107**, 115142 (2023).

[56] T. Jungwirth, Q. Niu, and A. H. MacDonald, Phys. Rev. Lett. **88**, 207208 (2002).

[57] Y. Yao, L. Kleinman, A. H. MacDonald, J. Sinova, T. Jungwirth, D.-S. Wang, E. Wang, and Q. Niu, Phys. Rev. Lett. **92**, 037204 (2004).

[58] H. Chen, Q. Niu, and A. H. MacDonald, Phys. Rev. Lett. **112**, 017205 (2014).

[59] T. C. van Thiel, W. Brzezicki, C. Autieri, J. R. Hortensius, D. Afanasiev, N. Gauquelin, D. Jannis, N. Janssen, D. J. Groenendijk, J. Fatermans, S. Van Aert, J. Verbeeck, M. Cuoco, and A. D. Caviglia, Phys. Rev. Lett. **127**, 127202 (2021).

[60] G. Kresse and J. Hafner, Phys. Rev. B **47**, 558 (1993).

[61] G. Kresse and J. Furthmüller, Comput. Mater. Sci. **6**, 15 (1996).

[62] G. Kresse and J. Furthmüller, Phys. Rev. B **54**, 11169 (1996).

[63] J. P. Perdew and A. Zunger, Phys. Rev. B **23**, 5048 (1981).

[64] D. M. Ceperley and B. J. Alder, Phys. Rev. Lett. **45**, 566 (1980).

[65] N. Marzari and D. Vanderbilt, Phys. Rev. B **56**, 12847 (1997).

[66] I. Souza, N. Marzari, and D. Vanderbilt, Phys. Rev. B **65**, 035109 (2001).

[67] A. A. Mostofi, J. R. Yates, Y.-S. Lee, I. Souza, D. Vanderbilt, and N. Marzari, Comput. Phys. Commun. **178**, 685 (2008).

[68] C. Autieri, G. Cuono, F. Forte, and C. Noce, J. Phys.: Condens. Matter **29**, 224004 (2017).

[69] C. Autieri, G. Cuono, F. Forte, and C. Noce, J. Phys.: Conf. Ser. **969**, 012106 (2018).

[70] G. Cuono, C. Autieri, F. Forte, G. Busiello, M. T. Mercaldo, A. Romano, C. Noce, and A. Avella, AIP Adv. **8**, 101312 (2018).

[71] G. Cuono, C. Autieri, F. Forte, M. T. Mercaldo, A. Romano, A. Avella, and C. Noce, New J. Phys. **21**, 063027 (2019).

[72] Q. Wu, S. Zhang, H.-F. Song, M. Troyer, and A. A. Soluyanov, Comput. Phys. Commun. **224**, 405 (2018).

[73] M. S. Alam, A. Fakhredine, M. Ahmad, P. K. Tanwar, H.-Y. Yang, F. Tafti, G. Cuono, R. Islam, B. Singh, A. Lynnyk, C. Autieri, and M. Matusiak, Phys. Rev. B **107**, 085102 (2023).

[74] G. Cuono, R. M. Sattigeri, C. Autieri, and T. Dietl, Phys. Rev. B **108**, 075150 (2023).

CHAPTER 7

OUTLOOK

The field of spintronics has developed over the past decades where the manufacture of devices is mainly focused on manipulating both the charge and the spin degree of freedom[95]. The lack of time-reversal symmetry (TRS) in certain systems plays a huge role in enabling and stabilizing spin-polarized currents due to the lifted degeneracy between spin-up and spin-down states. In systems with large spin-orbit coupling, the breaking of TRS is necessary to generate topologically protected phases in both real and reciprocal space. In the reciprocal space, the spin-orbit and the breaking of the TRS can generate Weyl semimetal and quantum anomalous Hall phases, while in the real space, the main key focuses today shifts toward experimental spintronic devices that can exploit spin-textured topological states[96]. In many studies, it has been shown that systems with both a broken TRS and the absence of inversion symmetry are among the most promising for some applications such as the generation of spin-textured skyrmions and their variants.
In ferromagnetic systems, the presence of spin-orbit coupling (SOC) effects has been of growing importance remarkably in heterostructures where the SOC strength has shown comparable energy scales and therefore is promising for new spin-based applications. The emergence of the net Dzyaloshinskii-Moriya interaction (DMI), which requires the breaking of the inversion symmetry, has been shown essential to stabilize spin textures in ferromagnetic ultra-thin films[97]. DMI enables controlled, deterministic switching of magnetic states via spin-orbit torque (SOT), reducing critical current thresholds in certain materials and supporting advanced functionalities like multilevel storage and programmable spin logic gates, making it pivotal for efficient spintronic devices[98]. The existence of the DMI is also important for understanding the emergence of skyrmions which are also very promising candidates in applications concerning memory devices, skyrmion racetrack, transistors, and many other functions[99]. These topological objects have been realized experimentally in thin films and future advances in this field are essential and

prosperous as they offer great potential as systematic information carriers although certain limitations should be taken into consideration which might reduce their utility in spintronic devices[100].

In materials that combine both broken TRS and inversion symmetry, SOC can have a substantial impact on their electronic properties and topological phenomena in the reciprocal space, as demonstrated in our study of CeAlSi. Specifically, the presence of SOC in this system, alongside the dual symmetry-breaking properties, enables the formation of Weyl points, which act as sources and sinks of the Berry curvature. This non-trivial Berry curvature distribution induced by SOC gives rise to the tunable anomalous Hall effect (AHE) in CeAlSi. The exotic properties exhibited by Weyl semimetals (WSMs) hold great potential for high-speed electronics and spintronic applications. Their gapless nature enables high mobility with minimal resistance, and they also exhibit large magnetoresistance due to the chiral anomaly[25, 101, 102]. WSMs can also demonstrate a strong spin Hall effect due to their large Berry curvature and SOC. This characteristic is anticipated to play a crucial role in spin Hall effect devices capable of efficiently converting charge current into spin current.

The emergence of the anomalous Hall effect (AHE) has been recently extended to the newly discovered field dubbed "altermagnetism" upon the inclusion of SOC in which the lack of TRS is a built-in property. The altermagnets exhibit faster spin dynamics and lower sensitivity to stray magnetic fields compared to ferromagnetic materials. Many compounds including CrAs which have been studied in this thesis have opened new perspectives of what is named "spin-split antiferromagnetic spintronics"[103]. The AHE offers the potential for developing innovative spintronic devices, such as the Hall balance, which can significantly boost magnetoelectronic ratios. In other altermagnetic compounds like RuO_2 and MnTe, research has also confirmed that the AHE can be measured and that it explicitly depends on the orientation of the Néel vector. The Néel vector of RuO_2 has been predicted to be tunable by spin transfer torques, and possibly by spin-orbit torques paving the way to antiferromagnetic spintronic devices[104]. The field of altermagnetism has shown very promising physical properties that can revolutionize fields such as data storage, spintronics, spin-to-charge conversion, faster spin-caloritronic devices, and magnetic sensing by providing more efficient and long-lasting alternatives to conventional ferromagnetic and antiferromagnetic materials[105].

We believe that future research should prioritize the realization of protected magnetic structures in real space, such as skyrmions, within systems exhibiting an interplay between ferromagnetism and SOC. Progress in this area, alongside theoretical predictions using mesoscopic-scale approaches like atomistic spin dynamics and micromagnetic simulations, holds great promise. Regarding altermagnetic systems, research is still open for investigation theoretically and experimentally towards combining altermagnetism and topology in real and reciprocal space. Another aspect to investigate is the robustness of the weak ferromagnetism in real materials where domains and other defects are present. Experimentally, one of the main challenges would be the

control of the magnetic domains with different Néel vectors which is relevant for the realization of possible devices based on altermagnetism.

INSTYTUT FIZYKI
POLSKIEJ AKADEMII NAUK

Date: 04 November 2024

STATEMENT

I declare that my contribution to the paper **Amar Fakhredine**, Andrzej Wawro, and Carmine Autieri. "Huge Dzyaloshinskii–Moriya interactions in Pt/Co/Re thin films." *Journal of Applied Physics* 135, no. 3 (2024) is related to:

i. Performing all the density functional theory calculations and collecting the data.

ii. Analyzing the results and producing all the figures.

iii. Writing the draft.

iv. Discussion of the scientific results.

Amar Fakhredine

PhD student of ON-3.4 at the Institute of Physics, Polish Academy of Science IFPAN
E-mail: amarf@ifpan.edu.pl
Google Scholar profile:
https://scholar.google.com/citations?user=Jp_m9k4AAAAJ&hl=en&oi=ao
Researchgate profile: https://www.researchgate.net/profile/Amar-Fakhredine/research

INSTYTUT FIZYKI
POLSKIEJ AKADEMII NAUK

Date: 6 September 2024

STATEMENT

I declare that my contribution to the paper **A. Fakhredine,** A. Wawro, C. Autieri, "Huge Dzyaloshinskii–Moriya interactions in Pt/Co/Re thin films" published in J. Appl. Phys. **135**, 035303 (2024) has been related to the discussion on the scientific project and the supervision of the project.

Yours Faithfully,

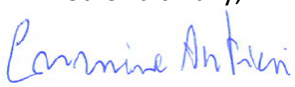

Carmine Autieri

Dr. hab. Carmine Autieri, IFPAN professor at the International Centre for Interfacing Magnetism and Superconductivity with Topological Matter (MagTop),
E-mail: autieri@MagTop.ifpan.edu.pl
Website: https://www.magtop.ifpan.edu.pl/resources/teams/
Google Scholar profile: https://scholar.google.it/citations?user=83pF0ywAAAA
ResearchGate profile: https://www.researchgate.net/profile/Carmine_Autieri

Warsaw, Nov. 6th, 2024

prof. dr hab. Andrzej Wawro
Institute of Physics Polish Academy of Sciences

Declaration of contribution

Hereby, I declare that my contribution to the research article as below included in the doctoral thesis by Amar Fakhredine entitled: "*Interplay between non-relativistic spin-splitting and spin-orbit coupling in metallic systems*" is the following:

Amar Fakhredine, Andrzej Wawro, and Carmine Autieri; "Huge Dzyaloshinskii–Moriya interactions in Pt/Co/Re thin films"; *Journal of Applied Physics* ***135****, 035303 (2024).*

> Suggestion of the investigated system and the interface structure

> Discussion of the obtained results

> Participation in the preparation of the paper final version.

I am a head of the project financed by the National Science Centre in Poland (no.: 2020/37/B/ST5/02299) from which this research was supported and Amar Fakhredine's PhD scholarship was paid.

Andrzej Waldemar Wawro

Elektronicznie podpisany przez Andrzej Waldemar Wawro
Data: 2024.11.06 19:38:18 +01'00'

UNIWERSYTET
IM. ADAMA MICKIEWICZA
W POZNANIU

Dated – 02nd October 2024

Statement

I declare that my contribution to the paper with authors Anuj Kumar Dhiman, **Amar Fakhredine**, Ryszard Gieniusz, Zbigniew Kurant, Iosif Sveklo, Piotr Dłużewski, Wojciech Dobrogowski, Sukanta Kumar Jena, Aleksiej Pietruczik, Carmine Autieri, Andrzej Wawro, and Andrzej Maziewski with title ”Evolution of static and dynamic magnetic properties of Re/Co/Pt and Pt/Co/Re trilayers with enhanced Dzyaloshinskii-Moriya interaction” published on **Applied Surface Science** vol. 679, 161151 (2024). I have contributed in this work through experimental measurements, scientific results discussion and manuscript writing & editing.

Yours Faithfully,

Anuj Kumar Dhiman

Postdoctoral scholar, Faculty of Physics,

Adam Mickiewicz University, Poznan, Poland

Email – dhianu@amu.edu.pl

INSTYTUT FIZYKI
POLSKIEJ AKADEMII NAUK

Date: 04 November 2024

STATEMENT

I declare that my contribution to the paper Anuj Kumar Dhiman, **Amar Fakhredine**, Ryszard Gieniusz, Zbigniew Kurant, Iosif Sveklo, Piotr Dłużewski, Wojciech Dobrogowski et al. "Evolution of static and dynamic magnetic properties of Re/Co/Pt and Pt/Co/Re trilayers with enhanced Dzyaloshinskii-Moriya interaction." *Applied Surface Science* 679 (2025): 161151 is related to:

i. Performing the density functional theory calculations related to the theoretical part.

ii. Analyzing and providing the data for figure 6 in the main text and figure S4 in the supplementary material.

iii. Writing the theoretical part.

Amar Fakhredine

PhD student of ON-3.4 at the Institute of Physics, Polish Academy of Science IFPAN
E-mail: amarf@ifpan.edu.pl
Google Scholar profile:
https://scholar.google.com/citations?user=Jp_m9k4AAAAJ&hl=en&oi=ao
Researchgate profile: https://www.researchgate.net/profile/Amar-Fakhredine/research

WYDZIAŁ FIZYKI
UNIWERSYTET W BIAŁYMSTOKU
Dr hab. Ryszard Gieniusz, prof. UwB,
Faculty of Physics, University of Bialystok, Białystok, Poland

Date: 08 October 2024

STATEMENT

I declare that my contribution to the paper with authors Anuj Kumar Dhiman, **Amar Fakhredine**, Ryszard Gieniusz, Zbigniew Kurant, Iosif Sveklo, Piotr Dłużewski, Wojciech Dobrogowski, Sukanta Kumar Jena, Aleksiej Pietruczik, Carmine Autieri, Andrzej Wawro, Andrzej Maziewski and with title "Evolution of static and dynamic magnetic properties of Re/Co/Pt and Pt/Co/Re trilayers with enhanced Dzyaloshinskii-Moriya interaction" published on Applied Surface Science 679, 161151, (2025) https://doi.org/10.1016/j.apsusc.2024.161151 has been related to the made BLS measurements and analysis.

Yours Faithfully,

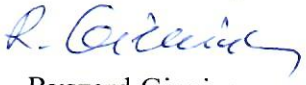

Ryszard Gieniusz

WYDZIAŁ FIZYKI
UNIWERSYTET W BIAŁYMSTOKU

Date: 18 October 2024

STATEMENT

I declare that my contribution to the paper with authors Anuj Kumar Dhiman, **Amar Fakhredine**, Ryszard Gieniusz, Zbigniew Kurant, Iosif Sveklo, Piotr Dłużewski, Wojciech Dobrogowski, Sukanta Kumar Jena, Aleksiej Pietruczik, Carmine Autieri, Andrzej Wawro, Andrzej Maziewski and with title "Evolution of static and dynamic magnetic properties of Re/Co/Pt and Pt/Co/Re trilayers with enhanced Dzyaloshinskii-Moriya interaction" published on Applied Surface Science 679, 161151, (2025) has been related to writing – original draft and magneto-optics investigation and data analysis.

Zbigniew Kurant

INSTYTUT FIZYKI
POLSKIEJ AKADEMII NAUK

Date: 01 October 2024

STATEMENT

I declare that my contribution to the paper with authors Anuj Kumar Dhiman, **Amar Fakhredine**, Ryszard Gieniusz,Zbigniew Kurant, Iosif Sveklo, Piotr Dłużewski, Wojciech Dobrogowski, Sukanta Kumar Jena, Aleksiej Pietruczik, Carmine Autieri, Andrzej Wawro, Andrzej Maziewski and with title "Evolution of static and dynamic magnetic properties of Re/Co/Pt and Pt/Co/Re trilayers with enhanced Dzyaloshinskii-Moriya interaction" published on **Applied Surface Science, Volume 679, 15 January 2025, 161151**, has been related to the discussion on the scientific results.

Yours Faithfully,

A. Pietruczik

Aleksiej Pietruczik

Institute of Physics, Polish Academy of Sciences, Aleja Lotników 32/46, 02-668 Warsaw, Poland

INSTYTUT FIZYKI
POLSKIEJ AKADEMII NAUK

Date: 16 September 2024

STATEMENT

I declare that my contribution to the paper with authors Anuj Kumar Dhiman, **Amar Fakhredine**, Ryszard Gieniusz,Zbigniew Kurant, Iosif Sveklo, Piotr Dłużewski, Wojciech Dobrogowski, Sukanta Kumar Jena, Aleksiej Pietruczik, Carmine Autieri, Andrzej Wawro, Andrzej Maziewski and with title ”Evolution of static and dynamic magnetic properties of Re/Co/Pt and Pt/Co/Re trilayers with enhanced Dzyaloshinskii-Moriya interaction” published on Applied Surface Science 679 (2025): 161151 has been related to the discussion on the scientific results.

Yours Faithfully,

Carmine Autieri

Dr. hab. Carmine Autieri, Institute Professor at the International Centre for Interfacing Magnetism and Superconductivity with Topological Matter (MagTop),
E-mail: autieri@MagTop.ifpan.edu.pl
Website: https://www.magtop.ifpan.edu.pl/resources/teams/
Google Scholar profile: https://scholar.google.it/citations?user=83pF0ywAAAA
ResearchGate profile: https://www.researchgate.net/profile/Carmine_Autieri

Warsaw, Nov. 6th, 2024

prof. dr hab. Andrzej Wawro
Institute of Physics Polish Academy of Sciences

Declaration of contribution

Hereby, I declare that my contribution to the research article as below included in the doctoral thesis by Amar Fakhredine entitled: "*Interplay between non-relativistic spin-splitting and spin-orbit coupling in metallic systems*" is the following:

Anuj Kumar Dhiman, Amar Fakhredine, Ryszard Gieniusz, Zbigniew Kurant, Iosif Sveklo, Piotr Dłużewski, Wojciech Dobrogowski, Sukanta Kumar Jena, Aleksiej Pietruczik, Carmine Autieri, Andrzej Wawro, and Andrzej Maziewski;"Evolution of static and dynamic magnetic properties of Re/Co/Pt and Pt/Co/Re trilayers with enhanced Dzyaloshinskii-Moriya interaction"; *Applied Surface Science* ***679****, 161151 (2025).*

> Suggestion of the investigated system

> Responsibility for the samples fabrication

> Responsibility for sample structural investigations

> Discussion of the obtained results

> Participation in the preparation of the paper final version.

I am a head of the project financed by the National Science Centre in Poland (no.: 2020/37/B/ST5/02299) from which this research was supported and Amar Fakhredine's PhD scholarship was paid.

Andrzej Waldemar Wawro

Elektronicznie podpisany przez Andrzej Waldemar Wawro
Data: 2024.11.06 19:37:14 +01'00'

Prof. dr hab. Andrzej Maziewski
Department of Physics of Magnetism
Faculty of Physics
University of Białystok

STATEMENT

I declare that my contribution to the paper with authors Anuj Kumar Dhiman, **Amar Fakhredine**, Ryszard Gieniusz, Zbigniew Kurant, Iosif Sveklo, Piotr Dłużewski, Wojciech Dobrogowski, Sukanta Kumar Jena, Aleksiej Pietruczik, Carmine Autieri, Andrzej Wawro, Andrzej Maziewski and with title "Evolution of static and dynamic magnetic properties of Re/Co/Pt and Pt/Co/Re trilayers with enhanced Dzyaloshinskii-Moriya interaction" published on Applied Surface Science 679 (2025) 161151 has been related to the discussion on the scientific results.

UNIVERSITAS BIALOSTOCENSIS 1997

Andrzej Maziewski
2024.11.07
12:22:17 +01'00'

INSTYTUT FIZYKI
POLSKIEJ AKADEMII NAUK

Date: 30 October 2024

STATEMENT

I declare that my contribution to the paper Md Shahin Alam, **Amar Fakhredine**, Mujeeb Ahmed, P.K. Tanwar, Hung-Yu Yang, Fazel Tafti, Giuseppe Cuono, Rajibul Islam, Bahadur Singh, Artem Lynnyk, Carmine Autieri, Marcin Matusiak, Sign change of anomalous Hall effect and anomalous Nernst effect in the Weyl semimetal CeAlSi, Phys. Rev. B **107**, 085102 (2023) is as follows,

Measurements: I did the measurements
Data Analysis: I analyzed the collected data and discuss with Amar Fakhredine for theoretical support
Figures: I made the figures (except for the DFT figures).
Manuscript: I prepared the draft (except for the DFT part).

Yours Faithfully,

Md. Shahin Alam.

Md Shahin Alam

Institute of Physics, Polish Academy of Sciences, Aleja Lotników 32/46, 02-668 Warsaw, Poland

INSTYTUT FIZYKI
POLSKIEJ AKADEMII NAUK

Date: 04 November 2024

STATEMENT

I declare that my contribution to the paper Md Shahin Alam, **Amar Fakhredine**, Mujeeb Ahmed, P.K. Tanwar, Hung-Yu Yang, Fazel Tafti, Giuseppe Cuono, Rajibul Islam, Bahadur Singh, Artem Lynnyk, Carmine Autieri, Marcin Matusiak, Sign change of anomalous Hall effect and anomalous Nernst effect in the Weyl semimetal CeAlSi, Phys. Rev. B **107**, 085102 (2023) is related to performing and analyzing the density functional theory (DFT) calculations and results, and making the related figures. In addition, I participated in the scientific discussion of the results and in proofreading the manuscript.

Amar Fakhredine

PhD student of ON-3.4 at the Institute of Physics, Polish Academy of Science IFPAN
E-mail: amarf@ifpan.edu.pl
Google Scholar profile:
https://scholar.google.com/citations?user=Jp_m9k4AAAAJ&hl=en&oi=ao
Researchgate profile: https://www.researchgate.net/profile/Amar-Fakhredine/research

INSTYTUT FIZYKI
POLSKIEJ AKADEMII NAUK

Date: 10 July 2024

STATEMENT

I declare that my contribution to the paper Md Shahin Alam, **Amar Fakhredine**, Mujeeb Ahmed, P.K. Tanwar, Hung-Yu Yang, Fazel Tafti, Giuseppe Cuono, Rajibul Islam, Bahadur Singh, Artem Lynnyk, Carmine Autieri, Marcin Matusiak, Sign change of anomalous Hall effect and anomalous Nernst effect in the Weyl semimetal CeAlSi, Phys. Rev. B **107**, 085102 (2023) is as follows,

(i) Participated in the measurements

(ii) Provided the python code and analysed the electrical measurements data

(iii) Participated in conceptualizing the study

(iv) Review and edit the manucript

(v) Participated in addressing the critism raised by reviewers during review process

Yours Faithfully,

Pardeep Kumar
MagTop (6.2)

Institute of Physics, Polish Academy of Sciences, Aleja Lotników 32/46, 02-668 Warsaw, Poland

Date: 6 September 2024

STATEMENT

I declare that my contribution to the paper Md. S. Alam**, A. Fakhredine,** M. Ahmed, P. K. Tanwar, H.-Y. Yang, F. Tafti, G. Cuono, R. Islam, B. Singh, A. Lynnyk, C. Autieri, M. Matusiak, "Sign change of the anomalous Hall effect and the anomalous Nernst effect in Weyl semimetal CeAlSi", published in Phys. Rev. B **107,** 085102 (2023) has been related to participation to the scientific discussion.

Yours Faithfully,

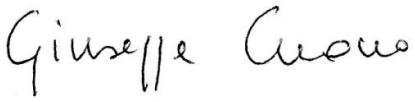

Giuseppe Cuono

Consiglio Nazionale delle Ricerche (CNR-SPIN),
Unità di Ricerca presso Terzi c/o Università "G. D'Annunzio", 66100 Chieti, Italy

Date: 6 September 2024

STATEMENT

I declare that my contribution to the paper Md. S. Alam**, A. Fakhredine,** M. Ahmed, P. K. Tanwar, H.-Y. Yang, F. Tafti, G. Cuono, R. Islam, B. Singh, A. Lynnyk, C. Autieri, M. Matusiak, "Sign change of the anomalous Hall effect and the anomalous Nernst effect in Weyl semimetal CeAlSi", published in Phys. Rev. B **107,** 085102 (2023) has been related to participation to the scientific discussion.

Yours Faithfully,

Rajibul Islam
Postdoctoral researcher,
Physics department, University of of Alabama at Birmingham,
Science and Engineering Complex - East Science Hall,
902 14th Street South Birmingham, AL 35233, USA

INSTYTUT FIZYKI
POLSKIEJ AKADEMII NAUK

Date: 16 July 2024

STATEMENT

I declare that my contribution to the paper Md Shahin Alam, **Amar Fakhredine**, Mujeeb Ahmed, P.K. Tanwar, Hung-Yu Yang, Fazel Tafti, Giuseppe Cuono, Rajibul Islam, Bahadur Singh, Artem Lynnyk, Carmine Autieri, Marcin Matusiak, Sign change of anomalous Hall effect and anomalous Nernst effect in the Weyl semimetal CeAlSi, Phys. Rev. B **107**, 085102 (2023) is as follows:

- The measurements of magnetic moment values along with ac susceptibility of Weyl semimetal CeAlSi by means of SQUID magnetometer.

Yours Faithfully,

Artem Lynnyk

Institute of Physics, Polish Academy of Sciences, Aleja Lotników 32/46, 02-668 Warsaw, Poland

INSTYTUT FIZYKI
POLSKIEJ AKADEMII NAUK

Date: 6 September 2024

STATEMENT

I declare that my contribution to the paper Md. S. Alam**, A. Fakhredine,** M. Ahmed, P. K. Tanwar, H.-Y. Yang, F. Tafti, G. Cuono, R. Islam, B. Singh, A. Lynnyk, C. Autieri, M. Matusiak, "Sign change of the anomalous Hall effect and the anomalous Nernst effect in Weyl semimetal CeAlSi", published in Phys. Rev. B **107,** 085102 (2023) has been related to the discussion on the scientific project and the supervision of the theoretical part of the project.

Yours Faithfully,

Carmine Autieri

Dr. hab. Carmine Autieri, IFPAN professor at the International Centre for Interfacing Magnetism and Superconductivity with Topological Matter (MagTop),
E-mail: autieri@MagTop.ifpan.edu.pl
Website: https://www.magtop.ifpan.edu.pl/resources/teams/
Google Scholar profile: https://scholar.google.it/citations?user=83pF0ywAAAA
ResearchGate profile: https://www.researchgate.net/profile/Carmine_Autieri

Wrocław, 10 July 2024

Dr hab. Marcin Matusiak
Institute of Low Temperature and Structure Research
Polish Academy of Sciences
ul. Okólna 2, 50-422 Wrocław, Poland

STATEMENT

I declare that my contribution to the publication "Sign change of anomalous Hall effect and anomalous Nernst effect in the Weyl semimetal CeAlSi" by Md Shahin Alam, Amar Fakhredine, Mujeeb Ahmad, P.K. Tanwar, Hung-Yu Yang, Fazel Tafti, Giuseppe Cuono, Rajibul Islam, Bahadur Singh, Artem Lynnyk, Carmine Autieri, and Marcin Matusiak, Phys. Rev. B 107, 085102 (2023) dealt mainly with the experimental aspect of the research and was as follows:

I conceived the study as well as supervised the measurements, analysis, writing and reviewing the article.

INSTYTUT FIZYKI
POLSKIEJ AKADEMII NAUK

Date: 04 November 2024

STATEMENT

I declare that my contribution to the paper **Amar Fakhredine**, Raghottam M. Sattigeri, Giuseppe Cuono, and Carmine Autieri. "Interplay between altermagnetism and nonsymmorphic symmetries generating large anomalous Hall conductivity by semi-Dirac points induced anticrossings." *Physical Review B* 108, no. 11 (2023): 115138 is related to:

i. Performing the density functional theory calculations.

ii. Analyzing and collecting the data and discussing with the co-authors.

iii. Produced the figures aside from those related to the AHE.

iv. Writing the draft with the help of the co-authors.

Amar Fakhredine

PhD student of ON-3.4 at the Institute of Physics, Polish Academy of Science IFPAN
E-mail: amarf@ifpan.edu.pl
Google Scholar profile:
https://scholar.google.com/citations?user=Jp_m9k4AAAAJ&hl=en&oi=ao
Researchgate profile: https://www.researchgate.net/profile/Amar-Fakhredine/research

Institute of Physics, Polish Academy of Sciences, Aleja Lotników 32/46, 02-668 Warsaw, Poland

Date: 6 September 2024

STATEMENT

I declare that my contribution to the paper **Amar Fakhredine,** Raghottam M. Sattigeri, Giuseppe Cuono, and Carmine Autieri "Interplay between altermagnetism and nonsymmorphic symmetries generating large anomalous Hall conductivity by semi-Dirac points induced anticrossings" published in Phys. Rev. B **108**, 115138 (2023) has been related to the discussion on the scientific project and the plot of the results reported in Figure 8.

Yours Faithfully,

Raghottam Sattigeri

Affiliation:

Physics Department, Università degli Studi di Milano, Via Celoria 16, 20133 Milan, Italy

Date: 6 September 2024

STATEMENT

I declare that my contribution to the paper **Amar Fakhredine,** Raghottam M. Sattigeri, Giuseppe Cuono, and Carmine Autieri “Interplay between altermagnetism and nonsymmorphic symmetries generating large anomalous Hall conductivity by semi-Dirac points induced anticrossings” published in Phys. Rev. B **108**, 115138 (2023) has been related to the discussion on the scientific project and the plot of the results in Figure 1.

Yours Faithfully,

Giuseppe Cuono

Consiglio Nazionale delle Ricerche (CNR-SPIN),
Unità di Ricerca presso Terzi c/o Università “G. D'Annunzio", 66100 Chieti, Italy

INSTYTUT FIZYKI
POLSKIEJ AKADEMII NAUK

Date: 6 September 2024

STATEMENT

I declare that my contribution to the paper **Amar Fakhredine,** Raghottam M. Sattigeri, Giuseppe Cuono, and Carmine Autieri "Interplay between altermagnetism and nonsymmorphic symmetries generating large anomalous Hall conductivity by semi-Dirac points induced anticrossings" published in Phys. Rev. B **108**, 115138 (2023) has been related to the discussion on the scientific project and the supervision of the project.

Yours Faithfully,

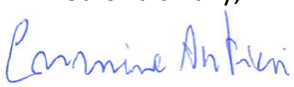

Carmine Autieri

Dr. hab. Carmine Autieri, IFPAN professor at the International Centre for Interfacing Magnetism and Superconductivity with Topological Matter (MagTop),
E-mail: autieri@MagTop.ifpan.edu.pl
Website: https://www.magtop.ifpan.edu.pl/resources/teams/
Google Scholar profile: https://scholar.google.it/citations?user=83pF0ywAAAA
ResearchGate profile: https://www.researchgate.net/profile/Carmine_Autieri

BIBLIOGRAPHY

[1] Lin-Ding Yuan, Alexandru B Georgescu, and James M Rondinelli. Non-relativistic spin splitting in compensated magnets that are not altermagnets. *arXiv preprint arXiv:2402.14321*, 2024.

[2] Albert Fert, Mairbek Chshiev, André Thiaville, and Hongxin Yang. From early theories of dzyaloshinskii–moriya interactions in metallic systems to today's novel roads. *Journal of the Physical Society of Japan*, 92(8):081001, 2023.

[3] AA Burkov. Anomalous hall effect in weyl metals. *Physical review letters*, 113(18):187202, 2014.

[4] Richard M Bozorth. Magnetism. *Reviews of Modern Physics*, 19(1):29, 1947.

[5] Amikam Aharoni. *Introduction to the Theory of Ferromagnetism*, volume 109. Clarendon Press, 2000.

[6] John MD Coey. *Magnetism and magnetic materials*. Cambridge university press, 2010.

[7] Libor Šmejkal, Jairo Sinova, and Tomas Jungwirth. Emerging research landscape of altermagnetism. *Physical Review X*, 12(4):040501, 2022.

[8] J Krempaskỳ, L Šmejkal, SW D'Souza, M Hajlaoui, G Springholz, K Uhlířová, F Alarab, PC Constantinou, V Strocov, D Usanov, et al. Altermagnetic lifting of kramers spin degeneracy. *Nature*, 626(7999):517–522, 2024.

[9] Thorben Schmirander. *Spin-Orbit Coupling Effects and Magnetism of the Topological Edge States of Graphene*. PhD thesis, Staats-und Universitätsbibliothek Hamburg Carl von Ossietzky, 2021.

[10] Igor Markovic. *Interplay of spin-orbit coupling and crystal symmetries in the electronic structures of NbGeSb and $Ca_3Ru_2O_7$*. PhD thesis, University of St Andrews, 2020.

[11] G. Dresselhaus. Spin-orbit coupling effects in zinc blende structures. *Phys. Rev.*, 100:580–586, Oct 1955.

[12] E. I. Rashba and V. I. Sheka. Symmetry of energy bands in crystals of wurtzite type ii. symmetry of bands with spin-orbit interaction included. *New Journal of Physics*, 17:050202, 2015.

[13] Igor Dzyaloshinsky. A thermodynamic theory of "weak" ferromagnetism of antiferromagnetics. *Journal of physics and chemistry of solids*, 4(4):241–255, 1958.

[14] SX Huang and CL Chien. Extended skyrmion phase in epitaxial fege (111) thin films. *Physical review letters*, 108(26):267201, 2012.

[15] Sebastian Mühlbauer, Benedikt Binz, Florian Jonietz, Christian Pfleiderer, Achim Rosch, Anja Neubauer, Robert Georgii, and Peter Böni. Skyrmion lattice in a chiral magnet. *Science*, 323(5916):915–919, 2009.

[16] Tôru Moriya. Anisotropic superexchange interaction and weak ferromagnetism. *Physical review*, 120(1):91, 1960.

[17] Albert Fert, Nicolas Reyren, and Vincent Cros. Magnetic skyrmions: advances in physics and potential applications. *Nature Reviews Materials*, 2(7):1–15, 2017.

[18] Carmine Autieri, Raghottam M Sattigeri, Giuseppe Cuono, and Amar Fakhredine. Staggered dzyaloshinskii-moriya inducing weak ferromagnetism in centrosymmetric altermagnets and weak ferrimagnetism in noncentrosymmetric altermagnets, 2024.

[19] Edwin H Hall et al. On a new action of the magnet on electric currents. *American Journal of Mathematics*, 2(3):287–292, 1879.

[20] Edwin Herbert Hall. Xviii. on the "rotational coefficient" in nickel and cobalt. *The London, Edinburgh, and Dublin Philosophical Magazine and Journal of Science*, 12(74):157–172, 1881.

[21] Robert Karplus and JM Luttinger. Hall effect in ferromagnetics. *Physical Review*, 95(5):1154, 1954.

[22] Jan Smit. The spontaneous hall effect in ferromagnetics ii. *Physica*, 24(1-5):39–51, 1958.

[23] Luc Berger. Side-jump mechanism for the hall effect of ferromagnets. *Physical Review B*, 2(11):4559, 1970.

[24] Michael Victor Berry. Quantal phase factors accompanying adiabatic changes. *Proceedings of the Royal Society of London. A. Mathematical and Physical Sciences*, 392(1802):45–57, 1984.

[25] Binghai Yan and Claudia Felser. Topological materials: Weyl semimetals. *Annual Review of Condensed Matter Physics*, 8(1):337–354, 2017.

[26] M Zahid Hasan, Su-Yang Xu, Ilya Belopolski, and Shin-Ming Huang. Discovery of weyl fermion semimetals and topological fermi arc states. *Annual Review of Condensed Matter Physics*, 8(1):289–309, 2017.

[27] Su-Yang Xu, Nasser Alidoust, Guoqing Chang, Hong Lu, Bahadur Singh, Ilya Belopolski, Daniel S Sanchez, Xiao Zhang, Guang Bian, Hao Zheng, et al. Discovery of lorentz-violating type ii weyl fermions in laalge. *Science advances*, 3(6):e1603266, 2017.

[28] M. Zahid Hasan, Guoqing Chang, Ilya Belopolski, Guang Bian, Su-Yang Xu, and Jia-Xin Yin. Weyl, dirac and high-fold chiral fermions in topological quantum matter. *Nature Reviews Materials*, 6(9):784–803, Sep 2021.

[29] Shuo Wang, Ben-Chuan Lin, An-Qi Wang, Da-Peng Yu, and Zhi-Min Liao. Quantum transport in dirac and weyl semimetals: a review. *Advances in Physics: X*, 2(3):518–544, 2017.

[30] Chandra Shekhar, Nitesh Kumar, V Grinenko, Sanjay Singh, R Sarkar, H Luetkens, Shu-Chun Wu, Yang Zhang, Alexander C Komarek, Erik Kampert, et al. Anomalous hall effect in weyl semimetal half-heusler compounds rptbi (r= gd and nd). *Proceedings of the National Academy of Sciences*, 115(37):9140–9144, 2018.

[31] Narayan Mohanta, Jong Mok Ok, Jie Zhang, Hu Miao, Elbio Dagotto, Ho Nyung Lee, and Satoshi Okamoto. Semi-dirac and weyl fermions in transition metal oxides. *Physical Review B*, 104(23):235121, 2021.

[32] Ying Wu. A semi-dirac point and an electromagnetic topological transition in a dielectric photonic crystal. *Optics express*, 22(2):1906–1917, 2014.

[33] Chengyong Zhong, Yuanping Chen, Yuee Xie, Yi-Yang Sun, and Shengbai Zhang. Semi-dirac semimetal in silicene oxide. *Physical Chemistry Chemical Physics*, 19(5):3820–3825, 2017.

[34] Ayan Banerjee and Awadhesh Narayan. Non-hermitian semi-dirac semi-metals. *Journal of Physics: Condensed Matter*, 33(22):225401, 2021.

[35] Ipsita Mandal. Andreev bound states in josephson junctions of semi-dirac semimetals. *Physica B: Condensed Matter*, 683:415918, 2024.

[36] Luyang Wang, Shao-Kai Jian, and Hong Yao. Hourglass semimetals with nonsymmorphic symmetries in three dimensions. *Physical Review B*, 96(7):075110, 2017.

[37] Q Niu, WC Yu, KY Yip, ZL Lim, H Kotegawa, E Matsuoka, H Sugawara, H Tou, Y Yanase, and Swee K Goh. Quasilinear quantum magnetoresistance in pressure-induced nonsymmorphic superconductor chromium arsenide. *Nature Communications*, 8(1):15358, 2017.

[38] Han Wu, Alannah M Hallas, Xiaochan Cai, Jianwei Huang, Ji Seop Oh, Vaideesh Loganathan, Ashley Weiland, Gregory T McCandless, Julia Y Chan, Sung-Kwan Mo, et al. Nonsymmorphic symmetry-protected band crossings in a square-net metal ptpb4. *npj Quantum Materials*, 7(1):31, 2022.

[39] Reiner M Dreizler and Eberhard KU Gross. *Density functional theory: an approach to the quantum many-body problem*. Springer Science & Business Media, 2012.

[40] Max Born and W Heisenberg. Zur quantentheorie der molekeln. *Original Scientific Papers Wissenschaftliche Originalarbeiten*, pages 216–246, 1985.

[41] Geerd HF Diercksen and Stephen Wilson. *Methods in computational molecular physics*, volume 113. Springer Science & Business Media, 2012.

[42] John C Slater. A simplification of the hartree-fock method. *Physical review*, 81(3):385, 1951.

[43] Charlotte Froese Fischer. Hartree–fock method for atoms. a numerical approach. 1977.

[44] EM Stoudenmire, Lucas O Wagner, Steven R White, and Kieron Burke. One-dimensional continuum electronic structure with the density-matrix renormalization group and its implications for density-functional theory. *Physical review letters*, 109(5):056402, 2012.

[45] Pierre Hohenberg and Walter Kohn. Inhomogeneous electron gas. *Physical Review*, 136(3B):B864, 1964.

[46] Kieron Burke and Lucas O Wagner. Dft in a nutshell. *International Journal of Quantum Chemistry*, 113(2):96–101, 2013.

[47] W. Kohn and L. J. Sham. Self-consistent equations including exchange and correlation effects. *Phys. Rev.*, 140:A1133–A1138, Nov 1965.

[48] John P Perdew and Alex Zunger. Self-interaction correction to density-functional approximations for many-electron systems. *Physical review B*, 23(10):5048, 1981.

[49] Axel D Becke. Density-functional exchange-energy approximation with correct asymptotic behavior. *Physical review A*, 38(6):3098, 1988.

[50] J. P. Perdew, K. Burke, and M. Ernzerhof. Generalized gradient approximation made simple. *Phys. Rev. Lett.*, 77:3865–3868, Oct 1996.

[51] Kieron Burke, John P Perdew, and Matthias Ernzerhof. Why semilocal functionals work: Accuracy of the on-top pair density and importance of system averaging. *The Journal of chemical physics*, 109(10):3760–3771, 1998.

[52] Richard M Martin. *Electronic structure: basic theory and practical methods*. Cambridge university press, 2020.

[53] Feliciano Giustino. *Materials modelling using density functional theory: properties and predictions*. Oxford University Press, 2014.

[54] Ws and Peter Puschnig. Fundamentals of electronic structure theory (phu.013). 2018.

[55] Nicola Marzari, Ivo Souza, and David Vanderbilt. An introduction to maximally-localized wannier functions. *Psi-K newsletter*, 57:129, 2003.

[56] A. A. Mostofi, J. R. Yates, Young-Su Lee, I. Souza, D. Vanderbilt, and N. Marzari. wannier90: A tool for obtaining maximally-localised wannier functions. *Computer Physics Communications*, 178(9):685–699, May 2008.

[57] Gregory H Wannier. The structure of electronic excitation levels in insulating crystals. *Physical Review*, 52(3):191, 1937.

[58] Nicola Marzari and David Vanderbilt. Maximally localized generalized wannier functions for composite energy bands. *Physical review B*, 56(20):12847, 1997.

[59] Nicola Marzari, Arash A Mostofi, Jonathan R Yates, Ivo Souza, and David Vanderbilt. Maximally localized wannier functions: Theory and applications. *Reviews of Modern Physics*, 84(4):1419, 2012.

[60] B Sporkmann and H Bross. Calculation of wannier functions for fcc transition metals by fourier transformation of bloch functions. *Physical Review B*, 49(16):10869, 1994.

[61] Xinjie Wang, Jonathan R Yates, Ivo Souza, and David Vanderbilt. Ab initio calculation of the anomalous hall conductivity by wannier interpolation. *Physical Review B*, 74(19):195118, 2006.

[62] Md Shahin Alam, Amar Fakhredine, Mujeeb Ahmad, P. K. Tanwar, Hung-Yu Yang, Fazel Tafti, Giuseppe Cuono, Rajibul Islam, Bahadur Singh, Artem Lynnyk, Carmine Autieri, and Marcin Matusiak. Sign change of anomalous hall effect and anomalous nernst effect in the weyl semimetal cealsi. *Phys. Rev. B*, 107:085102, Feb 2023.

[63] Tôru Moriya. New mechanism of anisotropic superexchange interaction. *Physical Review Letters*, 4(5):228, 1960.

[64] CD Hu. Relationship between ferroelectricity and dzyaloshinskii-moriya interaction in multiferroics and the effect of bond-bending. *Physical Review B*, 77(17):174418, 2008.

[65] Hongxin Yang, Jinghua Liang, and Qirui Cui. First-principles calculations for dzyaloshinskii–moriya interaction. *Nature Reviews Physics*, 5(1):43–61, 2023.

[66] Abderrezak Belabbes, G Bihlmayer, F Bechstedt, S Blügel, and Aurelien Manchon. Hund's rule-driven dzyaloshinskii-moriya interaction at 3 d- 5 d interfaces. *Physical review letters*, 117(24):247202, 2016.

[67] Vikas Kashid, Timo Schena, Bernd Zimmermann, Yuriy Mokrousov, Stefan Blügel, Vaishali Shah, and HG Salunke. Dzyaloshinskii-moriya interaction and chiral magnetism in 3 d- 5 d zigzag chains: Tight-binding model and ab initio calculations. *Physical Review B*, 90(5):054412, 2014.

[68] Sukanta Kumar Jena, Rajibul Islam, Ewelina Milińska, Marcin M Jakubowski, Roman Minikayev, Sabina Lewińska, Artem Lynnyk, Aleksiej Pietruczik, Paweł Aleszkiewicz, Carmine Autieri, et al. Interfacial dzyaloshinskii–moriya interaction in the epitaxial w/co/pt multilayers. *Nanoscale*, 13(16):7685–7693, 2021.

[69] SK Jena, J Kisielewski, R Gieniusz, U Guzowska, A Fakhredine, C Autieri, A Lynnyk, A Pietruczik, A Maziewski, and A Wawro. Field angle-dependent bubble lattice formation in re/co/pt multilayers. In *2023 IEEE International Magnetic Conference-Short Papers (INTERMAG Short Papers)*, pages 1–2. IEEE, 2023.

[70] Anuj Kumar Dhiman, Amar Fakhredine, Ryszard Gieniusz, Zbigniew Kurant, Iosif Sveklo, Piotr Dłużewski, Wojciech Dobrogowski, Sukanta Kumar Jena, Aleksiej Pietruczik, Carmine Autieri, Andrzej Wawro, and Andrzej Maziewski. Evolution of static and dynamic magnetic properties of re/co/pt and pt/co/re trilayers with enhanced dzyaloshinskii-moriya interaction. *Applied Surface Science*, 679:161151, 2025.

[71] Hongxin Yang, André Thiaville, Stanislas Rohart, Albert Fert, and Mairbek Chshiev. Anatomy of dzyaloshinskii-moriya interaction at co/pt interfaces. *Physical review letters*, 115(26):267210, 2015.

[72] Priyamvada Jadaun, Leonard F Register, and Sanjay K Banerjee. The microscopic origin of dmi in magnetic bilayers and prediction of giant dmi in new bilayers. *npj Computational Materials*, 6(1):88, 2020.

[73] Hongying Jia, Bernd Zimmermann, and Stefan Blügel. First-principles investigation of chiral magnetic properties in multilayers: Rh/co/pt and pd/co/pt. *Physical Review B*, 98(14):144427, 2018.

[74] Ruyi Chen, Qirui Cui, Liyang Liao, Yingmei Zhu, Ruiqi Zhang, Hua Bai, Yongjian Zhou, Guozhong Xing, Feng Pan, Hongxin Yang, et al. Reducing dzyaloshinskii-moriya interaction and field-free spin-orbit torque switching in synthetic antiferromagnets. *Nature Communications*, 12(1):3113, 2021.

[75] Bernd Zimmermann, William Legrand, Davide Maccariello, Nicolas Reyren, Vincent Cros, Stefan Blügel, and Albert Fert. Dzyaloshinskii-moriya interaction at disordered interfaces from ab initio theory: Robustness against intermixing and tunability through dusting. *Applied physics letters*, 113(23), 2018.

[76] IE Dzyaloshinskii. Theory of helicoidal structures in antiferromagnets. 3. *SOVIET PHYSICS JETP-USSR*, 20(3):665–+, 1965.

[77] Alexei N Bogdanov and DA Yablonskii. Thermodynamically stable "vortices" in magnetically ordered crystals. the mixed state of magnets. *Zh. Eksp. Teor. Fiz*, 95(1):178, 1989.

[78] Jonathan Gaudet, Hung-Yu Yang, Santu Baidya, Baozhu Lu, Guangyong Xu, Yang Zhao, Jose A Rodriguez-Rivera, Christina M Hoffmann, David E Graf, Darius H Torchinsky, et al. Weyl-mediated helical magnetism in ndalsi. *Nature materials*, 20(12):1650–1656, 2021.

[79] Xiaohan Yao, Jonathan Gaudet, Rahul Verma, David E Graf, Hung-Yu Yang, Faranak Bahrami, Ruiqi Zhang, Adam A Aczel, Sujan Subedi, Darius H Torchinsky, et al. Large topological hall effect and spiral magnetic order in the weyl semimetal smalsi. *Physical Review X*, 13(1):011035, 2023.

[80] Meng Lyu, Junsen Xiang, Zhenyu Mi, Hengcan Zhao, Zhen Wang, Enke Liu, Genfu Chen, Zhian Ren, Gang Li, and Peijie Sun. Nonsaturating magnetoresistance, anomalous hall effect, and magnetic quantum oscillations in the ferromagnetic semimetal pralsi. *Physical Review B*, 102(8):085143, 2020.

[81] Avinash Kumar Chaurasiya, Samiran Choudhury, Jaivardhan Sinha, and Anjan Barman. Dependence of interfacial dzyaloshinskii-moriya interaction on layer thicknesses in ta/co-fe-b/tao x heterostructures from brillouin light scattering. *Physical Review Applied*, 9(1):014008, 2018.

[82] Adam WJ Wells, Philippa M Shepley, Christopher H Marrows, and Thomas A Moore. Effect of interfacial intermixing on the dzyaloshinskii-moriya interaction in pt/co/pt. *Physical review B*, 95(5):054428, 2017.

[83] Hung-Yu Yang, Bahadur Singh, Jonathan Gaudet, Baozhu Lu, Cheng-Yi Huang, Wei-Chi Chiu, Shin-Ming Huang, Baokai Wang, Faranak Bahrami, Bochao Xu, et al. Noncollinear ferromagnetic weyl semimetal with anisotropic anomalous hall effect. *Physical Review B*, 103(11):115143, 2021.

[84] Naoto Nagaosa, Jairo Sinova, Shigeki Onoda, Allan H MacDonald, and Nai Phuan Ong. Anomalous Hall effect. *Reviews of Modern Physics*, 82(2):1539, 2010.

[85] Madhav Prasad Ghimire, Jorge I Facio, Jhih-Shih You, Linda Ye, Joseph G Checkelsky, Shiang Fang, Efthimios Kaxiras, Manuel Richter, and Jeroen Van Den Brink. Creating weyl nodes and controlling their energy by magnetization rotation. *Physical Review Research*, 1(3):032044, 2019.

[86] Juba Bouaziz, Gustav Bihlmayer, Christopher E Patrick, Julie B Staunton, and Stefan Blügel. Origin of incommensurate magnetic order in the r alsi magnetic weyl semimetals (r= pr, nd, sm). *Physical Review B*, 109(20):L201108, 2024.

[87] Jadupati Nag, Bishal Das, Sayantika Bhowal, Yukimi Nishioka, Barnabha Bandyopadhyay, Shiv Kumar, Kenta Kuroda, Akio Kimura, KG Suresh, and Aftab Alam. Gdalsi: An antiferromagnetic topological weyl semimetal with non-relativistic spin splitting. *arXiv preprint arXiv:2312.11980*, 2023.

[88] Miina Leiviskä, Javier Rial, Antonín Badura, Rafael Lopes Seeger, Ismaïla Kounta, Sebastian Beckert, Dominik Kriegner, Isabelle Joumard, Eva Schmoranzerová, Jairo Sinova, et al. Anisotropy of the anomalous hall effect in the altermagnet candidate mn _5 si _3 films. *arXiv preprint arXiv:2401.02275*, 2024.

[89] RD Gonzalez Betancourt, Jan Zubáč, R Gonzalez-Hernandez, Kevin Geishendorf, Zbynek Šobáň, Gunther Springholz, Kamil Olejník, Libor Šmejkal, Jairo Sinova, Tomas Jungwirth, et al. Spontaneous anomalous hall effect arising from an unconventional compensated magnetic phase in a semiconductor. *Physical Review Letters*, 130(3):036702, 2023.

[90] YX Zhao and Andreas P Schnyder. Nonsymmorphic symmetry-required band crossings in topological semimetals. *Physical Review B*, 94(19):195109, 2016.

[91] Tirthankar Chakraborty, Kartik Samanta, Satya N Guin, Jonathan Noky, Iñigo Robredo, Suchitra Prasad, Juergen Kuebler, Chandra Shekhar, Maia G Vergniory, and Claudia Felser. Berry curvature induced anomalous hall conductivity in the magnetic topological oxide double perovskite sr 2 femoo 6. *Physical Review B*, 106(15):155141, 2022.

[92] Giuseppe Cuono, Carmine Autieri, Giuseppe Guarnaccia, Adolfo Avella, Mario Cuoco, Filomena Forte, and Canio Noce. Spin–orbit coupling effects on the electronic properties of the pressure-induced superconductor cras. *The European Physical Journal Special Topics*, 228:631–641, 2019.

[93] DJ Campbell, John Collini, Jagoda Sławińska, C Autieri, L Wang, K Wang, B Wilfong, YS Eo, Paul Neves, D Graf, et al. Topologically driven linear magnetoresistance in helimagnetic fep. *npj Quantum Materials*, 6(1):38, 2021.

[94] Pierre Adroguer, David Carpentier, Gilles Montambaux, and Edmond Orignac. Diffusion of dirac fermions across a topological merging transition in two dimensions. *Physical Review B*, 93(12):125113, 2016.

[95] Jacques K Desmarais, Jean-Pierre Flament, and Alessandro Erba. Spin-orbit coupling in periodic systems with broken time-reversal symmetry: Formal and computational aspects. *Physical Review B*, 101(23):235142, 2020.

[96] Joon Sue Lee, Anthony Richardella, Robert D Fraleigh, Chao-xing Liu, Weiwei Zhao, and Nitin Samarth. Engineering the breaking of time-reversal symmetry in gate-tunable hybrid ferromagnet/topological insulator heterostructures. *npj Quantum Materials*, 3(1):51, 2018.

[97] Anjan Soumyanarayanan, Nicolas Reyren, Albert Fert, and Christos Panagopoulos. Emergent phenomena induced by spin–orbit coupling at surfaces and interfaces. *Nature*, 539(7630):509–517, 2016.

[98] Guo-Cai Wang, Wei Du, Lei Guo, Hua Su, and Xiao-Li Tang. The role of interfacial dzyaloshinskii–moriya interaction in different heavy metal-based perpendicular magnetic systems and its application in spintronic devices. *Applied Physics Letters*, 125(7), 2024.

[99] Vineet Kumar Sharma, Alana Okullo, Jalen Garner, Cheng Peng, Rajan Plumley, Adrian Feiguin, Chunjing Jia, Josh Turner, A Bansil, and Sugata Chowdhury. Skyrmions: A review on materials perspective for future electronic devices. *arXiv preprint arXiv:2402.01503*, 2024.

[100] Yuqing Zhou, Shuang Li, Xue Liang, and Yan Zhou. Topological spin textures: Basic physics and devices. *Advanced Materials*, page 2312935.

[101] Jairo Sinova, Sergio O Valenzuela, Jörg Wunderlich, CH Back, and T Jungwirth. Spin hall effects. *Reviews of modern physics*, 87(4):1213–1260, 2015.

[102] Sumathi Rao. Weyl semi-metals: a short review. *arXiv preprint arXiv:1603.02821*, 2016.

[103] Han Yan, Xiaorong Zhou, Peixin Qin, and Zhiqi Liu. Review on spin-split antiferromagnetic spintronics. *Applied Physics Letters*, 124(3), 2024.

[104] Hongyu Chen, Li Liu, Xiaorong Zhou, Ziang Meng, Xiaoning Wang, Zhiyuan Duan, Guojian Zhao, Han Yan, Peixin Qin, and Zhiqi Liu. Emerging antiferromagnets for spintronics. *Advanced Materials*, 36(14):2310379, 2024.

[105] Ling Bai, Wanxiang Feng, Siyuan Liu, Libor Šmejkal, Yuriy Mokrousov, and Yugui Yao. Altermagnetism: Exploring new frontiers in magnetism and spintronics. *Advanced Functional Materials*, page 2409327, 2024.